



저작자표시-비영리-변경금지 2.0 대한민국

이용자는 아래의 조건을 따르는 경우에 한하여 자유롭게

- 이 저작물을 복제, 배포, 전송, 전시, 공연 및 방송할 수 있습니다.

다음과 같은 조건을 따라야 합니다:



저작자표시. 귀하는 원저작자를 표시하여야 합니다.



비영리. 귀하는 이 저작물을 영리 목적으로 이용할 수 없습니다.



변경금지. 귀하는 이 저작물을 개작, 변형 또는 가공할 수 없습니다.

- 귀하는, 이 저작물의 재이용이나 배포의 경우, 이 저작물에 적용된 이용허락조건을 명확하게 나타내어야 합니다.
- 저작권자로부터 별도의 허가를 받으면 이러한 조건들은 적용되지 않습니다.

저작권법에 따른 이용자의 권리는 위의 내용에 의하여 영향을 받지 않습니다.

이것은 [이용허락규약\(Legal Code\)](#)을 이해하기 쉽게 요약한 것입니다.

[Disclaimer](#)

이학박사 학위논문

**Investigation on correlated topological  
phases in pyrochlore iridate thin films**

파이로클로로 이리듐 산화물 박막에서의 강상관계  
위상 상태에 대한 연구

2019년 2월

서울대학교 대학원

물리천문학부

김우진

# **Investigation on correlated topological phases in pyrochlore iridate thin films**

Woo Jin Kim

Supervised by  
Professor Tae Won Noh

A Dissertation submitted to the Faculty of Seoul National  
University in Partial Fulfillment of the Requirements for the  
Degree of Doctor of Philosophy  
February 2019

*Department of Physics and Astronomy  
Graduate School  
Seoul National University*

Investigation on correlated topological phases in  
pyrochlore iridate thin films

파이로클로로 이리듐 산화물 박막에서의 강상관계  
위상 상태에 대한 연구

지도교수 노 태 원

이 논문을 이학박사 학위논문으로 제출함  
2018년 12월

서울대학교 대학원  
물리천문학부  
김 우 진

김우진의 이학박사 학위논문을 인준함  
2018년 12월

위 원 장	양 범 정	(인) 
부위원장	노 태 원	(인) 
위 원	김 창 영	(인) 
위 원	박 철 환	(인) 
위 원	장 서 형	(인) 

## **Abstract**

*5d* transition metal oxides (TMOs) have received much attention as unexplored playgrounds where a rich of exotic quantum phenomena take place. In particular, *5d* TMOs electron-electron correlations ( $U$ ), electron band width ( $W$ ) and the energy of spin-orbit coupling (SOC) have comparable energy scales. The interplay among three energy scales can induce novel topological phenomena. Among *5d* TMOs, iridium-based oxide materials have attracted a great deal of interest due to their novel physical properties stemmed from strong SOC of Iridium. A number of exotic electronic states including Weyl semi-metal, Axion insulator, and Topological insulator, have been predicted for various iridates and their heterostructures.

Epitaxial thin film can provide fertile playgrounds for studying topological phases which have distinct electronic structures. Since the electronic structure of the materials are strongly governed by the systems crystal symmetry, fabricating the target material with epitaxial thin film form give benefit for studying topological ground state as following reasons. First, by using different substrates, we can designate the lattice structures which have different crystalline symmetries. Second, by strain effect, we can break certain crystal symmetry, i.e., cubic symmetry breaking. I will report the electronic structures and its related topological physical properties of epitaxially grown iridates thin films.

We investigated electronic structure of rutile IrO<sub>2</sub> thin film, simplest form among iridates, which has nonsymmorphic symmetry crystalline symmetry. Our optical

conductivity measurements and the generalized gradient approximation (GGA) + SOC calculation showed that SOC has an effect on the band-structure formation of IrO<sub>2</sub>, close to  $E_F$ . However, O 1s X-ray absorption spectroscopy (XAS) results and projected density of state (pDOS) analysis of Ir *d* orbitals suggest that the  $J_{\text{eff}} = 1/2$  state no longer exists in metallic IrO<sub>2</sub>. Maintaining its metallic state with reasonably strong SOC, IrO<sub>2</sub> epitaxial thin films provide a sufficient environment for electronic transport applications, such as highly sensitive spin detection devices.

Ferroic domain walls (DWs) create different symmetries and ordered states compared with those in single domain bulk materials. In particular, the DWs of an antiferromagnet with noncoplanar spin structure have a distinct symmetry that cannot be realized in those of their ferromagnet counterparts. We show that an unconventional anomalous Hall effect (AHE) can arise from the DWs of a noncoplanar antiferromagnet, Nd<sub>2</sub>Ir<sub>2</sub>O<sub>7</sub>. Bulk Nd<sub>2</sub>Ir<sub>2</sub>O<sub>7</sub> has a cubic symmetry; thus, its Hall signal should be zero without an applied magnetic field. The DWs generated in this material break the twofold rotational symmetry, which allows for finite anomalous Hall conductivity. It highlights the symmetry-broken interface of AFM materials as a means of exploring topological effects and their relevant applications.

When this Nd<sub>2</sub>Ir<sub>2</sub>O<sub>7</sub> can be deposited on Y-stabilized ZrO<sub>2</sub> (YSZ) with epitaxial strain induced, the antiferromagnetic insulator ground state undergoes topological phase transition and can become Weyl semimetal or Axion insulator. We observed large AHE in compressively strained Nd<sub>2</sub>Ir<sub>2</sub>O<sub>7</sub> thin film. The size of anomalous Hall conductivity value is comparably large with theoretically predicted value. Moreover, resistivity of the film is

significantly reduced compare to fully relaxed film. From the longitudinal magneto-resistance measurements, we observed negative magneto-resistance which may be due to chiral charge pumping through two Weyl points. We strongly suggest the strain effect on pyrochlore iridates is very effective control parameter to study emergent topological phases and its related exotic phenomenon.

Keywords: Correlated topological phases, electronic structures, anomalous Hall effect, Weyl semimetal, pyrochlore iridate, Magneto-transport.

Student number: 2013-20360

<b>Abstracts .....</b>	<b>i</b>
<b>List of Figures .....</b>	<b>vii</b>
<b>1 Introduction .....</b>	<b>1</b>
1.1 Correlated topological state in <i>5d</i> transition metal oxides (TMOs).....	1
1.2 Strain induced topological phase transitions in <i>5d</i> TMO heterostructures .....	3
1.3 Outlines of thesis.....	4
<b>2 Experimental detail .....</b>	<b>7</b>
2.1 Pulsed-laser deposition .....	7
2.2 <i>In-situ</i> spectroscopic ellipsometry .....	9
2.3 Magnetotransport measurement .....	11
<b>3 The role of spin orbit coupling (SOC) in nonsymmorphic IrO<sub>2</sub> thin film and its electronic structure.....</b>	<b>14</b>
3.1 Introduction .....	14
3.2 Results and Discussion .....	16
3.2.1 Experimental details .....	16
3.2.2 Structural characterization and transport property.....	18
3.2.3 Optical spectroscopy and first-principles calculations.....	21
3.2.4 X-ray-absorption spectroscopy: Orbital character of an empty state near $E_F$ .....	24
3.3 Conclusion .....	27

<b>4</b>	<b>Unconventional anomalous Hall effect (AHE) from antiferromagnetic (AFM) domain walls (DWs) of Nd<sub>2</sub>Ir<sub>2</sub>O<sub>7</sub> thin films .....</b>	<b>33</b>
4.1	Introduction .....	33
4.2	Results and Discussion .....	36
4.2.1	Sample preparation .....	36
4.2.1.1	Deposition of Nd <sub>2</sub> Ir <sub>2</sub> O <sub>7</sub> thin films.....	36
4.2.1.2	Scanning transmission electron microscopy measurements.....	38
4.2.1.3	Resistivity and magnetotransport measurements.....	40
4.2.2	AFM domain switching .....	42
4.2.2.1	Magnetoresistance hysteresis .....	42
4.2.2.2	Asymmetric analysis on hysteretic magnetoresistance curves...	43
4.2.2.3	Domain switching caused by the <i>f</i> - <i>d</i> exchange interaction.....	46
4.2.3	AHEs caused by antiferromagnetic .....	47
4.2.3.1	AHEs observed in Nd <sub>2</sub> Ir <sub>2</sub> O <sub>7</sub> thin films.....	47
4.2.3.2	Bulk AHE of AFM material: Scalar spin chirality.....	49
4.2.3.3	Emergence of the AHE in the presence of an AFM DW: Symmetry analysis.....	51
4.2.3.4	Unconventional AHE at the antiferromagnetic DWs of Nd <sub>2</sub> Ir <sub>2</sub> O <sub>7</sub> thin films.....	53
4.3	Conclusion .....	55

<b>5</b>	<b>Strain induced Weyl semimetal state in epitaxial Nd<sub>2</sub>Ir<sub>2</sub>O<sub>7</sub> thin film.....</b>	<b>60</b>
5.1	Introduction .....	60
5.2	Results and Discussion .....	63
5.2.1	Experimental details .....	63
5.2.2	Sample preparation .....	64
5.2.2.1	Difficulties on <i>in-situ</i> pyrochlore iridate growth.....	64
5.2.2.2	Rapid pulse annealing epitaxy.....	69
5.2.2.3	Sample characterization.....	71
5.2.3	Strain induced insulator to semimetal transition.....	74
5.2.3.1	Strain effect and phase diagram .....	74
5.2.3.2	Resistivity comparision between fully relaxed and strained samples.....	76
5.2.4	Large AHE and cubic symmetry breaking.....	80
5.2.5	Chiral anomaly-related magnetoresistance in Weyl semimetals.....	82
5.3	Conclusion.....	85
<b>6</b>	<b>Conclusion .....</b>	<b>91</b>
	<b>Publication List .....</b>	<b>94</b>
	<b>국문초록 (Abstract in Korean).....</b>	<b>96</b>
	<b>감사의 글 (Acknowledgements).....</b>	<b>99</b>

## List of figures

**Figure 1.1** Sketch of a generic phase diagram for electronic materials in terms of the interaction strength  $U/t$  and spin-orbit coupling  $\lambda/t$ . [4]

**Figure 2.1** Schematic diagram of a PLD chamber. It consists of a target holder and a substrate holder housed in a vacuum chamber.

**Figure 2.2** (a) Schematic diagram of a PLD chamber with *in-situ* spectroscopic ellipsometry. It consists of a target and a substrate housed in a vacuum chamber. (b) Real photo of Experimental setup for *in-situ* spectroscopic ellipsometry, which is equipped with IR laser heater, ion gauge, variable leakage valve, and M-2000D ellipsometer.

**Figure 2.3** Schematic diagram of setup for MR and Hall measurement.

**Figure 3.1** Ir 4*f* core level spectrum from in-situ and *ex-situ* XPS measurements.

**Figure 3.2** (a) X-ray sideways geometry to probe the (200) Bragg peak in the thin film/substrate. (b) X-ray diffraction pattern of IrO<sub>2</sub> grown on (100) TiO<sub>2</sub> substrate. (c) Reciprocal space mapping of (301) IrO<sub>2</sub>. (d) Reciprocal space mapping of (310) IrO<sub>2</sub>. (e) Temperature dependence of resistivity of IrO<sub>2</sub> thin film along [010] and [001] corresponding to the *b* axis and *c* axis, respectively.

**Figure 3.3** (a) Experimental optical conductivity spectra of IrO<sub>2</sub> *b* axis [010] (black empty circle) and theoretically computed interband component of the optical conductivity values based on GGA (blue dashed line) and GGA+SOC (red solid line). (b) Experimental optical conductivity spectra of IrO<sub>2</sub> *c* axis [001] and theoretically computed

interband component of the optical conductivity values based on GGA (blue dashed line) and GGA+SOC (red solid line). (c) Brillouin zone of IrO<sub>2</sub> film. (d) Band dispersion computed within GGA approximation. (e) Band dispersion computed within GGA+SOC approximation.

**Figure 3.4** (a) Indication of sample orientation and polarized light direction.  $\pi$  and  $\sigma$  polarization light are parallel to  $c$  and  $b$  axes, respectively. (b) O 1s Polarization-dependent X-ray absorption spectroscopy of IrO<sub>2</sub> grown on (100) TiO<sub>2</sub> substrate.

**Figure 4.1** Schematic diagrams of the magnetic domain structure of Nd<sub>2</sub>Ir<sub>2</sub>O<sub>7</sub>. (a) The magnetic structure of Nd 4*f* moments (blue arrows) and Ir 5*d* moments (red arrows) at  $H = 0$  at temperatures below  $T_N^{\text{Nd}}$ . The Ir and Nd sublattices have all-in-all-out (AIAO) and all-out-all-in (AOAI) ordering, respectively. (b) The magnetic structure in sufficiently strong  $H$ . The Nd 4*f* and Ir 5*d* moments are coupled with the *f-d* exchange interaction. (c) Schematic diagram of the domain walls (DWs) between Ir-AIAO and Ir-AOAI. The purple-colored line indicates the possible DW structure with finite magnetization. (d) Schematic diagram of the dotted square region in (c), enlarged for detail. The purple arrows indicate the net magnetization of Ir moments at a DW.

**Figure 4.2** (a) X-ray diffraction pattern of an 80-nm-thick Nd<sub>2</sub>Ir<sub>2</sub>O<sub>7</sub> film grown on a YSZ (111) substrate (red bold line) and the diffraction pattern of the bare YSZ substrate (black bold line). (b) Nd<sub>2</sub>Ir<sub>2</sub>O<sub>7</sub> (222) diffraction pattern. (c) Rocking curve of Nd<sub>2</sub>Ir<sub>2</sub>O<sub>7</sub> /YSZ (111) film. (d) Reciprocal space mapping of Nd<sub>2</sub>Ir<sub>2</sub>O<sub>7</sub> (662).

**Figure 4.3** (a) Scanning transmission electron microscopy (STEM) image of an Nd<sub>2</sub>Ir<sub>2</sub>O<sub>7</sub> film grown on YSZ (111) from the viewpoint of the  $[2\bar{1}\bar{1}]$  axis. The Nd<sub>2</sub>Ir<sub>2</sub>O<sub>7</sub> film exhibits an ordered pyrochlore structure and an epitaxial relationship with the YSZ

substrate. (b) The FFT of the pyrochlore  $\text{Nd}_2\text{Ir}_2\text{O}_7$  thin film (upper red dashed square) and (c) that of the YSZ substrate (downside red dashed square).

**Figure 4.4** (a) Temperature dependence of the longitudinal resistivity  $\rho_{xx}$  of the 80-nm-thick film (red bold line) and its counterpart of single crystal from Ref. [15] (blue square). (b) Temperature dependent magneto-resistance ( $MR$ ) of  $\text{Nd}_2\text{Ir}_2\text{O}_7$  for various  $H // [111]$  from 0 T to 14 T. The  $T_N^{\text{Nd}}$  ( $\sim 15$  K) and  $T_N^{\text{Ir}}$  ( $\sim 30$  K) indicate the Néel temperature of the Nd and Ir moments, respectively. (c) Corresponding normalized  $MR$  values versus temperature. When  $H$  is sufficiently large, the gradient of  $MR$  changes from positive to negative at  $T_N^{\text{Nd}}$ . (d) Normalized  $MR$  values with  $H // [111]$  at 2 K of 80-nm-thick film (red bold line) and a single crystal from Ref. [15] (blue square).

**Figure 4.5** (a) Normalized magneto-resistance ( $MR$ ) at various temperatures with  $H // [111]$ . (b) Asymmetric part of sweep-up  $MR$  at 1.8 K (positive  $H$ ). The colored region with Roman numerals corresponds to the represented spin structures. The red (blue) and orange solid lines indicate the hysteretic part of Ir (Nd) domain switching from Eq. (2) and its total contribution to both Nd and Ir, respectively. (c) Quantified fit parameters ‘ $a$ ’ extracted from Eq. (2), where red empty circles (blue empty diamonds) indicate the contribution of hysteretic behavior from Ir (Nd) domain switching. (d) Red empty circles and blue empty diamonds are the coercive fields of the Ir domain and Nd spins, respectively, from  $MR$ . At 30 K, the asymmetric  $MR$  becomes too small to obtain reliable values of the coercive field.

**Figure 4.6** (a)  $H$ -dependence of Hall resistivity taken with  $H // [111]$  at various temperatures. The arrows indicate the  $H$  sweep directions. (b) Black empty circles

indicate the Hall resistivity at 2 K. The ordinary Hall term is subtracted by linear fitting in the higher  $H$  region. The blue solid lines indicate the contribution of the bulk-anomalous Hall effect (AHE). The red circles indicate the DW-AHE. (c) Color map of anomalous Hall resistivity (ordinary Hall term is subtracted) in the  $T$ - $H$  plane. The red empty circles represent the coercive field  $H_c^{\text{Ir}}$  of Ir domain switching, which are obtained from  $MR$  measurements.

**Figure 5.1** (a) Phase diagram of  $R_2\text{Ir}_2\text{O}_7$  (R: rare earth atoms) film growth. The solid blue (dashed black) line indicates the vapor (dissociation) pressure of  $\text{IrO}_3$  ( $\text{IrO}_2$ ). (b) X-ray  $\theta$ - $2\theta$  scan of an  $\text{Nd}_2\text{O}_3/\text{Ir}$  mixed-phase film. (c) X-ray  $\theta$ - $2\theta$  scan of an  $\text{Nd}_2\text{Ir}_2\text{O}_7$  amorphous thin film.

**Figure 5.2** (a) Schematic diagram of an  $\text{IrO}_2$  thin film on a  $\text{TiO}_2$  (001) substrate. The  $\text{IrO}_2$  phase becomes Ir metal with a rough surface after Process (1). (b) The sample temperatures ( $T_f$  values) at times  $t$  are shown by the blue solid line. The  $\varepsilon_1$ ,  $\varepsilon_2$ , and the volume fraction of the Ir metal phase (in terms of total film volume;  $P_{\text{Ir}}$ ) were determined with the aid of Maxwell–Garnett theory. Real-time  $P_{\text{Ir}}$  film data acquired during annealing, shown as a bold dotted line. SE spectra of (c)  $\Psi$  and (d)  $\Delta$  collected at various times  $t$  during Process (1). The dielectric functions (e)  $\varepsilon_1$  and (f)  $\varepsilon_2$  at various times  $t$  during Process (1)

**Figure 5.3** (a) Schematic of the  $\text{IrO}_2$  thin film. The film maintained its phase but became thinner due to  $\text{IrO}_3$  formation during Process (2). (b) The sample temperatures  $T_f$  at various times  $t$  are shown as a blue solid line. The real-time thicknesses of the  $\text{IrO}_2$  thin-film during Process (2) are shown as a bold dotted line. SE spectra of (c)  $\Psi$  and (d)  $\Delta$

collected at various times  $t$  during Process (2). The simulated spectral values are shown in (e) and (f). The film thicknesses derived by simulation are shown in (e).

**Figure 5.4** (a) The bold black line indicates temporal variation of growth temperature, switching between 600 °C and 800 °C, during  $\text{Nd}_2\text{Ir}_2\text{O}_7$  thin-film growth. Layers of amorphous  $\text{Nd}_2\text{Ir}_2\text{O}_7$  ( $\text{IrO}_2$ ) were first (after) deposited at 600 °C in the period coloured orange (pink). The deposited layers were annealed at 800 °C for 30 seconds. After the annealing, RHEED (blue bold line) intensity increased due to the crystallization of the layers. The dashed squared process is repeated during the growth. (b) The schematic figures of the procedure of the growth technique. (c) RHEED patterns of each procedure, from the left most to 2<sup>nd</sup> and 3<sup>rd</sup> indicate RHEED patterns of process (I), (II) and (III) of (b) respectively.

**Figure 5.5** Fully strained epitaxial  $\text{Nd}_2\text{Ir}_2\text{O}_7$  thin film a, X-ray  $\theta$ - $2\theta$  scans of the epitaxial  $\text{Nd}_2\text{Ir}_2\text{O}_7$  film grown on (a) YSZ (111) substrate. (b) Reciprocal space map around the (331) diffraction of the YSZ substrate with (662) diffraction of  $\text{Nd}_2\text{Ir}_2\text{O}_7$  thin film. (c) Scanning tunneling electron microscope (STEM) image of a 18-nm-thick  $\text{Nd}_2\text{Ir}_2\text{O}_7$  film. (d) Magnified STEM image at the orange dashed square region in (c). (e) High resolution STEM image of the  $\text{Nd}_2\text{Ir}_2\text{O}_7$  film near the interface shows the sharp interface with pyrochlore ordering of the Nd and Ir sublattices as schematically shown in (e). The fast Fourier transformation (FFT) of the (f) pyrochlore  $\text{Nd}_2\text{Ir}_2\text{O}_7$  thin film and (g) YSZ substrate from the dashed squares region in (c).

**Figure 5.6** Theoretical descriptions on strain induced Weyl semimetallic state. (a),

Structure of the pyrochlore lattice. An Ir atom sits at each vertex of a tetrahedron. Four sites within a tetrahedral unit cell are numbered from 1 to 4. (b), The coordinate of Ir sites depicted with specific crystallographic directions. Tetrahedron lattice deformations are also shown when it gets strained along [111]. (c), The phase diagram where the vertical axis is the electron correlation  $U$  and the horizontal axis is a strain strength along [111] directions. AIAO and 4P (1P) WSM stand for all-in-all-out and four points (one point) Weyl semimetal. (d), Schematic picture of the distribution of Weyl points in the three-dimensional momentum space for 1P WSM.

**Figure 5.7** Strain-induced emergent topological phases (a) Black open (blue filled) circles indicate the temperature-dependent resistivity of the fully relaxed (strained) 80-nm-thick (9-nm-thick)  $\text{Nd}_2\text{Ir}_2\text{O}_7$  thin film. (b) Magnetoresistivity (MR) values of fully strained 9-nm-thick film at various temperatures with  $H // [111]$ . Negative to positive MR change occurs near the  $T_N \sim 15$  K. (c) The schematic figure of magnetic structure of  $\text{Nd}_2\text{Ir}_2\text{O}_7$  in sufficiently strong  $H$ . The Nd-4*f* and Ir-5*d* moments are coupled with the *f*-*d* exchange interaction. (d) MR value with  $H // [111]$  at 2 K of the 9-nm-thick film. It shows MR hysteresis from AIAO/AOAI domain switching.

**Figure 5.8** Large anomalous Hall conductivity. Hall conductivity for a magnetic field along [111] direction at various temperature (a), 2 K, (b), 5 K, and (c), 8 K. The red (blue) lines are Hall conductivity and magnetization on field-increasing (field-decreasing) process.

**Figure 5.9** Evidence for charge pumping through Weyl points. (a), Sketch of two

### *List of figures*

---

massless Weyl points at  $W_+$  and  $W_-$  which have distinct chiralities  $C = +1$  and  $-1$  respectively. (b), Magnetoconductivity in  $H$ -field at various angle. In weak  $H$ , it has the  $H^2$  form predicted in Type-I Weyl semimetal<sup>45</sup>. Inset figure shows the measurement geometry. Angle dependent magnetoconductivity at (c) high and (d) low  $H$ -fields.

# Chapter 1

## Introduction

### 1.1 Correlated topological state in $5d$ transition metal oxides (TMOs)

The combination of two central energy scales, electron-electron correlation ( $U$ ) and spin orbit coupling (SOC), in transition metal oxides (TMOs) play important role for emergent phenomena. In  $3d$  TMOs, a traditional playground for studying strongly correlated electron systems,  $U$  is much larger than electron hopping amplitude,  $t$ , and other scales of solids. Such relatively large  $U$  plays main role in many physical phenomena including local moment formation and magnetism, Mott insulator, correlated metallic states, colossal magnetoresistance, quantum criticality, and high  $T_c$  superconductivity. When the SOC gets much larger than  $U$ , it opens another area for exotic phenomena. Since 2005, the investigation of topological aspects of electron bands has exploded, both theoretically and experimentally [1–3]. From the materials perspective, the domain of the topological insulator (TI) field has mostly been the class of solids with heavy  $s$ - and  $p$ -electron elements, such as Bi, Pb, Sb, Hg, and Te where the SOC is very large.

When TMOs have three comparable energy scales,  $U$ ,  $t$ , and SOC, it induces new intriguing electronic ground state called ‘correlated topological state’. Upon descending the periodic table from the  $3d$  to the  $4d$  to the  $5d$  series, there are several competing trends. First, the  $d$  orbitals become more extended, tending to reduce the  $U$ . However, simultaneously, the SOC increases dramatically, leading to enhanced splitting between otherwise degenerate or nearly degenerate orbitals and bands, in many cases reducing the hopping amplitude. The latter effect can offset the reduction in  $U$ , allowing correlation physics to come into play [4]. In 2011, X. Wan *et al.* [5] theoretically predicted that where the interplay between the  $U$ ,  $t$ , and SOC is comparable to each other, there can be exist Weyl semimetal state. Moreover, by tuning each parameter, it can widely open new topological phases such as Axion insulator and Topological Mott insulator. Overall intriguing ground states in TMOs can be well summarized by general phase diagram in Fig. 1.1.

The first real system which has been predicted to be a Weyl semimetal in real material system is pyrochlore iridate [5]. The pyrochlore iridate which has  $\text{Ir}^{4+}$  valence state with  $5d$  electrons, however it is extremely difficult to synthesize. Therefore, although there were extensive experiment efforts, no clear signature or smoking gun evidence has been observed in pyrochlore iridate. The direct evidence for observing such exotic ground state can be done with angle resolved photoemission spectroscopy (ARPES). If one can observe bulk Weyl points, which appear with linear dispersive Dirac-like band structure, and special surface state called Fermi-arc, it will be the direct evidence that this material have Weyl state.

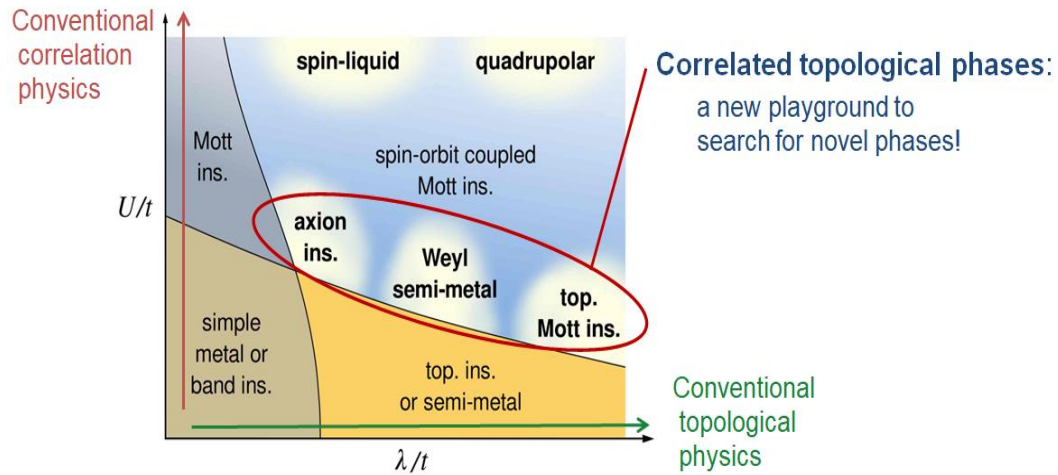


Figure 1.1 Sketch of a generic phase diagram for electronic materials in terms of the interaction strength  $U/t$  and spin-orbit coupling  $\lambda/t$ . [4]

## 1.2 Strain induced topological phase transitions in $5d$ TMO heterostructures

Heterostructure is defined by a combination of multiple interfaces using different materials. This heterostructure shows many exotic properties which are different from the bulk counterparts. For example, by using two different semiconductors which have different band gap structures, two-dimensional electron gas (2DEG) can appear at the interface due to band-bending [6]. Moreover, at the interface of heterostructures, many other interesting phenomena such as quantum hall effect [7], quantum well structure [8], two-dimensional superconductor, and etc. can occur.

Not only the interface effect but also strain effect is another key control parameter

for emergent phenomena in heterostructure. Since spin, charge, and lattice degree of freedoms are strongly coupled in TMOs, strain effect can strongly affect their ground state. For examples, control of physical properties or phases in ferroelectric [9], colossal magnetoresistance [10], superconducting state [11], and etc. by means of symmetry breaking via strain effect. In terms of magnetism and superconductivity, TMOs are ideal playgrounds as they have already demonstrated a wide variety of symmetry breaking [12] arising from strong correlations between electrons.

Since strain effect can breaking the crystal symmetry, and open the new area to study another symmetry broken emergent phenomena such as topologically nontrivial state. Very recently, emergent topological phases via lattice distortion (pressure, strain) were theoretically predicted in *5d* TMOs [13]. However, only a few experimental studies for topological ground state based on the transition-metal oxides have appeared so far due to difficult realization of the high quality samples.

### **1.3 Outline of the thesis**

In this thesis, I will show that *5d* TMOs heterostructure, especially iridates, can be ideal system to study various correlated topological phase. I start with the study on electronic structure of  $\text{IrO}_2/\text{TiO}_2$  thin film which is most simple form of iridate. Next I move on to studies on possible Weyl semimetallic state in pyrochlore iridate by demonstrating epitaxial *in-situ* pyrochlore iridate thin film. With optical spectroscopy and magnetotransport measurements, I will confirm that there are exotic physical phenomena

which only can be shown in topologically nontrivial system (Large Anomalous Hall effect, Negative magnetoconductance, etc.).

## References

- 1 Hasan MZ, Kane CL. Rev. Mod. Phys. **82**, 3045–67 (2010).
- 2 Qi X-L, Zhang S-C. Rev. Mod. Phys. **83**, 1057–110 (2011).
- 3 Hasan MZ, Moore JE. Annu. Rev. Condens. Matter Phys. **2**:55–78 (2011).
- 4 W. W.-Krempa, G. Chen, Y. B. Kim, and L. Balents, Ann. Rev. Condens. Mat. Phys. **5**, 57-82 (2014).
- 5 X. Wan, A. M. Turner, A. Vishwanath, and S. Y. Savrasov, Phys. Rev. B **83**, 205101 (2011).
- 6 J. Tersoff, Phys. Rev. B **30**, 4874(R), (1984).
- 7 R. B. Laughlin, Science **242**, 525 (1988).
- 8 J. J. Paggel et al., Science **283**, 1709 (1999).
- 9 R. T. Resta, Phys. Rev. Lett. **105**, 127601 (2010).
- 10 Y. Lee et al., Nat. Commun. **6**, 5959 (2015).
- 11 J. Engelmann et al., Nat. Commun. **4**, 2877 (2013).
- 12 M.-T. Suzuki et al., Phys. Rev. B **95**, 094406 (2017).
- 13 K. Y. Yang et al., Phys. Rev. B **84**, 075129 (2011).

## **Chapter 2**

### **Experimental detail**

#### **2.1 Pulsed-laser deposition**

For last several decades, lots of fabrication techniques have been developed and advanced to make high-quality thin films [1]. They include molecular beam epitaxy method, on/off-axis sputter, and pulse laser deposition (PLD) method. Among them, PLD is probably the simplest way to make a thin film with high crystalline quality [2]. PLD method offers a very wide range of deposition parameters, such as substrate temperature, oxygen partial pressure, and laser intensity. This flexibility makes the PLD method to be very attractive for investigating the effects of the deposition parameters. For example, it is known that oxide thin films have quite different physical properties, according to deposition conditions. Figure 2.1 shows a schematic diagram of a PLD chamber. It consists of a target holder and a substrate holder housed in a vacuum chamber. The substrate temperature is maintained near room temperature, in order to deposit amorphous and polycrystalline film. However, in most cases, the substrate is heated in order that its temperature is maintained at a certain temperature, high enough to deposit epitaxial film. Epitaxial growth of oxide thin films usually requires a high deposition temperature

( $\geq 500$  °C). A high-power laser is used as an external energy source to ablate the target material and vaporize it. And, a set of optical components is used to focus the laser beam on the target surface. The vaporization process of target material occurs by a congruent melting, and thus the chemical stoichiometry of vapor is almost the same as that of the target material. This means that we can easily make thin film with desired chemical component with PLD method.

The separation between the vacuum control equipment and the laser power source makes the PLD to be so flexible that it is easily adaptable to different operational modes. Film growth can be carried out in a reactive environment containing any kind of gases. Because of the fast and very directional plume, attenuation due to trajectory change as a result of collisions with the background gas is small.

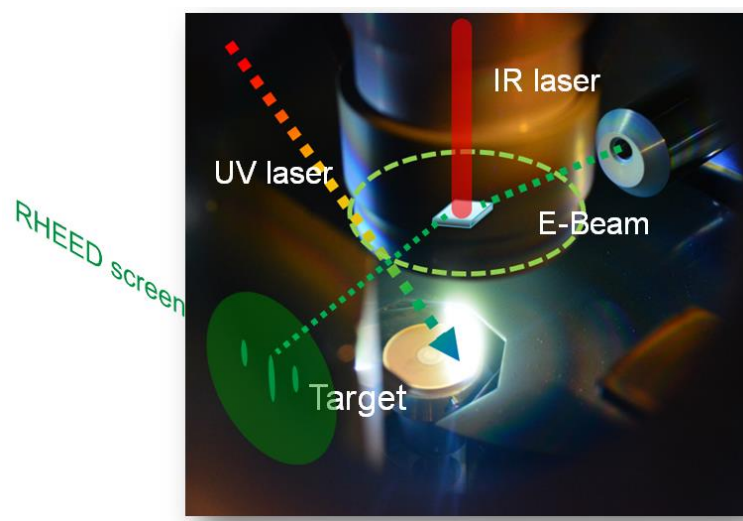


Figure 2.1 Schematic diagram of a PLD chamber. It consists of a target holder and a substrate holder housed in a vacuum chamber.

## 2.2 *In-situ* spectroscopic ellipsometry

Optical investigations of the samples are widely used for determining the electronic properties of various materials including transition-metal oxides, organic conductors, and Si based semiconductors. Spectroscopic ellipsometry (SE) is a type of optical spectroscopy utilizing the fact that reflected light from a sample surface becomes elliptically polarized. From the elliptically polarized light two parameters are obtained, namely amplitude ratio and phase difference between *s*- and *p*- polarized light. Based on these two parameters, optical constants such as  $\tilde{\epsilon}$ ,  $\tilde{\sigma}$  could be directly acquired without Kramers-Kronig relation which is essential in some optical spectroscopies measuring transmittance or reflectance.

When this spectroscopic ellipsometer (J. A. Woollam M-2000-210 *in-situ* instrument) is attached to ultra-high vacuum (UHV) PLD chamber, we can measure the film's optical properties during the deposition or chemical decomposition processes. Our *in-situ* SE apparatus featured a light source and a detector mounted on the outside of the PLD chamber, as shown in Fig. 2.2(a). In the proposed method, light enters the chamber and exits through optical windows. As rapid optical measurements can be performed outside the chamber, the technique can be used to monitor film chemical kinetics *in-operando*. In our experiments, the SE obtained real-time scans from the thin film samples every 10 s over the photon energy spectral range of 0.7–6.5 eV.

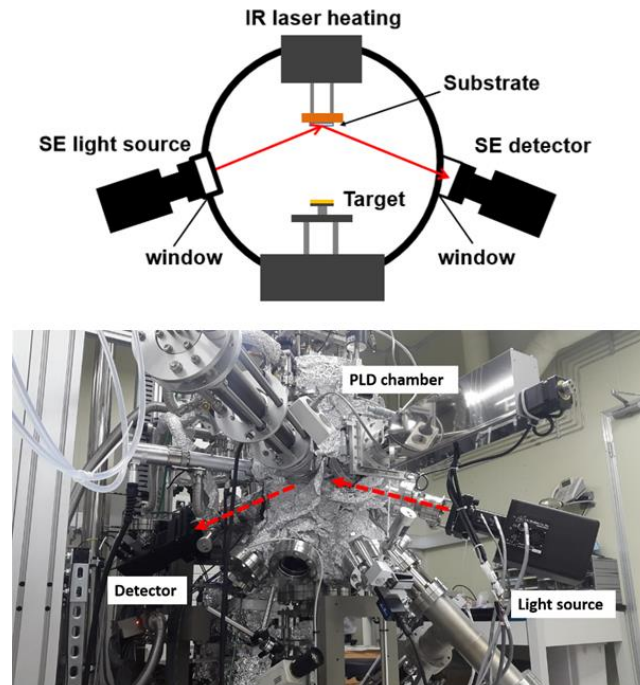


Figure 2.2 (a) Schematic diagram of a PLD chamber with *in-situ* spectroscopic ellipsometry. It consists of a target and a substrate housed in a vacuum chamber. (b) Real photo of Experimental setup for *in-situ* spectroscopic ellipsometry, which is equipped with IR laser heater, ion gauge, variable leakage valve, and M-2000D ellipsometer.

## 2.3 Magnetotransport measurement

The magnetoresistance is consisting of two perpendicular direction, longitudinal magnetoresistance (MR) and Hall resistance. The MR and Hall resistance were measured with use of Physical Property Measurement System (PPMS, Quantum Design Inc.). The electric current was applied parallel to the longest side ( $x$ -axis) and the magnetic field is applied along the  $z$ -axis as shown in Fig.2.3. The electrical resistivity and conductivity are defined by the ratio of the applied current and the induced voltage  $V_{xx}$  as shown in Fig. 2.3, i.e.

$$j = \sigma E$$

and

$$E = \rho j$$

From  $j_y = 0$ , we obtain

$$\rho_{xx} = \frac{E_x}{j_x}$$

The Hall resistivity is defined by the ratio of the applied current and the induced voltage  $V_{xy}$  as shown in Fig. 2.3. Therefore we obtain

$$\rho_{xy} = \frac{E_y}{j_x}$$

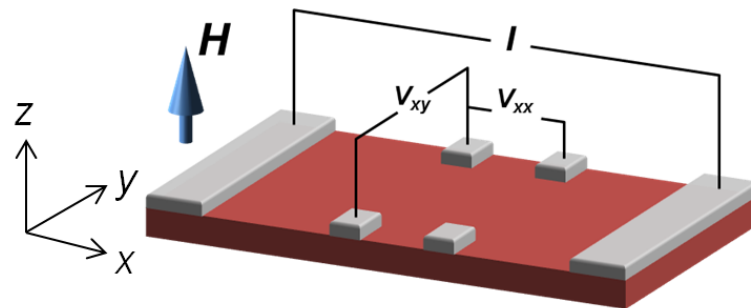


Figure 2.3 Schematic diagram of setup for MR and Hall measurement.

## **References**

1. H. Kitahata, K. Tadanaga, T. Minami, N. Fujimura, and T. Ito, *Jpn. J. Appl. Phys.* **38**, 5448 (1999).
2. D. B. Chrisey and G. K. Hubler, eds., *Pulsed laser deposition of thin films*, John Wiley & Sons, Inc., 1994.

## Chapter 3

# The role of spin orbit coupling in nonsymmorphic IrO<sub>2</sub> thin film and its electronic structure

### 3.1 Introduction

Spin-orbit coupling (SOC) in iridates has attracted much attention due to their intriguing novel ground states as well as potential applications. For example, in Sr<sub>2</sub>IrO<sub>4</sub>, the SOC induces nontrivial electronic properties, such as *5d* Mott insulators [1–3]. With large SOC and electron-electron correlations, pyrochlore iridates are promising candidate materials to realize novel topological phases, such as Weyl semimetals and axion insulators [4–6]. Na<sub>2</sub>IrO<sub>3</sub> is considered to be a useful system for topological quantum computation [7].

Recently, a metallic *5d* IrO<sub>2</sub>, one of the simplest forms of iridium compounds, has gained particular attention among iridates. It has been proposed that IrO<sub>2</sub> can be used as a very good spin detector material, thanks to a large spin Hall angle due to pronounceable SOC and large resistivity [8]. More recently, it was shown that the dominant carrier type can be controlled in the nonsymmorphic IrO<sub>2</sub> films by applied magnetic-field direction [9]. Obviously, a detailed understanding of the role of SOC in the electronic structure of this compound is essential for such novel applications.

The importance of SOC in the electronic structure of IrO<sub>2</sub> has been debated for some time. In the early days, physical properties of IrO<sub>2</sub> had been explained without considering SOC [10–12]. In the 1970s, Graebner *et al.* measured the Fermi-surface topology of IrO<sub>2</sub> by magnetothermal oscillations [13]. To explain the experimental data, Mattheiss used the Slater-Koster linear-combination-of-atomic-orbitals calculation method and found that the Fermi-surface topology was significantly altered by SOC effects [14]. Following these earlier studies, the role of SOC in the electronic structure of IrO<sub>2</sub> has been investigated using a variety of spectroscopic techniques [15–20] and first-principles calculations [9,20–22]. However, the debate on precisely how SOC affects the electronic structure of metallic IrO<sub>2</sub> still remains unsettled.

Another interesting issue in metallic IrO<sub>2</sub> is the possible formation of a novel ground state, called the  $J_{\text{eff}} = 1/2$  state. It has been established recently that the  $J_{\text{eff}} = 1/2$  state can form as a novel ground state in the known insulating iridates, such as Sr<sub>2</sub>IrO<sub>4</sub>, Sr<sub>3</sub>Ir<sub>2</sub>O<sub>7</sub>, and Na<sub>2</sub>IrO<sub>3</sub> [1,2,23–25]. In the presence of a large cubic crystal field, the  $5d$  orbitals are split into  $t_{2g}$  and  $e_g$  levels, and all five electrons should occupy the  $t_{2g}$  levels. When SOC is large,  $t_{2g}$  levels split into effective total angular momentum states: fourfold  $J_{\text{eff}} = 3/2$  and twofold  $J_{\text{eff}} = 1/2$  states. Because the energies of the  $J_{\text{eff}} = 1/2$  states are higher than those of the  $J_{\text{eff}} = 3/2$  states, half of the  $J_{\text{eff}} = 1/2$  states should be occupied [1]. With moderate on-site Coulomb interaction  $U$ , it is possible to form a Mott insulator with the  $J_{\text{eff}} = 1/2$  ground state, which has been confirmed in numerous  $5d$  compounds [1,2,23–25]. Some studies claim that this intriguing  $J_{\text{eff}} = 1/2$  state is applicable even in metallic IrO<sub>2</sub>, although the presence of this state is yet to be confirmed experimentally [9,19–21].

However, due to the itinerant nature and relatively large bandwidth of metallic compounds, other groups argue that the  $J_{\text{eff}} = 1/2$  state is not relevant in  $\text{IrO}_2$  [26–28].

In this chapter, we describe the importance of SOC and the possible formation of the  $J_{\text{eff}} = 1/2$  state in  $\text{IrO}_2$ . To elucidate the roles of SOC, we grew high-quality epitaxial thin films of  $\text{IrO}_2$ . We performed optical and x-ray absorption spectroscopy (XAS) measurements on our samples and compared the data with first-principles calculations with and without SOC contribution. From our optical measurements, we determined that SOC should play an important role in the electronic structure of  $\text{IrO}_2$ , especially near the Fermi surface. SOC causes the degenerate bands to split, especially along the  $ZUR$  line. However, despite its importance, we do not observe the formation of the novel  $J_{\text{eff}} = 1/2$  state in the metallic  $\text{IrO}_2$  from our XAS measurements. The possible orbital state of the unoccupied band near the Fermi energy ( $E_F$ ) would be a mixed state of  $\pi$ -bonding  $d_{yz}$  and  $d_{zx}$  orbitals.

## 3.2 Results and Discussion

### 3.2.1 Experimental details

To fabricate epitaxial  $\text{IrO}_2$  films, we used pulsed laser deposition. We irradiated a single-phase  $\text{IrO}_2$  polycrystalline target with a KrF excimer laser (repetition rate: 3 Hz); the laser fluence at the target surface was  $\sim 1 \text{ J cm}^{-2}$ . The distance between the target and the substrate was maintained at  $\sim 50 \text{ mm}$ . To grow the  $\text{IrO}_2$  films with the (100)

direction normal to the substrate, we used a single-crystal  $\text{TiO}_2$  (100) substrate. The optimal conditions for high-quality  $\text{IrO}_2$  films were stabilized at a substrate temperature  $T_g$  of  $400^\circ\text{C}$  under an oxygen pressure of 50 mTorr. Temperature-dependent resistivity was measured by the conventional four-probe technique from 2 to 300 K in a physical property measurement system (Quantum Design). We used reflectance and spectroscopic ellipsometry measurements to obtain the real parts of  $b$ - and  $c$ -axis optical conductivity  $\sigma_{1b}(\omega)$  and  $\sigma_{1c}(\omega)$ . For 0.74–4 eV,  $\sigma_{1b}(\omega)$  and  $\sigma_{1c}(\omega)$  were directly measured using a V-Vase ellipsometer (J.A. Woollam Co., Lincoln, NE). From 6 to 600 meV, we measured the near-normal reflectance with polarized light parallel to  $b$  and  $c$  crystallographic axes of the sample. We used an in situ gold evaporation technique to minimize experimental error [29]. Then we fitted both the low-energy reflectance spectra and the high-energy  $\sigma_{1b}(\omega)$  and  $\sigma_{1c}(\omega)$  using a model with one Drude peak and four Lorentz oscillators. This fitting process provided us experimental  $\sigma_{1b}(\omega)$  and  $\sigma_{1c}(\omega)$  in the broad energy range. Density functional theory calculation was performed with the generalized gradient approximation (GGA) without and with SOC as implemented in the ELK code. In addition, the linear optical dielectric responses have been calculated within the random-phase approximation. We performed polarization-dependent O 1s XAS measurements at the 2A beamline at the Pohang Light Source (PLS) in the total electron yield mode. To ensure that additional iridium oxidation did not occur on the surface during sample transfer, we performed in situ x-ray photoelectron spectroscopy (XPS) and ex situ XPS studies of Ir 4*f* and 5*p* core levels of  $\text{IrO}_2$  on the same sample. Even after long exposure to air, the *ex-situ* XPS spectra remained the same as the in situ XPS spectra. And they agreed with the XPS data

of bulk  $\text{IrO}_2$  [26]. Therefore, our O 1s XAS spectra contain information only for  $\text{IrO}_2$ , not those from any other oxidation states.

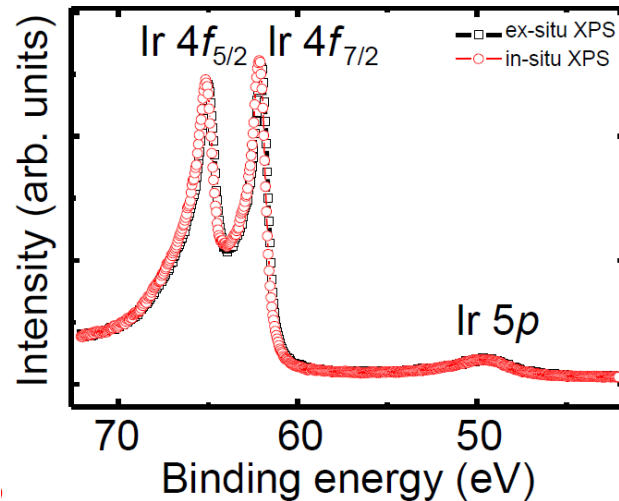


Figure 3.1 Ir 4f core level spectrum from in-situ and *ex-situ* XPS measurements.

### 3.2.2 Structural characterization and transport property

We used x-ray diffraction (XRD) to confirm that our  $\text{IrO}_2$  films were epitaxially grown with lattice parameters close to those of the bulk compound. Figure 3.2(b) shows the XRD  $\theta-2\theta$  scans of our  $\text{IrO}_2$  film, indicating that the film was epitaxially grown without any impurity phases. A film thickness of 11 nm has been estimated based on interference fringes of the film diffraction peak. To measure the in-plane lattice constants of the film and the substrate, we used x-ray reciprocal space mapping (X-RSM). Figures 3.2(c) and 3.2(d) show X-RSM data around the (301) and (310) Bragg reflections,

respectively, of both the IrO<sub>2</sub> film and the TiO<sub>2</sub> substrate. From the experimental  $H$ ,  $K$ , and  $L$  values, the lattice constants of our film are estimated to be  $a = 4.47$ ,  $b = 4.58$ , and  $c = 3.10$  Å. This result indicates that the film is actually partially tensile strained about 1.7% along the  $b$ -axis direction, whereas it is compressive strained about 1.6% along the  $c$ -axis direction. Our X-RSM data also show that the  $a - c$  axes of the IrO<sub>2</sub> film are aligned with the [100], [010], and [001] axes of the TiO<sub>2</sub> substrate, respectively. The resistivity  $\rho$  of our epitaxial IrO<sub>2</sub> film decreases with temperature, in consistence with a metallic ground state. Note that IrO<sub>2</sub> has anisotropic  $\rho$ . We prepared two kinds of electrodes which were aligned along the  $b$  or  $c$  axes and measured the direction-dependent  $\rho$ . Figure 3.2(e) shows the temperature-dependent  $\rho$  along the [010] and [001] directions: the anisotropic values close to those of single crystals. At 300 K,  $\rho$ 's for the  $c$  and  $b$  axes were measured to be 32 and 20  $\mu\Omega$  cm, respectively; the values similar to those of a single crystal, i.e., 49 and 28  $\mu\Omega$  cm, respectively [11]. However, the residual-resistance ratio (RRR)  $\rho(2\text{ K})/\rho(300\text{ K})$  values of our film were around 2 for both  $\rho_b$  and  $\rho_c$ . These values are smaller than those of single crystals but comparable to the values of epitaxial films [9,11] and higher than those previously reported for polycrystalline films [30–36]. The small RRR value might come from lots of misfit dislocations, which inevitably resulted during the growth of the partially relaxed films.

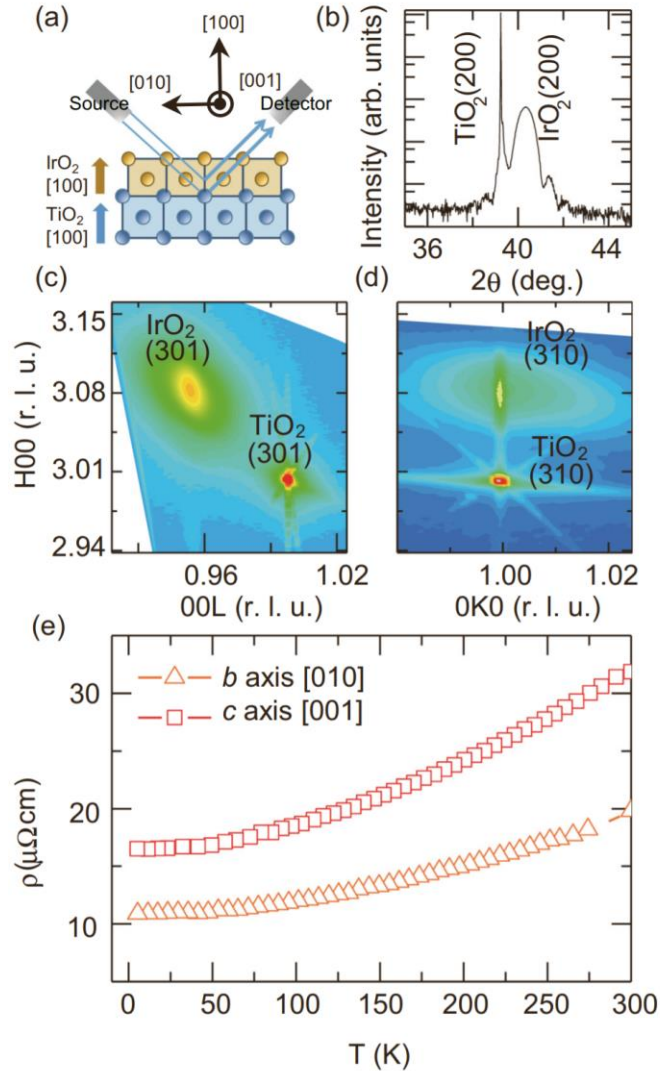


Figure 3.2 (a) X-ray sideways geometry to probe the (200) Bragg peak in the thin film/substrate. (b) X-ray diffraction pattern of IrO<sub>2</sub> grown on (100) TiO<sub>2</sub> substrate. (c) Reciprocal space mapping of (301) IrO<sub>2</sub>. (d) Reciprocal space mapping of (310) IrO<sub>2</sub>. (e) Temperature dependence of resistivity of IrO<sub>2</sub> thin film along [010] and [001] corresponding to the *b* axis and *c* axis, respectively.

### 3.2.3 Optical spectroscopy and first-principles calculations

We observed the free carrier response and several interband transitions in  $\sigma_{1b}(\omega)$  and  $\sigma_{1c}(\omega)$ . Open circles in Figs 2(a) and (b) display the  $\sigma_{1b}(\omega)$  and  $\sigma_{1c}(\omega)$  of our IrO<sub>2</sub> film, respectively. Below 0.2 eV, both spectra show the Drude responses, indicating a metallic state. The inverse values of  $\sigma_{1b}(0)$  and  $\sigma_{1c}(0)$  from fitting are about 64  $\mu\Omega$  cm and 92  $\mu\Omega$  cm, respectively, which are in good agreement with those from the direct *dc* resistivity measurements. In  $\sigma_{1b}(\omega)$ , we observed two strong peaks around 0.4 and 3.5 eV and two small peaks around 1.1 and 2.0 eV. In  $\sigma_{1c}(\omega)$ , we observed two strong peaks around 0.5 and 2.0 eV and an easily discernable peak at  $\sim$  1.1 eV. Earlier optical data on the polycrystalline IrO<sub>2</sub> films reported peak structures around 0.4, 0.9, 1.8, and 3.6 eV, similar to our observations,<sup>17</sup> but could not resolve optical anisotropy. In the earlier studies, all of the peaks below 2.0 eV were assigned to *d* - *d* transitions.

The results of GGA and GGA+SOC calculations using lattice constants of IrO<sub>2</sub> film are shown in Figs. 3.3(d) and (e), respectively. We have confirmed the differences between calculations results from bulk lattice constants and those of film are negligible. Although the general band dispersions in the wide energy regions are similar to each other, SOC causes the degenerate bands to split, especially along the *ZUR* line. Such a splitting could result in additional optical transitions, which might be missing when SOC is not turned on. The dashed and solid lines in Figs. 3.3(a) and (b) are theoretically computed interband component of the  $\sigma_1(\omega)$  values with and without SOC, respectively.  $\sigma_1(\omega)$  values from the experiments show better agreement with those from GGA+SOC

than GGA. Fig. 3.3(a) shows peaks around 0.5, 1.2 and 1.9 eV, in good agreement with experimental  $\sigma_1(\omega)$ . Fig. 3.3(b) also shows reasonable agreement between experimental and GGA+SOC calculation except the lowest peak position, which might be due to the omission of the Drude component in the calculation. While GGA+SOC calculation reproduces most peaks below 3 eV, the GGA calculation fails to reproduce the experimental peaks around 0.4 and 2.0 eV. Particularly, the lowest peak in  $\sigma_{1b}(\omega)$  corresponds to the transition between the two bands along the  $UR$ , which are branched off from the degenerate bands in the absence of SOC. Its peak energy ( $\sim 0.4$  eV) is very consistent with the known value of SOC ( $\sim 0.5$  eV) in iridates. Therefore, we concluded that SOC plays an important role to determine the electronic structure of  $\text{IrO}_2$ , especially near the  $E_F$ .

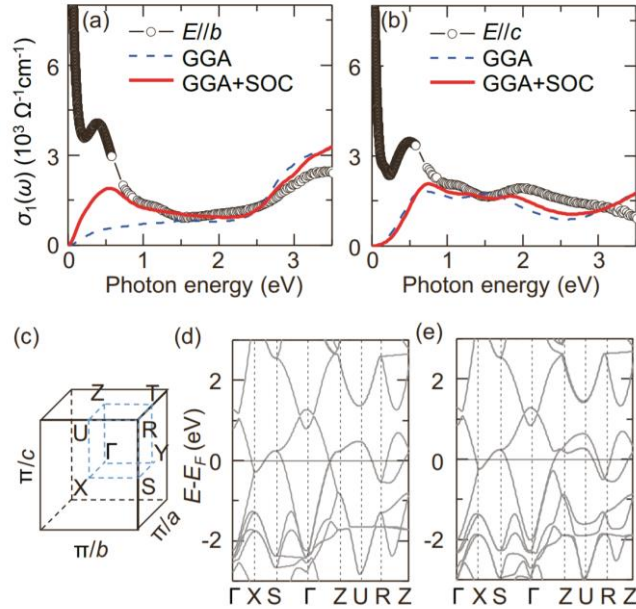


Figure 3.3 (a) Experimental optical conductivity spectra of  $\text{IrO}_2$   $b$  axis [010] (black empty circle) and theoretically computed interband component of the optical conductivity values based on GGA (blue dashed line) and GGA+SOC (red solid line). (b) Experimental optical conductivity spectra of  $\text{IrO}_2$   $c$  axis [001] and theoretically computed interband component of the optical conductivity values based on GGA (blue dashed line) and GGA+SOC (red solid line). (c) Brillouin zone of  $\text{IrO}_2$  film. (d) Band dispersion computed within GGA approximation. (e) Band dispersion computed within GGA+SOC approximation.

### 3.2.4 X-ray-absorption spectroscopy: Orbital character of an empty state near $E_F$

It is still unclear whether metallic  $\text{IrO}_2$  has a  $J_{\text{eff}} = 1/2$  ground state near  $E_F$ . Note that the  $J_{\text{eff}} = 1/2$  can be represented by a combination of three  $t_{2g}$  orbitals,  $(\mp \frac{1}{\sqrt{3}}[|d_{xy} \pm 1/2\rangle \pm |d_{yz} \mp 1/2\rangle + i|d_{zx} \mp 1/2\rangle])$ .<sup>1</sup> So this ground state should be formed with equal contribution of three  $t_{2g}$  orbitals,  $d_{xy}$ ,  $d_{yz}$ , and  $d_{zx}$ . To check the possible formation of  $J_{\text{eff}} = 1/2$  state, we investigated orbital characters of  $\text{IrO}_2$  near the  $E_F$  by using O 1s XAS measurements. The O 1s spectra reflect the transitions from the O 1s core level to the unoccupied O 2p states that are hybridized with Ir 5d orbitals. Since the hybridization varies depending on the extended nature of d orbitals, the polarized XAS spectra can probe the participation of each  $t_{2g}$  orbital in the unoccupied state [37-39].

Figure 3.4(a) shows the experimental geometry of our XAS measurements, where  $\pi$  and  $\sigma$  polarizations were parallel with respect to the  $c$  and  $b$  axes, respectively. Figure 3.4(b) displays the  $\pi$ - and  $\sigma$ -polarization O 1s XAS spectra from 528 to 536 eV, which are normalized by the data at a higher energy region. The O 1s XAS spectra display a sharp peak denoted by  $\alpha$  in Fig. 3.4(b), followed by two broad peaks denoted by  $\beta$  and  $\gamma$ , respectively. Peak  $\alpha$  represents the unoccupied O 2p states hybridized with the Ir  $t_{2g}$  orbital, while peaks  $\beta$  and  $\gamma$  represent those hybridized with  $e_g$  orbitals. These spectra show that  $t_{2g}$  and  $e_g$  states are well separated above  $E_F$ . We found that the orbital character of the empty state near  $E_F$  is not consistent with the formation of the  $J_{\text{eff}} = 1/2$  state. Note that peak  $\alpha$  shows strong polarization dependence: the intensity of  $\pi$  polarization

becomes strongly suppressed compared to that of  $\sigma$  polarization. The intensity ratio of peak  $\alpha$  in  $\pi$  and  $\sigma$  polarizations is estimated to be  $I_\pi/I_\sigma = 0.07$ . To understand the large polarization dependence, we evaluated the intensity ratio in  $\pi$  and  $\sigma$  polarizations for the pure  $J_{\text{eff}} = 1/2$  orbital states. Since the peak intensities reflect the directional hybridization between O  $2p$  and Ir  $5d$  orbitals, we calculated their strength by using the Slater-Koster interatomic matrix [40]. We found that the intensity ratio  $I_\pi/I_\sigma$  should be about 2.9 for the  $J_{\text{eff}} = 1/2$  state. This value is much higher than the experimental value of  $I_\pi/I_\sigma = 0.07$ .

The projected density of states (pDOS) of Ir  $d$  orbitals also confirm that orbital character of IrO<sub>2</sub> does not follow the  $J_{\text{eff}} = 1/2$  orbital picture. Figure 3.4(c) shows the pDOS of Ir  $d$  orbitals in GGA and GGA+SOC calculations. In GGA, two  $t_{2g}$  orbitals,  $d_{xz}$  and  $d_{yz}$ , are responsible for most of the electron density near  $E_F$ . There exists a small peak structure near  $E_F$  around 0.5 eV. Note that this structure can originate from the flat band dispersion near  $E_F$ , along the  $ZU$  line in Fig. 3.3(e) formed due to SOC. However, in both GGA and GGA+SOC calculations, the  $d_{xy}$  orbital has its most of electron density on 2.0 eV below the  $E_F$ . The energy difference between  $d_{xy}$  and the other  $d$  orbitals should be originated from their bonding nature. In the rutile structure, the IrO<sub>6</sub> octahedra have edge sharing, and the  $d_{xy}$  orbital lies within the plane formed by the shared edges and has little mixing with the O  $2p$  orbitals. On the other hand, the  $d_{xz}$  and  $d_{yz}$  orbitals lie perpendicular to the octahedra-edge sharing plane and have a strong  $\pi$ -bonding with O  $2p$  orbitals. The resulting energy difference is about 2 eV, much larger than the SOC energy. Therefore, the  $J_{\text{eff}} = 1/2$  state cannot be formed in IrO<sub>2</sub>.

It was experimentally reported that IrO<sub>2</sub> has a large branching ratio of about 7 in Ir

$L$  edge XAS [19, 41]. They suggested that the large branching ratio might come from formation of the  $J_{\text{eff}} = 1/2$  state. However, our observation of the simple  $\pi$ -bonding states with  $d_{xz}$  and  $d_{yz}$  orbitals near  $E_F$  is seemingly to be inconsistent. It should be noted that large  $\langle L \cdot S \rangle$  values do not have to come from  $J_{\text{eff}} = 1/2$  state. Although SOC is not sufficient to form the  $J_{\text{eff}} = 1/2$  state in  $\text{IrO}_2$ , SOC might be able to mix the  $\pi$ -bonding  $d_{yz}$  and  $d_{zx}$  orbitals to result in the observed large  $\langle L \cdot S \rangle$  values. To confirm this intriguing possibility, some more systematic investigations, including resonant inelastic x-ray scattering or polarization dependent Ir  $L$  edge XAS, are desirable.

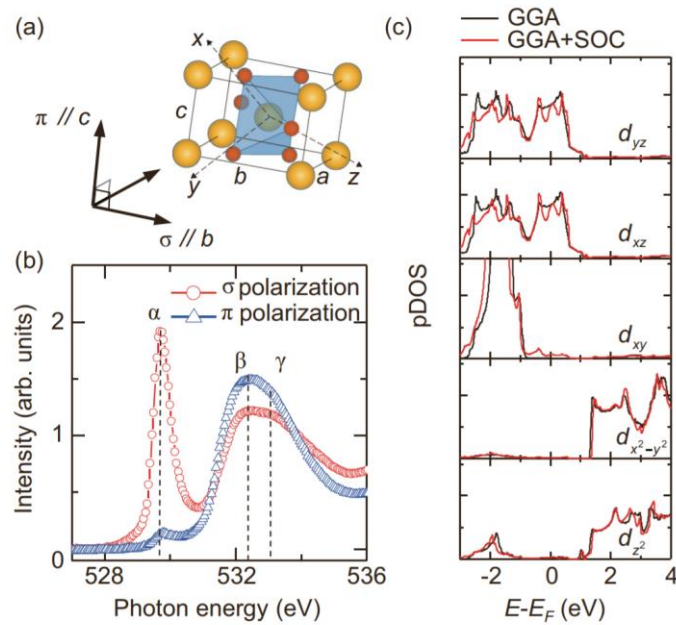


Figure 3.4 (a) Indication of sample orientation and polarized light direction.  $\pi$  and  $\sigma$  polarization light are parallel to  $c$  and  $b$  axes, respectively. (b) O 1s Polarization-dependent X-ray absorption spectroscopy of  $\text{IrO}_2$  grown on (100)  $\text{TiO}_2$  substrate.

Red solid circles and blue solid triangles represent  $\sigma$  polarization and  $\pi$  polarization spectra, respectively. (c) Projected density of state (pDOS) of  $d$  orbitals of  $\text{IrO}_2$ . Black solid line and red solid line represent pDOS calculated using GGA and GGA+SOC, respectively.

### 3.3 Conclusion

At this point, let us revisit the controversies related to SOC in  $\text{IrO}_2$ . First, contrary to our finding that  $J_{\text{eff}} = 1/2$  state cannot be formed in  $\text{IrO}_2$ , there have been some studies that claimed the existence of this novel state in the metallic compound [20, 21]. Note that all of these studies were based on atomic Hamiltonian. So the inconsistency might come from the fact that they did not properly consider the bonding nature of rutile structures in  $\text{IrO}_2$ , which was described in Sec. III.C [42]. As shown in Fig. 3.4(c), the bonding nature moves the  $d_{xy}$  orbital state far below  $E_F$ , i.e. about 2 eV, making it difficult to form the  $J_{\text{eff}} = 1/2$  state. Second, let us discuss on the importance of SOC in  $\text{IrO}_2$ . There have been experimental studies which have good agreement on electronic structure with SOC is turned on. They claimed the importance of SOC by measuring photoemission [15, 18], specific heat [13], and optical properties [16, 17]. However, by using the density functional calculations, other groups claimed that SOC effects are negligible in density of states [27, 28]. Later, hard-X-ray photoelectron spectroscopy experiments supported such a claim [26]. As shown in Fig. 3.4(c), the SOC effects in pDOS are quite small except in the region close to  $E_F$ . And the band dispersion, shown in Figs. 3.3(d) and (e), also shows

that the electronic structural changes due to the SOC should occur close to  $E_F$ . Away from  $E_F$ , SOC effects will become quite small. Therefore, SOC should play important roles mainly in physical properties that are determined by the Fermi surface topology and/or electronic states near  $E_F$ .

In summary, our optical conductivity measurements and the GGA+SOC calculation showed that SOC has an effect on the band structure formation of IrO<sub>2</sub>, close to  $E_F$ . However, O 1s XAS results and pDOS analysis of Ir  $d$  orbitals suggest that  $J_{\text{eff}} = 1/2$  state no longer exists in metallic IrO<sub>2</sub>. Maintaining its metallic state with reasonably strong SOC, IrO<sub>2</sub> epitaxial thin films provide a sufficient environment for electronic transport applications, such as highly sensitive spin detection devices [8].

## References

- 1 B. J. Kim, H. Jin, S. J. Moon, J. Y. Kim, B. G. Park, C. S. Leem, J. Yu, T. W. Noh, C. Kim, S. J. Oh, J. H. Park, V. Durairaj, G. Cao and E. Rotenberg. *Phys. Rev. Lett.* **101**, 076402 (2008).
- 2 B. J. Kim, H. Ohsumi, T. Komesu, S. Sakai, T. Morita, H. Takagi and T. Arima. *Science* **323**, 1329-1332 (2009).
- 3 S. J. Moon, H. Jin, W. S. Choi, J. S. Lee, S. S. A. Seo, J. Yu, G. Cao, T. W. Noh and Y. S. Lee. *Phys. Rev. B* **80**, 195110 (2009).
- 4 A. Shitade, H. Katsura, J. Kuneš, X.-L. Qi, S.-C. Zhang and N. Nagaosa. *Phys. Rev. Lett.* **102**, 256403 (2009).
- 5 D. Pesin and L. Balents. *Nat. Phys.* **6**, 376-381 (2010).
- 6 W. Witczak-Krempa, G. Chen, Y. B. Kim and L. Balents. *Annual Review of Condensed Matter Physics* **5**, 57-82 (2014).
- 7 G. Jackeli and G. Khaliullin. *Phys. Rev. Lett.* **102**, 017205 (2009).
- 8 K. Fujiwara, Y. Fukuma, J. Matsuno, H. Idzuchi, Y. Niimi, Y. Otani and H. Takagi. *Nat. Commun.* **4**, 2893 (2013).
- 9 M. Uchida, W. Sano, K. S. Takahashi, T. Koretsune, Y. Kozuka, R. Arita, Y. Tokura and M. Kawasaki. *Phys. Rev. B* **91**, 241119 (2015).
- 10 W. D. Ryden and A. W. Lawson. *The Journal of Chemical Physics* **52**, 6058-6061 (1970).

- 11 W. D. Ryden, A. W. Lawson and C. C. Sartain. *Phys. Rev. B* **1**, 1494-1500 (1970).
- 12 W. D. Ryden, W. A. Reed and E. S. Greiner. *Phys. Rev. B* **6**, 2089-2093 (1972).
- 13 J. E. Graebner, E. S. Greiner and W. D. Ryden. *Phys. Rev. B* **13**, 2426-2432 (1976).
- 14 L. F. Mattheiss. *Phys. Rev. B* **13**, 2433-2450 (1976).
- 15 R. R. Daniels, G. Margaritondo, C. A. Georg and F. Lévy. *Phys. Rev. B* **29**, 1813-1818 (1984).
- 16 A. K. Goel, G. Skorinko and F. H. Pollak. *Phys. Rev. B* **24**, 7342-7350 (1981).
- 17 W. S. Choi, S. S. A. Seo, K. W. Kim, T. W. Noh, M. Y. Kim and S. Shin. *Phys. Rev. B* **74**, 205117 (2006).
- 18 G. K. Wertheim and H. J. Guggenheim. *Phys. Rev. B* **22**, 4680-4683 (1980).
- 19 J. P. Clancy, N. Chen, C. Y. Kim, W. F. Chen, K. W. Plumb, B. C. Jeon, T. W. Noh and Y.-J. Kim. *Phys. Rev. B* **86**, 195131 (2012).
- 20 Y. Hirata, K. Ohgushi, J.-i. Yamaura, H. Ohsumi, S. Takeshita, M. Takata and T.-h. Arima. *Phys. Rev. B* **87**, 161111 (2013).
- 21 S. K. Panda, S. Bhowal, A. Delin, O. Eriksson and I. Dasgupta. *Phys. Rev. B* **89**, 155102 (2014).
- 22 J. S. de Almeida and R. Ahuja. *Phys. Rev. B* **73**, 165102 (2006).
- 23 D. A. Zocco, J. J. Hamlin, B. D. White, B. J. Kim, J. R. Jeffries, S. T. Weir, Y. K. Vohra, J. W. Allen and M. B. Maple. *J. Phys.: Cond. Matter* **26**, 255603 (2014).

- 24 M. K. Vamshi, S. Nishimoto, V. Yushankhai, A. Stoyanova, H. Kandpal, C. Sungkyun, R. Coldea, I. Rousochatzakis, L. Hozoi and B. Jeroen van den. *New J. Phys.* **16**, 013056 (2014).
- 25 C. H. Sohn, H. S. Kim, T. F. Qi, D. W. Jeong, H. J. Park, H. K. Yoo, H. H. Kim, J. Y. Kim, T. D. Kang, D.-Y. Cho, G. Cao, J. Yu, S. J. Moon and T. W. Noh. *Phys. Rev. B* **88**, 085125 (2013).
- 26 J. M. Kahk, C. G. Poll, F. E. Oropeza, J. M. Ablett, D. Céolin, J. P. Rueff, S. Agrestini, Y. Utsumi, K. D. Tsuei, Y. F. Liao, F. Borgatti, G. Panaccione, A. Regoutz, R. G. Egdell, B. J. Morgan, D. O. Scanlon and D. J. Payne. *Phys. Rev. Lett.* **112**, 117601 (2014).
- 27 M. S. Miao and R. Seshadri. *J. Phys.: Cond. Matter* **24**, 215503 (2012).
- 28 Y. Ping, G. Galli and W. A. Goddard. *J. Phys. Chem. C* **119**, 11570-11577 (2015).
- 29 C. C. Homes, M. Reedyk, D. A. Cradles and T. Timusk. *Appl. Opt.* **32**, 2976-2983 (1993).
- 30 M. A. El Khakani, M. Chaker and E. Gat. *Appl. Phys. Lett.* **69**, 2027-2029 (1996).
- 31 B. R. Chalamala, Y. Wei, R. H. Reuss, S. Aggarwal, B. E. Gnade, R. Ramesh, J. M. Bernhard, E. D. Sosa and D. E. Golden. *Appl. Phys. Lett.* **74**, 1394-1396 (1999).
- 32 J. Hämäläinen, M. Kemell, F. Munnik, U. Kreissig, M. Ritala and M. Leskelä. *Chem. Mat.* **20**, 2903-2907 (2008).
- 33 S.-W. Kim, S.-H. Kwon, D.-K. Kwak and S.-W. Kang. *J. Appl. Phys.* **103**, 023517 (2008).

- 34 C. Wang, Y. Gong, Q. Shen and L. Zhang. *Appl. Surf. Sci.* **253**, 2911-2914 (2006).
- 35 P. C. Liao, W. S. Ho, Y. S. Huang and K. K. Tiong. *J. Mat. Research* **13**, 1318-1326 (1998).
- 36 Y. Liu, H. Masumoto and T. Goto. *Mat. Transactions* **45**, 3023-3027 (2004).
- 37 H.-J. Noh, S. J. Oh, B. G. Park, J. H. Park, J. Y. Kim, H. D. Kim, T. Mizokawa, L. H. Tjeng, H. J. Lin, C. T. Chen, S. Schuppler, S. Nakatsuji, H. Fukazawa and Y. Maeno. *Phys. Rev. B* **72**, 052411 (2005).
- 38 T. Mizokawa, L. H. Tjeng, G. A. Sawatzky, G. Ghiringhelli, O. Tjernberg, N. B. Brookes, H. Fukazawa, S. Nakatsuji and Y. Maeno. *Phys. Rev. Lett.* **87**, 077202 (2001).
- 39 W. B. Wu, D. J. Huang, J. Okamoto, A. Tanaka, H. J. Lin, F. C. Chou, A. Fujimori and C. T. Chen. *Phys. Rev. Lett.* **94**, 146402 (2005).
- 40 J. C. Slater and G. F. Koster. *Physical Review* **94**, 1498-1524 (1954).
- 41 D.-Y. Cho, J. Park, J. Yu and J.-G. Park. *J. Phys.: Cond. Matter* **24**, 055503 (2012).
- 42 J. B. Goodenough. *J. Solid State Chem.* **3**, 490-500 (1971).

## Chapter 4

# Unconventional anomalous Hall effect from antiferromagnetic domain walls of $\text{Nd}_2\text{Ir}_2\text{O}_7$ thin films

### 4.1 Introduction

Both symmetry and the ferroic order inevitably become modified in a ferroic domain wall (DW), triggering new functions and topological properties [1-6]. The discovery of conductive DWs in ferroelectric thin films opened a broad field of research dedicated to understanding the underlying mechanisms, and the fabrication of practical DW-based devices [1-4]. The DWs of certain ferromagnets exhibit topological Hall effects attributable to magnetic skyrmions [5, 6]. However, similar topological properties have yet to be observed in the DWs of antiferromagnets (AFMs). Although there exists a theoretical prediction that a finite anomalous Hall effect (AHE) can arise among AFM DWs with non-vanishing Berry curvatures [7], few experimental studies have investigated this intriguing possibility.

Since Wan *et al.* theoretically proposed the existence of a Weyl fermionic state in AFM-ordered  $\text{Y}_2\text{Ir}_2\text{O}_7$  [8], the rare-earth pyrochlore iridates have attracted great interest [9]. Particularly,  $\text{Nd}_2\text{Ir}_2\text{O}_7$  has been widely studied, due to its closeness to the metal–insulator transition (MIT) [10, 11] and large DW conductance [12]. To discuss the AFM spin structure in detail, consider that  $\text{Nd}_2\text{Ir}_2\text{O}_7$  is composed of two types of tetrahedra, Ir

and Nd sublattices, as shown in Fig. 4.1(a). As shown by the red arrows, all four of the Ir spins at the vertices of a tetrahedron point inward. At the nearest neighboring Ir tetrahedra (not shown), all of the Ir spins should point outward. These results in all-in-all-out (AIAO) ordering of Ir spins, which we refer to as Ir:AIAO. At the same time, the spins in the Nd sublattice have similar magnetic ordering (all-out-all-in), Nd:AOAI, as shown in Fig. 4.1(a). These intriguing magnetic orderings and coupling between two different sublattices play important roles in the physical properties of these materials [8-14].

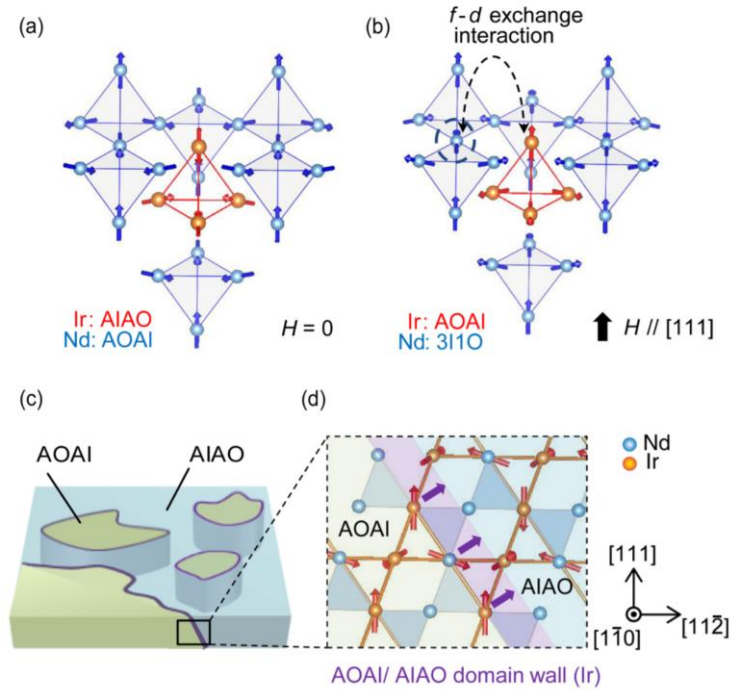


Figure 4.1 Schematic diagrams of the magnetic domain structure of  $\text{Nd}_2\text{Ir}_2\text{O}_7$ . (a) The magnetic structure of Nd  $4f$  moments (blue arrows) and Ir  $5d$  moments (red arrows) at  $H=0$  at temperatures below  $T_N^{\text{Nd}}$ . The Ir and Nd sublattices have all-in-all-out (AIAO) and

all-out-all-in (AOAI) ordering, respectively. (b) The magnetic structure in sufficiently strong  $H$ . The Nd  $4f$  and Ir  $5d$  moments are coupled with the  $f$ - $d$  exchange interaction. (c) Schematic diagram of the domain walls (DWs) between Ir-AIAO and Ir-AOAI. The purple-colored line indicates the possible DW structure with finite magnetization. (d) Schematic diagram of the dotted square region in (c), enlarged for detail. The purple arrows indicate the net magnetization of Ir moments at a DW.

Under an external magnetic field,  $H$ , we can switch between AIAO and AOAI domains of Ir spin. It is important to understand how DWs can be formed during the switching process in a  $\text{Nd}_2\text{Ir}_2\text{O}_7$  sample. Note that the Nd ion has a larger magnetic moment; thus, the corresponding Zeeman field is larger. When  $H$  increases along the  $[111]$  direction, Nd spins become canted and then suddenly flip to form the 3-in-1-out (3I1O) configuration [15]. At a higher  $H$ , Nd spins can induce the flip of Ir sublattice spin into the AOAI configuration via the  $f$ - $d$  exchange interaction [see Fig. 4.1(b)]. During this spin switching process, two kinds of domains may coexist, resulting in the presence of DWs [see Fig. 4.1(c)].

In this chapter we present a  $\text{Nd}_2\text{Ir}_2\text{O}_7$  epitaxial thin film, as an ideal system for realizing the intriguing topological responses that originate from the DWs of an AFM material. The electronic structure of  $\text{Nd}_2\text{Ir}_2\text{O}_7$  has been assumed to be close to that of a Weyl semimetal [8, 16]. This similarity to a semimetallic ground state results in a very large DW conductance [12, 15]. Within a single AIAO or AOAI domain, AHE is forbidden by cubic crystalline symmetry [17, 18]. However, in the presence of the DW,

we will show that two-fold rotation symmetries are explicitly broken, resulting in uncompensated magnetic moments (see Section IV C). This leads to finite anomalous Hall conductivity in the plane parallel to the highly conducting DW. Thus, it will be informative to explore DW-induced unconventional magneto-transport in low-dimensional  $\text{Nd}_2\text{Ir}_2\text{O}_7$  films, in which the contribution of the DW can be maximized [19].

## 4.2 Results and Discussion

### 4.2.1 Sample preparation

#### 4.2.1.1 Deposition of $\text{Nd}_2\text{Ir}_2\text{O}_7$ thin films

We prepared  $\text{Nd}_2\text{Ir}_2\text{O}_7$  (111) films on commercial Y-stabilized  $\text{ZrO}_2$  (YSZ) (111) single-crystal substrates via pulsed laser deposition and following post annealing procedure. We irradiated a single-phase  $\text{Nd}_2\text{Ir}_2\text{O}_7$  polycrystalline target with a KrF excimer laser ( $\lambda = 248$  nm); the laser fluence and frequency were  $4.5 \text{ J/cm}^2$  and 3 Hz, respectively. We maintained the distance between the target and the substrate at 50 mm. It is well known that the pyrochlore iridate thin films are extremely difficult to grow because of volatility of iridium [20-22]. To form the pyrochlore phase thermodynamically, it is required to use a high oxygen pressure and a high temperature [23]. When we try to grow pyrochlore iridate films in such a condition, a gas phase  $\text{IrO}_3$  is likely formed and becomes evaporated, posing extreme difficulties for *in-situ* growth. We initially deposited

stoichiometric  $\text{Nd}_2\text{Ir}_2\text{O}_7$  films on amorphous phase by growing at  $600^\circ\text{C}$ . Then, we post-annealed the films in air in an electrical box furnace at  $1,000^\circ\text{C}$  for an hour [24].

Figure 4.2(a) shows X-ray diffraction (XRD)  $\theta$ - $2\theta$  scans of our  $\text{Nd}_2\text{Ir}_2\text{O}_7$  film and the YSZ substrate. The XRD of film shows only peaks from plane parallel to  $\text{Nd}_2\text{Ir}_2\text{O}_7$  (111) in addition to substrate peaks, indicating that the film is single-phase. Figure 4.2(b) shows the detailed XRD pattern near the  $\text{Nd}_2\text{Ir}_2\text{O}_7$  (222) peak. Figure 4.2(c) shows that the full-width-half-maximum (FWHM) of the rocking curve is  $\sim 0.05^\circ$ , indicating that the sample is highly crystalline. We used X-ray reciprocal space mapping (X-RSM) to measure the in-plane lattice constants of the film and substrate. Figure 4.2(d) shows X-RSM data around the (662) and (331) Bragg reflections of the  $\text{Nd}_2\text{Ir}_2\text{O}_7$  film and YSZ substrate, respectively. The (662) Bragg peak of the  $\text{Nd}_2\text{Ir}_2\text{O}_7$  film has smaller  $Q_x$ - and  $Q_z$ -values than those of the YSZ (331) Bragg peak. From the experimental  $Q_x$ - and  $Q_z$ -values, the lattice constants of our film are estimated to be  $a = b = 10.380 \text{ \AA}$ , close to those of bulk polycrystalline  $\text{Nd}_2\text{Ir}_2\text{O}_7$  ( $a = b = c = 10.375 \text{ \AA}$ ). This indicates that our films have high structural qualities close to the bulk counterparts.

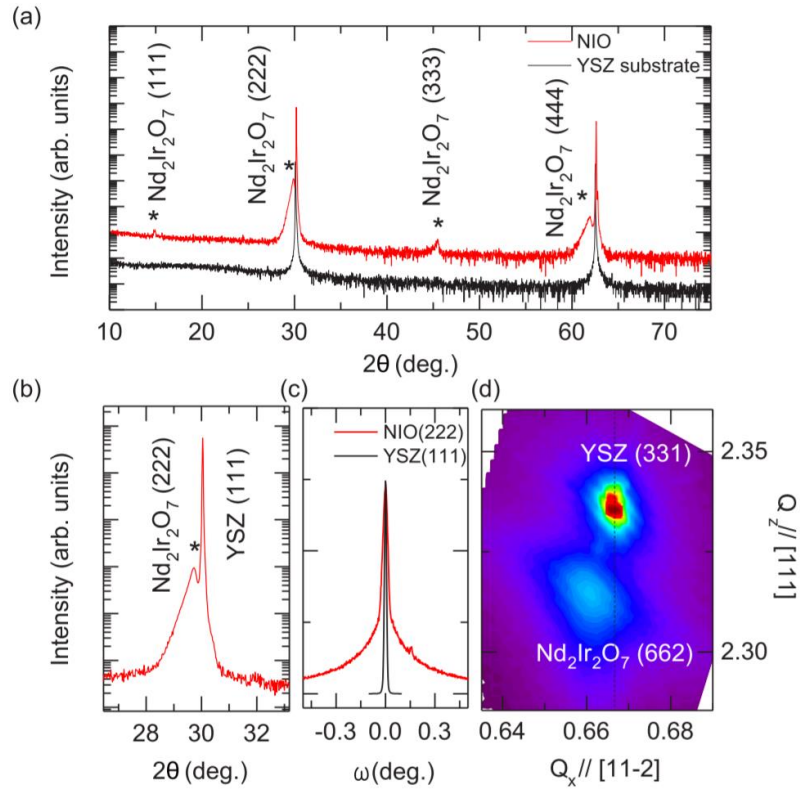


Figure 4.2 (a) X-ray diffraction pattern of an 80-nm-thick  $\text{Nd}_2\text{Ir}_2\text{O}_7$  film grown on a YSZ (111) substrate (red bold line) and the diffraction pattern of the bare YSZ substrate (black bold line). (b)  $\text{Nd}_2\text{Ir}_2\text{O}_7$  (222) diffraction pattern. (c) Rocking curve of  $\text{Nd}_2\text{Ir}_2\text{O}_7$  /YSZ (111) film. (d) Reciprocal space mapping of  $\text{Nd}_2\text{Ir}_2\text{O}_7$  (662).

#### 4.2.1.2 Scanning transmission electron microscopy measurements

We used STEM to explore the microstructure of our  $\text{Nd}_2\text{Ir}_2\text{O}_7$  films. Figure 4.3(a) shows a STEM image of an  $\text{Nd}_2\text{Ir}_2\text{O}_7$  film grown on YSZ (111) with the zone axis parallel to  $[2\bar{1}\bar{1}]$ . A blurry region is evident near the interface between film and substrate, which

may be attributable to defects and/or electron beam damage during STEM measurements. To determine structural relationships, we performed fast Fourier transforms (FFTs) of real-space images of the  $\text{Nd}_2\text{Ir}_2\text{O}_7$  film and the YSZ substrate region [see Figs. 4.3(b) and (c)]. Although our films were grown by post-annealing the amorphous phase, an epitaxial relationship is evident between  $\text{Nd}_2\text{Ir}_2\text{O}_7$  and the YSZ substrate:  $\text{Nd}_2\text{Ir}_2\text{O}_7$  [111] // YSZ [111] and  $\text{Nd}_2\text{Ir}_2\text{O}_7$  [0 $\bar{1}$ 1] // YSZ [0 $\bar{1}$ 1].

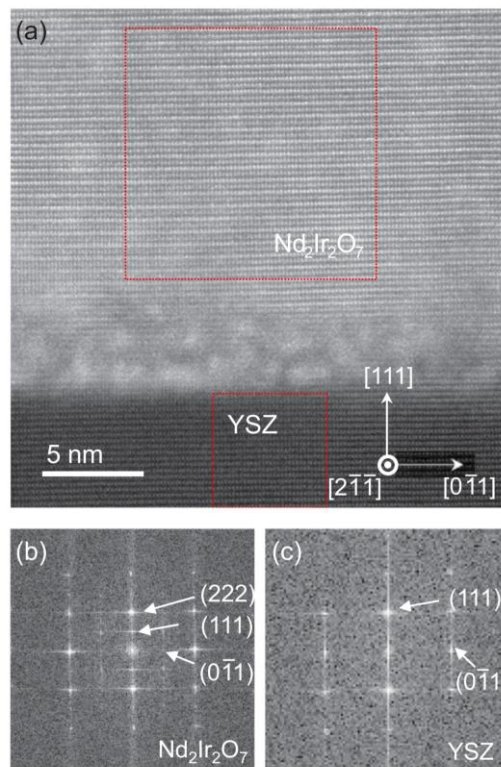


Figure 4.3 (a) Scanning transmission electron microscopy (STEM) image of an  $\text{Nd}_2\text{Ir}_2\text{O}_7$  film grown on YSZ (111) from the viewpoint of the  $[2\bar{1}\bar{1}]$  axis. The  $\text{Nd}_2\text{Ir}_2\text{O}_7$  film exhibits an ordered pyrochlore structure and an epitaxial relationship with the YSZ

substrate. (b) The FFT of the pyrochlore  $\text{Nd}_2\text{Ir}_2\text{O}_7$  thin film (upper red dashed square) and (c) that of the YSZ substrate (downside red dashed square).

### 4.2.1.3 Resistivity and magnetotransport measurements

We measured *dc* magneto-transport properties below  $\sim 14$  T using the standard four-probe method and a commercial cryostat system (Oxford Instruments). For higher *H*-fields up to 30 T, we used the resistive magnet at the National High Magnetic Field Laboratory (NHMFL). During these magneto-transport measurements, we applied current along the  $[1\bar{1}0]$  direction and *H* along the  $[111]$  direction (i.e., perpendicular to the current direction). As shown in Fig. 4.4(a), our 80-nm-thick  $\text{Nd}_2\text{Ir}_2\text{O}_7$  film exhibits a MIT around  $T_N^{\text{Ir}} \sim 30$  K, close to the bulk value. On the other hand, the associated resistivity ratio,  $\rho(2\text{ K})/\rho(300\text{ K})$ , is much broader than that of the ‘best’ single-crystalline sample [15]. The resistivity ratio,  $\rho(2\text{ K})/\rho(300\text{ K})$ , is  $\sim 10$ , which is much smaller than the compared value ( $\sim 1,000$ ) of the single crystal. However, it should be noted that the reported resistivity ratio values in literature varies in a wide range of  $10 \sim 1,000$  even for single crystals [25]. Therefore, our  $\text{Nd}_2\text{Ir}_2\text{O}_7$  films would have crystal quality at least comparable to some single crystals [25].

To measure magneto-resistance (*MR*) behavior, we zero-field-cooled the  $\text{Nd}_2\text{Ir}_2\text{O}_7$  thin film to 2 K and measured resistivity under a constant *H*-field while warming to 300 K. As shown in Fig. 4.4(b), the resistance changes under an *H*-field are large but become smaller as *T* increases, vanishing around  $T_N^{\text{Ir}}$ . Figure 4.4(c) shows *T*-dependent

normalized  $MR$  curves at various  $H$  values. The  $MR$  peaks at  $\sim 15$  K, which corresponds to the Néel ordering temperature of the Nd moment ( $T_N^{\text{Nd}}$ ) [26].

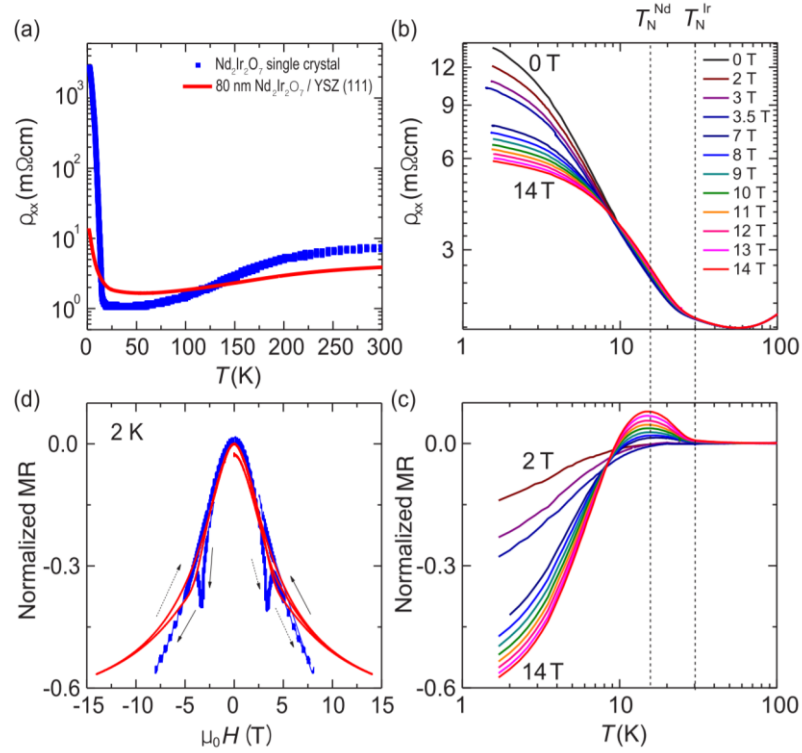


Figure 4.4 (a) Temperature dependence of the longitudinal resistivity  $\rho_{xx}$  of the 80-nm-thick film (red bold line) and its counterpart of single crystal from Ref. [15] (blue square). (b) Temperature dependent magneto-resistance ( $MR$ ) of Nd<sub>2</sub>Ir<sub>2</sub>O<sub>7</sub> for various  $H // [111]$  from 0 T to 14 T. The  $T_N^{\text{Nd}}$  ( $\sim 15$  K) and  $T_N^{\text{Ir}}$  ( $\sim 30$  K) indicate the Néel temperature of the Nd and Ir moments, respectively. (c) Corresponding normalized  $MR$  values versus temperature. When  $H$  is sufficiently large, the gradient of  $MR$  changes from positive to negative at  $T_N^{\text{Nd}}$ . (d) Normalized  $MR$  values with  $H // [111]$  at 2 K of 80-nm-thick film (red bold line) and a single crystal from Ref. [15] (blue square).

## 4.2.2 Antiferromagnetic domain switching

### 4.2.2.1 Magnetoresistance hysteresis

Figure 4.4(d) shows  $H$ -dependent normalized  $MR$  curve at 2 K, where the comparison with the single crystal data in Ref. [15] can be made. Note that it exhibits an intriguing hysteretic behavior with very broad  $MR$  dips around  $\pm 3$  T. This feature is somewhat broad, since it might come from many inherent defects inside the film and pinning of DWs to such defects. However, this hysteretic behavior is essentially similar to that of single crystal, marked by the blue square line. The  $MR$  dips occurs around  $\pm 3$  T, nearly at the magnetic coercive field  $H_C$  of the single crystal [15]. In addition, the hysteresis direction is the same as that in the single crystal data, suggesting that the magnetic hysteresis might come from DW switching.

Such hysteretic behavior is also evident at other temperatures below  $T_N^{\text{Ir}}$ . Figure 4.5(a) shows normalized  $MR$  curves with  $H$  along the [111] direction at various temperatures. The  $MR$  is positive at higher  $T$  but becomes negative around  $T_N^{\text{Nd}} \sim 15$  K [26], consistent with Fig. 4.4(c). Note that the dip structures in  $MR$  hysteresis curve can be easily observed between 5 K and 15 K. And these structures occur at the magnetic fields which are close to the reported  $H_C$  values of single crystals [15]. In the earlier work, the hysteretic  $MR$  behaviors were already attributable to AFM domain-switching [27]. Likewise, we should be able to explain our  $MR$  data in terms of switching between the AIAO and AOAI domains.

### 4.2.2.2 Asymmetric analysis on hysteretic magnetoresistance curves

In the hysteresis curve of a ferroic material, it is well known that the asymmetric  $MR$  part contains important information on magnetic domain switching [24, 28]. We extract the asymmetric part of the normalized  $MR$  curves using

$$MR_{Asym}(H) = \frac{\rho_{xx}(H) - \rho_{xx}(-H)}{2\rho_{xx}(0)}. \quad (1)$$

Figure 4.5(b) shows the  $MR_{Asym}(H)$  curve at 1.8 K with increasing  $H$ -field from  $-30$  to 30 T [only the positive side is plotted, given that  $MR_{Asym}(-H) = -MR_{Asym}(H)$ ]. Note that the  $MR_{Asym}(H)$  curve had interesting structures: a peak at lower  $H$  and a dip at higher  $H$ . Additionally, the curve displayed a sign change in  $MR_{Asym}(H)$  around 3.0 T. Up to our knowledge, these  $MR_{Asym}(H)$  behaviors have not been observed in other magnetic ferroic materials.

Using detailed analysis of the  $MR$  curves, we can obtain insights into spin-ordering and DW dynamics. It is well established in most ferroic materials that domain switching usually occurs at  $H_C$ . When a switching becomes broadened due to pinning of DWs to defects and/or surfaces, the  $H_C$  distribution in DW switching dynamics can be fitted with a Gaussian function [29, 30]. To account for the asymmetry, we fitted our  $MR_{Asym}(H)$  data with an asymmetric Gaussian function:

$$MR_{Asym,FIT}(H) = a(e^{-b(H-H_C)^2} - e^{-b(H+H_C)^2}), \quad (2)$$

where ‘ $a$ ’ and ‘ $b$ ’ are the magnitude and width of the hysteretic behavior, respectively.

We found that the associated sign change in  $MR_{Asym}(H)$  in Fig. 4.5(b) cannot be fit with a single asymmetric Gaussian function in Eq. (2). This indicates that the hysteresis cannot be explained in terms of magnetic switching in one kind of sublattice, i.e., either Ir or Nd spins. On the other hand, when we introduce two magnetic switching functions (namely the two asymmetric Gaussian functions), we are able to fit the experimental  $MR_{Asym}(H)$  curves quite well. In Fig. 4.5(b), we plot the red (blue) line for higher (lower) field magnetic switching. These indicate that both Ir and Nd spins are involved with magneto-transport properties of our  $Nd_2Ir_2O_7$  films.

Considering the  $T_N$  of each ion, we find that the switching at the higher (lower)  $H_c$ -value is a result of the Ir (Nd) sublattice. Figure 4.5(c) shows the temperature dependence of each respective ion's fit coefficient (' $a$ ') calculated from the symmetry analysis of  $MR_{Asym}(H)$  curves. As the temperature decreased, the ' $a$ ' value of the red line first appeared around 30 K ( $\sim T_N^{Ir}$ ). This coincides with Ir spin ordering; thus, we can assign the red line to  $a^{Ir}$ . Likewise, the blue line began to emerge around  $T_N^{Nd}$  and monotonically increased, thus corresponding to  $a^{Nd}$ . Note that the values of  $a^{Ir}$  are larger than those of  $a^{Nd}$ . As the conduction in  $Nd_2Ir_2O_7$  occurs in the Ir-O network [9], it is reasonable to expect Ir spin to dominate the change in  $MR$ . Therefore, the red and blue lines in Fig. 4.5(b) should correspond to switching of spins of Ir and Nd sublattices, respectively.

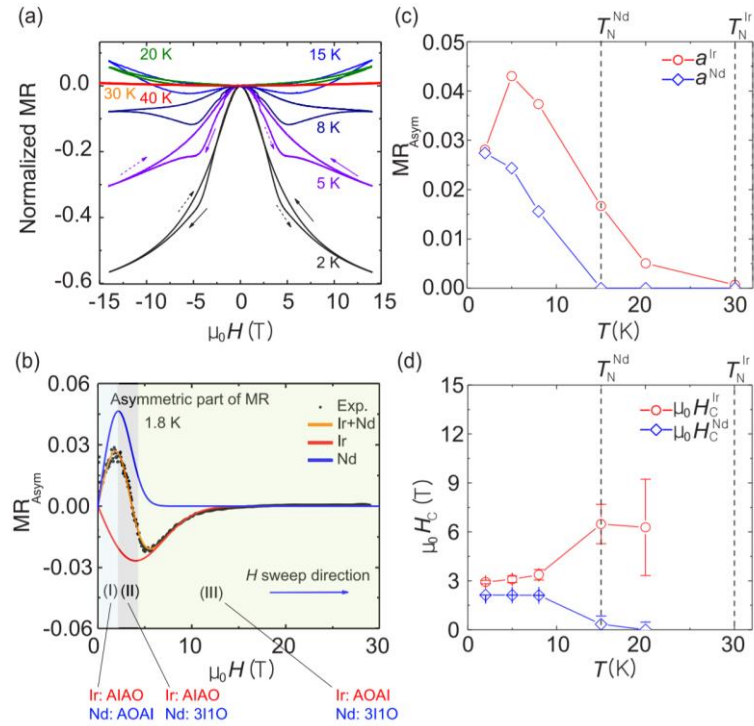


Figure 4.5 (a) Normalized magneto-resistance ( $MR$ ) at various temperatures with  $H // [111]$ . (b) Asymmetric part of sweep-up  $MR$  at 1.8 K (positive  $H$ ). The colored region with Roman numerals corresponds to the represented spin structures. The red (blue) and orange solid lines indicate the hysteretic part of Ir (Nd) domain switching from Eq. (2) and its total contribution to both Nd and Ir, respectively. (c) Quantified fit parameters ‘ $a$ ’ extracted from Eq. (2), where red empty circles (blue empty diamonds) indicate the contribution of hysteretic behavior from Ir (Nd) domain switching. (d) Red empty circles and blue empty diamonds are the coercive fields of the Ir domain and Nd spins, respectively, from  $MR$ . At 30 K, the asymmetric  $MR$  becomes too small to obtain reliable values of the coercive field.

### 4.2.2.3 Domain switching caused by the $f$ - $d$ exchange interaction

Figure 4.5(b) shows that the switching of Nd spins occurred at lower  $H$  than that of Ir spins. Based on the relative values of the switching  $H$ -field, we can summarize the domain switching sequence as follows: (I) at small  $H$ , the Ir-AIAO domains dominate, along with Nd-AOAI spin structures; (II) as  $H$  increases, Nd spins flip first to form Nd-3I1O while the Ir sublattice remains in the Ir-AIAO configuration; and (III) finally, at higher  $H$ , the Nd-3I1O spin structure flips the Ir spins, resulting in the formation of Ir-AOAI domains. This switching sequence is consistent with that was described in Fig. 4.1.

The  $MR$  data also indicate that Ir and Nd spins are strongly coupled, presumably due to the  $f$ - $d$  exchange interaction. From the  $T$ -dependent analysis of  $MR_{Asym}(H)$ , we were able to determine the coercive fields required to switch the spins of each Ir and Nd sublattice. The fitted values for  $\mu_0 H_C^{Nd}$  are shown as blue open diamonds in Fig. 4.5(d). As expected, Nd spin switching did not occur for  $T > T_N^{Nd}$ . Below  $T_N^{Nd}$ ,  $\mu_0 H_C^{Nd}$  increased and remained nearly constant around 2 T. The fitted values for  $\mu_0 H_C^{Ir}$  are shown as red open circles. Ir-AIAO to AOAI domain switching began below  $T_N^{Ir}$ , i.e.,  $H_C^{Ir} \sim 7$  T around 20 K. The  $MR$  signal became small close to  $T_N^{Ir}$ , making it difficult to estimate a value for  $H_C^{Ir}$ . As the temperature decreased,  $\mu_0 H_C^{Ir}$  decreased abruptly below  $T_N^{Nd}$  and then remained nearly constant around 3 T. Note that the extraordinary decrease of  $H_C^{Ir}$  around  $T_N^{Nd}$  cannot occur in magnetic systems with a single magnetic sublattice. This surprising behavior emphasizes the important role of the  $f$ - $d$  exchange interaction in Ir domain switching of the pyrochlore iridate film.

### 4.2.3 Anomalous Hall effects caused by antiferromagnetic

#### 4.2.3.1 Anomalous Hall effects observed in $\text{Nd}_2\text{Ir}_2\text{O}_7$ thin films

We measured the transverse magneto-resistance, i.e., Hall resistivity  $\rho_{xy}$ , of our  $\text{Nd}_2\text{Ir}_2\text{O}_7$  films with  $H$  along the [111] direction. Figure 4.6(a) shows that the  $\rho_{xy}$  curves have a very large and unconventional Hall resistivity behavior. As the temperature decreased below 30 K, hysteretic behavior with a ‘humplike’ peak was observed, which cannot be explained by the conventional ordinary Hall effect. This hysteretic behavior with ‘humplike’ peak intensity became more pronounced as the temperature decreased below  $T_N^{\text{Nd}}$ . Similar ‘humplike’ behavior has been observed in ferromagnetic DWs and has been attributed to the presence of a real-space topological Hall effect related to magnetic skyrmions [5, 6].

To obtain further insight into the AHE, we subtracted the  $H$ -linear ordinary Hall effect term from the 2K  $\rho_{xy}$  data and plotted the data as black solid circles in Fig. 4.6(b). As shown in the figure, the AHE term becomes peaked around 2 ~3 T. The corresponding  $H$  value is close to  $\mu_0 H_C^{\text{Ir}}$  values, obtained from the earlier  $MR$  data analysis. It indicates that a DW could play a significant role in the observed AHE. In addition, the experimental AHE reached a nearly constant value above 5 T, suggesting that bulk effects may also be involved. Taken together, these results suggest that the AHE may have originated from both bulk and DW contributions, hereafter referred to as bulk-AHE and DW-AHE, respectively.

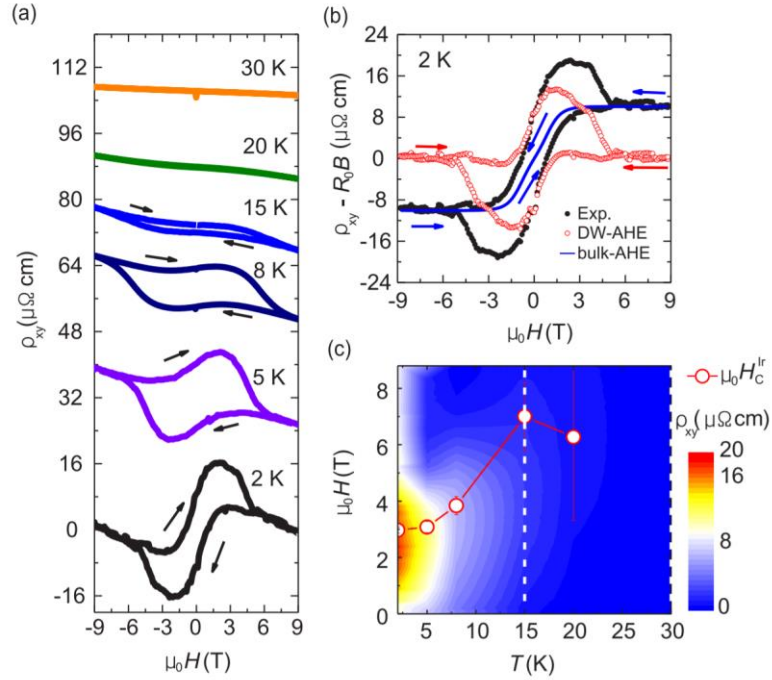


Figure 4.6 (a)  $H$ -dependence of Hall resistivity taken with  $H \parallel [111]$  at various temperatures. The arrows indicate the  $H$  sweep directions. (b) Black empty circles indicate the Hall resistivity at 2 K. The ordinary Hall term is subtracted by linear fitting in the higher  $H$  region. The blue solid lines indicate the contribution of the bulk-anomalous Hall effect (AHE). The red circles indicate the DW-AHE. (c) Color map of anomalous Hall resistivity (ordinary Hall term is subtracted) in the  $T$ - $H$  plane. The red empty circles represent the coercive field  $H_c^{\text{Ir}}$  of Ir domain switching, which are obtained from  $MR$  measurements.

### 4.2.3.2 Bulk AHE of antiferromagnetic material: Scalar spin chirality

For AFM bulk materials, AHEs have been observed and explained in terms of the scalar spin chirality. This term can be defined as  $\vec{S}_i \cdot (\vec{S}_j \times \vec{S}_k)$  with three local spins  $\vec{S}_i$ ,  $\vec{S}_j$  and  $\vec{S}_k$  [31]; the scalar product corresponds to the solid angle subtended by the three spins. The noncoplanar spin configuration is closely linked to the Berry curvature and can generate a fictitious magnetic flux proportional to the scalar spin chirality. As a result, AHE can occur [32-39]. Without a magnetic field, the total magnetization and scalar spin chirality remain zero inside a single  $\text{Nd}_2\text{Ir}_2\text{O}_7$  magnetic domain. However, applying the strong magnetic field changes the order of the Nd moments to 3I1O [see Fig. 4.1(b)] and Ir moments to a canted AIAO. Then, both magnetization and scalar spin chirality become finite, and the canted AFM exhibits finite bulk-AHE.

Now let us estimate  $\rho_{xy}$  values attributable to the bulk-AHE for  $\text{Nd}_2\text{Ir}_2\text{O}_7$ . Note that the AIAO (AOAI) order of the Ir moments is canted by the 1I3O (3I1O) order of the Nd moments via the  $f-d$  exchange interaction. As a result, the scalar spin chirality is produced in the Ir spin system and generates a fictitious magnetic field parallel to its magnetization direction [40]. Moreover, it is well-known that the Nd moments ( $\sim 2.4 \mu_B/\text{Nd}$ ) are much larger than the Ir moments ( $\sim 0.2 \mu_B/\text{Ir}$ ) [15]. As the magnetic moment of Ir is an order of magnitude smaller than that of Nd, the Ir sublattice makes a much smaller contribution to the magnetization. Given that both the scalar spin chirality term of Ir spins and total magnetization are dominated by Nd moments, we will focus on the spin configuration in

Nd tetrahedrons, changing from AIAO to 3I1O. We can quantify the proportions of Nd unit cells in the 3I1O order by calculating the expectation value of magnetization per unit cell. Then we can infer a bulk Hall resistivity curve, which is proportional to the number of Nd unit cells in the 3I1O order.

To quantitatively estimate the  $H$ -dependent net magnetization of the Nd sublattice, we consider the Hamiltonian below, describes a single Nd unit cell under a magnetic field in the direction of the [111] plane:

$$H = -J \sum_{\langle ij \rangle} \vec{S}_i \cdot \vec{S}_j - \mu \vec{B} \cdot \sum_i \vec{S}_i - K \Phi B_x B_y B_z, \quad (3)$$

where  $J$  is the interaction strength,  $\mu$  is the Bohr magneton, and  $\vec{B}$  is magnetic field. The  $K$  is a coefficient and  $\Phi$  is the AIAO order parameter expressed as

$$\Phi = \frac{1}{4\sqrt{3}} (S_{1x} + S_{1y} + S_{1z} + S_{2x} - S_{2y} - S_{2z} - S_{3x} + S_{3y} - S_{3z} - S_{4x} - S_{4y} + S_{4z}). \quad (4)$$

Here, we treat the Nd spin as an Ising variable. The spin vector at each site in a unit cell is defined as  $\vec{S}_1 = \frac{\sigma_1}{\sqrt{3}}(1,1,1)$ ,  $\vec{S}_2 = \frac{\sigma_2}{\sqrt{3}}(1,-1,-1)$ ,  $\vec{S}_3 = \frac{\sigma_3}{\sqrt{3}}(-1,1,-1)$  and  $\vec{S}_4 = \frac{\sigma_4}{\sqrt{3}}(-1,-1,1)$ , where  $\sigma_i = \pm 1$ . Then, the Eq. (3) can be simplified to

$$H = -J \sum_{\langle ij \rangle} \sigma_i \sigma_j - \mu \vec{B} \cdot \sum_i \vec{S}_i - K \Phi B_x B_y B_z. \quad (5)$$

When  $J > 0$ , the ground state of the Hamiltonian in a Nd unit cell is AIAO or AOA1 order without the magnetic field; namely,  $\sigma_i$  are either +1 or -1. As such, the expectation value of the magnetization can be calculated using a partition function. For the unit cell, the partition function is

$$Z = \sum_{\sigma_1, \sigma_2, \sigma_3, \sigma_4 = \pm 1} \exp(-\beta H), \quad (6)$$

and the expectation value of magnetization along [111] direction is

$$\langle M \rangle = \frac{1}{Z} \sum_{\sigma_1, \sigma_2, \sigma_3, \sigma_4 = \pm 1} \left( \sigma_1 - \frac{1}{3} (\sigma_2 + \sigma_3 + \sigma_4) \right) \exp(-\beta H). \quad (7)$$

We evaluated the bulk-AHE of our  $\text{Nd}_2\text{Ir}_2\text{O}_7$  film by assuming that it should be proportional to the magnetization. Given a sufficient  $H$ -field, all of the DWs should disappear, such that the DW-AHE becomes negligible and the bulk-AHE dominates. Using the experimental values of the saturated Hall resistivity value ( $\sim 8 \mu\Omega \text{ cm}$ ) at  $\sim 2 \text{ T}$  ( $\mu_0 H_C^{\text{Nd}}$ ) in Fig. 4.6(b), we derived an analytical estimate of the bulk-AHE contribution. The bulk-AHE contribution is shown as the blue line in Fig. 4.6(b). It should be noted that the bulk-AHE alone cannot explain the experimental AHE. There should be an additional AHE, which cannot be explained by the scalar spin chirality effect or Nd spins. On the other hand, when we introduce two magnetic switching functions (namely the two asymmetric Gaussian functions), we are able to fit the experimental  $MR_{\text{Asym}}(H)$  curves quite well. In Fig. 4.5(b), we plot the red (blue) line for higher (lower) field magnetic switching. These indicate that both Ir and Nd spins are involved with magneto-transport properties of our  $\text{Nd}_2\text{Ir}_2\text{O}_7$  films.

### 4.2.3.3 Emergence of the AHE in the presence of an AFM domain wall: Symmetry analysis

We considered the possible emergence of the AHE due to momentum space Berry curvature by performing symmetry analysis. First, we should note that the anomalous Hall conductivity cannot occur in a single domain of AIAO order in cubic pyrochlore iridates [17]. To calculate the intrinsic anomalous Hall conductivity, we integrate the

Berry curvature of the occupied bands in momentum space:

$$\sigma_{\alpha\beta} = \frac{e^2}{\hbar} \int_{BZ} \frac{d^3k}{(2\pi)^3} \sum_n f(\epsilon_n(\vec{k}) - \mu) F_{\alpha\beta}(\vec{k}), \quad (8)$$

where  $f(\epsilon_n(\vec{k}) - \mu)$  is the Fermi-Dirac distribution, and  $F_{\alpha\beta}$  is the Berry curvature of  $\alpha\beta$  plane. For convenience, we denote each component of the Berry curvature in a vector notation, i.e.,  $F^x(\vec{k}) = F_{yz}(\vec{k})$ ,  $F^y(\vec{k}) = F_{zx}(\vec{k})$ , and  $F^z(\vec{k}) = F_{xy}(\vec{k})$ . When two-fold rotation symmetry around the z-axis ( $C_{2z}$ ) exists, as in the single domain of AIAO (or AOAI) order,  $F^x(-k_x, -k_y, k_z) = -F^x(k_x, k_y, k_z)$ ,  $F^y(-k_x, -k_y, k_z) = -F^y(k_x, k_y, k_z)$ , and  $F^z(-k_x, -k_y, k_z) = F^z(k_x, k_y, k_z)$ . Then  $\sigma_{yz}, \sigma_{zx}$  should be trivial, but  $\sigma_{xy}$  does not have to be trivial through Eq. (8). In a single domain of AIAO order, cubic pyrochlore iridates have  $C_{2x}, C_{2y}$  and  $C_{2z}$  symmetry, thus, AHEs cannot occur.

However, in the presence of a DW, an unconventional AHE can be generated from the non-zero Berry curvature. At the DW, two-fold rotation symmetries become broken but there exists a three-fold rotational symmetry about the axis perpendicular to the DW [see Fig. 7]. Considering the three-fold rotation axis as  $[111]$  and taking the two other perpendicular axes as  $[0\bar{1}1]$  and  $[\bar{2}11]$ , the symmetry properties of the Berry curvature under three-fold rotational symmetry are  $F^x(k_y, k_z, k_x) = F^y(k_x, k_y, k_z)$ ,  $F^y(k_y, k_z, k_x) = F^z(k_x, k_y, k_z)$  and  $F^z(k_y, k_z, k_x) = F^x(k_x, k_y, k_z)$ . Using these properties, we establish the properties of the Berry curvature components along  $[111]$  as

$$F^{[111]}(\vec{k}) + F^{[111]}(C\vec{k}) + F^{[111]}(C^{-1}\vec{k}) \neq 0, \quad (9)$$

where  $C$  is the three-fold rotation operator. Therefore,  $\sigma^{[111]} \neq 0$ , and finite anomalous Hall conductivity can occur in the plane parallel to the DW.

Considering the  $T_N$  of each ion, we find that the switching at the higher (lower)  $H_c$ -value is a result of the Ir (Nd) sublattice. Figure 4.5(c) shows the temperature dependence of each respective ion's fit coefficient (' $a$ ') calculated from the symmetry analysis of  $MR_{Asym}(H)$  curves. As the temperature decreased, the ' $a$ ' value of the red line first appeared around 30 K ( $\sim T_N^{\text{Ir}}$ ). This coincides with Ir spin ordering; thus, we can assign the red line to  $a^{\text{Ir}}$ . Likewise, the blue line began to emerge around  $T_N^{\text{Nd}}$  and monotonically increased, thus corresponding to  $a^{\text{Nd}}$ . Note that the values of  $a^{\text{Ir}}$  are larger than those of  $a^{\text{Nd}}$ . As the conduction in  $\text{Nd}_2\text{Ir}_2\text{O}_7$  occurs in the Ir-O network [9],

#### 4.2.3.4 Unconventional AHE at the antiferromagnetic domain walls of $\text{Nd}_2\text{Ir}_2\text{O}_7$ thin films

When  $H$  is applied parallel to the [111] direction, DWs are expected to form within the (111) plane. Among the possible DW orientations (see Appendix A), in a zero  $H$ -field, the AIAO magnetic ground state favors the formation of DWs within the (111) plane due to its lower frustration compared with other possible orientations [41, 42]. Moreover, a magnetization experiment on  $\text{Cd}_2\text{Os}_2\text{O}_7$  single crystal, another AIAO ordered pyrochlore structure, showed that the plane of DW formation prefers to orient normal to the direction of the applied  $H$  [42]. Thus, in our experimental geometry, DWs with the (111) plane orientation should play a significant role in magneto-transport results.

Figure 4.6(b) shows the  $H$ -dependent  $\rho_{xy}$  at 2 K, from which we subtract the ordinary term that varies linearly with  $H$ . As mentioned earlier, we should interpret this

unconventional Hall resistivity as a combination of the bulk-AHE and the DW-AHE. The bulk-AHE is shown as the blue curve, estimated by following the procedure in Section IV B. To obtain the Hall resistivity attributable to DW-AHE, we subtracted the bulk-AHE from the experimental values. The red circles in Fig. 4.6(b) show the remaining contribution.

Note that the maximum value of the remaining Hall resistivity of  $\Delta\rho_{xy} \sim 15 \mu\Omega \text{ cm}$  is twice as large as the saturated Hall resistivity value of  $\sim 8 \mu\Omega \text{ cm}$ . The obtained maximum value of the red circles ( $\sim 2 \text{ T}$ ) is also in reasonable agreement with  $\mu_0 H_C^{\text{Ir}}$  ( $\sim 3 \text{ T}$ ) from *MR* in which a DW conductance contribution played a significant role. The red circles follow the Gaussian functions used to fit  $MR_{\text{Asym},\text{FIT}}(H)$  [see Eq. (2)]. This implies that broad DW switching occurred upon  $H$ , which is consistent with our *MR* analysis. Moreover, the quadratic dependence of the DW anomalous Hall resistivity on longitudinal resistivity indicates that intrinsic AHEs arose at  $\mu_0 H_C^{\text{Ir}}$  ( $\sim 3 \text{ T}$ ) (see Appendix B). Thus, our results indicate that the ‘humplike’  $\rho_{xy}$  signal originates from the DW-AHE.

Figure 4.6(c) shows a contour plot of the  $\rho_{xy}$ , from which we subtract the ordinary term, as a function of both  $T$  and  $H$ . The contour plot also supports a large enhancement of AHE due to DWs. For a given  $T$ , the  $H$  value at which  $\rho_{xy}$  reaches its maximum is correlated with the value of  $H_c^{\text{Ir}}$  from *MR*. This implies that the large density of DWs near  $H_c^{\text{Ir}}$  can result in a maximized contribution to the AHE. The peak value of the ‘humplike’ Hall resistivity was also highly enhanced below  $T_N^{\text{Nd}}$ , which supports the idea of strong coupling between Ir and Nd sublattices via the  $f$ - $d$  exchange interaction.

It has already been observed experimentally that the DWs of  $\text{Nd}_2\text{Ir}_2\text{O}_7$  have a much

higher conductivity than bulk  $\text{Nd}_2\text{Ir}_2\text{O}_7$ . Their conductivity is approximately one order of magnitude larger [15, 43]. Hence, the DW-AHE may be significantly enhanced in  $\text{Nd}_2\text{Ir}_2\text{O}_7$  thin films. In comparison, Hall data on  $\text{Sm}_2\text{Ir}_2\text{O}_7$  films, in which the DW conductance is lower than that of the bulk [44], do not reveal any hysteretic AHE, as shown in Fig. 10 in Appendix C. This observation also indirectly supports that the hysteretic hump-like AHE observed in  $\text{Nd}_2\text{Ir}_2\text{O}_7$  film originates from DW conduction.

### 4.3 Conclusion

We observed a large AHE in an AFM  $\text{Nd}_2\text{Ir}_2\text{O}_7$  thin film, which was induced mainly by the DWs. The strong  $f$ - $d$  exchange interaction effectively lowers the energy barrier for Ir domain switching, such that a small magnetic field can be used to control the Ir-DW. Eventually, effective Ir-domain switching induces an intrinsic AHE from the Berry curvature at the DW, leading to a large DW-AHE,  $\sim 15 \mu\Omega \text{ cm}$  at 2 K. Given the observation of AHE at DWs, we suggest that  $\text{Nd}_2\text{Ir}_2\text{O}_7$  is a fertile area for the discovery and investigation of new topological phenomena. As the DW-conducting channels of  $\text{Nd}_2\text{Ir}_2\text{O}_7$  are attributable to the fact that the system lies close to the topological Weyl semimetal phase, the observed DW-driven AHE provides additional evidence that the system exhibits novel topological properties.

## References

- 1 J. Seidel, L. W. Martin, Q. He, Q. Zhan, Y.-H. Chu, A. Rother, M. E. Hawkrigde, P. Maksymovych, P. Yu, M. Gajek, N. Balke, S. V. Kalinin, S. Gemming, F. Wang, G. Catalan, J. F. Scott, N. A. Spaldin, J. Orenstein, and R. Ramesh, *Nat. Mater.* **8**, 229-234 (2009).
- 2 D. Meier, J. Seidel, A. Cano, K. Delaney, Y. Kumagai, M. Mostovoy, N. A. Spaldin, R. Ramesh, and M. Fiebig, *Nat. Mater.* **11**, 284-288 (2012).
- 3 W. Wu, Y. Horibe, N. Lee, S.-W. Cheong, and J. R. Guest, *Phys. Rev. Lett.* **108**, 077203 (2012).
- 4 G. Catalan, J. Seidel, R. Ramesh, and J. F. Scott, *Rev. Mod. Phys.* **84**, 119–156 (2012).
- 5 J. Matsuno, N. Ogawa, K. Yasuda, F. Kagawa, W. Koshibae, N. Nagaosa, Y. Tokura, and M. Kawasaki, *Science Advances* **2**, 1600304 (2016).
- 6 X. Z. Yu, Y. Onose, N. Kanazawa, J. H. Park, J. H. Han, Y. Matsui, and Y. Nagaosa, *Nature* **465**, 901-904 (2011).
- 7 E. G. Tveten, T. Müller, J. Linder, and A. Brataas, *Phys. Rev. B* **93**, 104408 (2016).
- 8 X. Wan, A. M. Turner, A. Vishwanath, and S. Y. Savrasov, *Phys. Rev. B* **83**, 205101 (2011).
- 9 W. W.-Krempa, G. Chen, Y. B. Kim, and L. Balents, *Ann. Rev. Condens. Mat. Phys.* **5**, 57-82 (2014).

- 10 K. Matsuhira, M. Wakeshima, R. Nakanishi, T. Yamada, A. Nakamura, W. Kawando, S. Takagi, and Y. Hinatsu, *J. Phys. Soc. Jpn.* **76**, 043706 (2007).
- 11 K. Matsuhira, M. Wakeshima, Y. Hinatsu, and S. Takagi, *J. Phys. Soc. Jpn.* **80**, 094701 (2011).
- 12 E. Y. Ma, Y.-T. Cui, K. Ueda, S. Tang, K. Chen, N. Tamura, P. M. Wu, J. Fujioka, Y. Tokura, and Z.-X. Shen, *Science* **350**, 538 (2015).
- 13 G. Chen and M. Hermele, *Phys. Rev. B* **86**, 235129 (2012).
- 14 Y.-P. Huang, G. Chen, and M. Hermele, *Phys. Rev. Lett.* **112**, 167203 (2014).
- 15 K. Ueda, J. Fujioka, B.-J. Yang, J. Shiogai, A. Tsukazaki, S. Nakamura, S. Awaji, N. Nagaosa, and Y. Tokura, *Phys. Rev. Lett.* **115**, 056402 (2015).
- 16 K. Ueda, J. Fujioka, Y. Takahashi, T. Suzuki, S. Ishiwata, Y. Taguchi, and Y. Tokura, *Phys. Rev. Lett.* **109**, 136402 (2012).
- 17 B.-J. Yang, and N. Nagaosa, *Phys. Rev. Lett.* **112**, 246402 (2014).
- 18 M.-T. Suzuki, T. Koretsune, M. Ochi, and R. Arita, *Phys. Rev. B* **95**, 094406 (2017).
- 19 M. E. Fisher, and A. E. Ferdinand, *Phys. Rev. Lett.* **19**, 169-172 (1967).
- 20 E. H. P. Cordfunke and G. Meyer, *Recl. des Trav. Chim. des Pays-Bas* **81**, 495–504 (1962).
- 21 J. C. Gallagher, B. D. Esser, R. Morrow, S. R. Dunsiger, R. E.A. Williams, P. M. Woodward, D.W. McComb, and F.Y. Yang, *Scientific Reports* **6**, 22282 (2016).

- 
- 22 W. C. Yang, Y. T. Xie, W. K. Zhu, K. Park, A. P. Chen, Y. Losovyj, Z. Li, H. M. Liu, M. Starr, J. A. Acosta, C. G. Tao, N. Li, Q. X. Jia, J. J. Heremans, and S. X. Zhang, *Scientific Reports* **7**, 7740 (2017).
- 23 K. T. Jacob, T. H. Okabe, T. Uda and Y. Waseda, *Electrochim. Acta* **45**, 1963–1971 (2000).
- 24 T. C. Fujita, Y. Kozuka, M. Uchida, A. Tsukazaki, T. Arima, and M. Kawasaki, *Scientific Reports* **5**, 9711 (2015).
- 25 M. Nakayama, T. Kondo, Z. Tian, J. J. Ishikawa, M. Halim, C. Bareille, W. Malaeb, K. Kuroda, T. Tomita, S. Ideta, K. Tanaka, M. Matsunami, S. Kimura, N. Inami, K. Ono, H. Kumigashira, L. Balents, S. Nakatsuji, and S. Shin, *Phys. Rev. Lett.* **117**, 056403 (2016).
- 26 K. Tomiyasu, K. Matsuhira, K. Iwasa, M. Watahiki, S. Takagi, M. Wakeshima, Y. Hinatsu, M. Yokoyama, K. Ohoyama, and K. Yamada, *J. Phys. Soc. Jpn.* **81**, 034709 (2012).
- 27 Under the  $H$ -field, both of spin canting and domain switching can induce  $MR$ . However, the irreversible processes, such as hysteresis, can be explained in terms of the domain switching.
- 28 V. K. Wadhawan, *Introduction to ferroic materials* (CRC Press, 2000).
- 29 K. G. Webbera, H. C. Robinson, G. A. Rossetti, C. S. Lynch, *Acta Mater.*, **56** 2744–9 (2008).
- 30 Z. Zhao, K. Bowman, R. E. García, *J. Am. Ceram. Soc.*, **95** 1619–1627 (2012).
- 31 X. G. Wen, F. Wilczek, and A. Zee, *Phys. Rev. B* **39**, 11413 (1989).

- 32 K. Ohgushi, S. Murakami, and N. Nagaosa, *Phys. Rev. B* **62**, R6065 (2000).
- 33 Y. Taguchi, Y. Oohara, H. Yoshizawa, N. Nagaosa, and Y. Tokura, *Science* **291**, 2573 (2001).
- 34 Y. Taguchi, T. Sasaki, S. Awaji, Y. Iwasa, T. Tayama, T. Sakakibara, S. Iguchi, T. Ito, and Y. Tokura, *Phys. Rev. Lett.* **90**, 257202 (2003).
- 35 P. Bruno, V. K. Dugaev, and M. Taillefumier, *Phys. Rev. Lett.* **93**, 096806 (2004).
- 36 Y. Machida, S. Nakatsuji, Y. Maeno, T. Tayama, T. Sakakibara, and S. Onoda, *Phys. Rev. Lett.* **98**, 057203 (2007).
- 37 N. Nagaosa, J. Sinova, S. Onoda, A. H. MacDonald, and N. P. Ong, *Rev. Mod. Phys.* **82**, 1539 (2010).
- 38 C. Sürgers, G. Fischer, P. Winkel, and H. v. Löhneysen, *Nature comm.* **5**, 3400 (2014).
- 39 S. Nakatsuji, N. Kiyohara, and T. Higo, *Nature* **527**, 212–215 (2015).
- 40 T. Arima, *J. Phys. Soc. Jpn.* **82**, 013705 (2013).
- 41 S. Tardif, S. Takeshita, H. Ohsumi, J. I. Yamaura, D. Okuyama, Z. Hiroi, M. Takata, and T. H. Arima, *Phys. Rev. Lett.* **114**, 147205 (2015).
- 42 H. T. Hirose, J. Yamaura, and Z. Hiroi, *Scientific Reports* **7**, 42440 (2017).
- 43 Z. Tian, Y. Kohama, T. Tomita, H. Ishizuka, T. H. Hsieh, J. J. Ishikawa, K. Kindo, L. Balents, and S. Nakatsuji, *Nat. Phys.* **12**, 134–138 (2016).
- 44 K. Ueda, J. Fujioka, C. Terakura, and Y. Tokura, *Phys. Rev. B.* **92**, 121110(R) (2015).
- 45 S. Onoda, N. Sugimoto, and N. Nagaosa, *Phys. Rev. Lett.* **97**, 126602 (2006).

## Chapter 5

# Strain induced Weyl semimetal state in epitaxial $\text{Nd}_2\text{Ir}_2\text{O}_7$ thin film

### 5.1 Introduction

The strain effect has been a key control parameter for emergent phenomena in heterostructure. Particularly in transition metal oxides (TMOs), spin, charge, and lattice degree of freedoms are strongly coupled; strain effect can strongly affect their ground state. For examples, physical properties and functionalities in ferroelectric [1], colossal magnetoresistance [2], superconducting state [3], etc. can be strongly modulated by strain effect. In terms of magnetism and superconductivity, TMOs are ideal playgrounds as they have already demonstrated a wide variety of symmetry breaking [4] arising from interplay between strain and strong electron correlations ( $U$ ). However for realizing nontrivial topological phases in TMOs, not many studies are done. Since, nontrivial band topology in TMOs are driven by both relativistic spin-orbit coupling (SOC) and  $U$  the actual materials is confined to very narrow choice;  $5d$  compounds mostly. Therefore by means of modulating the lattice and related band structure, strain effect can be good tuning parameter for extending the field of correlated topological phases.

Recently, pyrochlore iridates,  $\text{R}_2\text{Ir}_2\text{O}_7$  (R: rare earth ion) have attracted much of attention due to their similarity to the Weyl semimetallic ground state and associated physical phenomena [5–7].  $\text{R}_2\text{Ir}_2\text{O}_7$  engages in metal-insulator transitions that vary by

R [8,9]. The  $5d$  pyrochlore oxides also exhibit magnetic ground states such as all-in-all-out (AIAO) antiferromagnetic ordering [10–12]. Given such ordering, Wan *et al* theoretically predicted that a Weyl semimetallic ground state should exist [5]. If realized, it would be the first oxide material to show such an exotic topological state; in particular, when deposited as a thin film, new topological states appear that are hidden in the bulk [13–15]. Therefore, numerous theoretical and experimental efforts have been made for both on bulk and film side [5–8,16–20].

In bulk  $R_2Ir_2O_7$ , no Weyl semimetallic state has been observed without implanting dopants or applying external perturbations. Starting from  $Pr_2Ir_2O_7$  which has largest lattice constants among  $R_2Ir_2O_7$ , it is confirmed to have quadratic band crossing (QBC) point near the Fermi level [21]. By changing A-site rare earth to Nd, AIAO magnetic ground state appears which is prerequisite for Weyl state. However simultaneous with magnetic ordering charge gap also opens, and become insulating state [21]. Theoretical studies also support that there are very narrow windows for Weyl semimetallic state in terms of  $U$  and hopping interaction term,  $t$  [21]. Therefore, to observe such exotic topological ground state one has to apply the external perturbations on  $R_2Ir_2O_7$ . They could only observed nontrivial topological phenomena, i.e., large anomalous Hall effect, when they apply large magnetic field ( $\sim 10$  T) [22] or hydrostatic pressure ( $\sim 1$  GPa) [23] on bulk  $R_2Ir_2O_7$ .

On film side of view, very limited studies are done on  $R_2Ir_2O_7$  due to the extreme difficulty of their synthesis. It is known that the pyrochlore phase becomes more stable at higher oxygen pressure  $P_{O_2}$  and temperature  $T$  than the perovskite counterpart [24].

However, due to instabilities of Iridium oxide in high vacuum chamber, where the conditions thin film is deposited, most of the film turned out to form iridium deficient phase [25] or phase segregation [26]. The first epitaxial  $R_2Ir_2O_7$  film growth was succeeded by using the method so-called ‘solid state epitaxy’ [27]. This method starts with growing amorphous  $R_2Ir_2O_7$  films at a low  $T$  and post annealing them with extra  $IrO_2$  powder in a sealed tube to prevent the loss of Iridium [27]. Although such efforts have made some partial success, the Ir metal defect at the interface between the film and substrate prevent to form uniform film quality. Therefore, it is highly desirable to deposit high quality  $R_2Ir_2O_7$  films via an *in-situ* method to gain insights into the role of strain.

Here we propose the new pulsed laser deposition (PLD) method called rapid pulse annealing epitaxy as a reliable and reproducible way to fabricate fully strained  $R_2Ir_2O_7$ . By using this deposition technique, we could achieve to synthesize high quality  $Nd_2Ir_2O_7$  epitaxial thin film on Yttrium stabilized  $ZrO_2$  (YSZ) substrate with the surface normal plane is (111) oriented. The 9-nm-thick  $Nd_2Ir_2O_7$  thin film was compressively strained on in-plane direction. Here, we also present that only a small uniaxial strain ( $\sim 1\%$  lattice change) along [111] can induce large band modulation where insulating  $Nd_2Ir_2O_7$  ground state become Weyl semimetallic state. The resistivity was significantly reduced compared to the fully relaxed 80-nm-thick  $Nd_2Ir_2O_7$  film possibly from large enhanced electron hopping interaction. Moreover, large anomalous Hall effect is observed due to the uncompensated Chern vector from broken cubic symmetry via strain. The longitudinal positive magnetoconductance also depicts signal from charge pumping through chiral anomaly i.e.,  $\sim H^2$  dependence.

## 5.2 Results and Discussion

### 5.2.1 Experimental details

High quality single phase  $\text{Nd}_2\text{Ir}_2\text{O}_7$  films were grown on insulating YSZ substrates by pulsed laser deposition (PLD) equipped with an infrared (IR) laser heating system. An IR laser beam was introduced to the back of a substrate holder (SiC) so that very high substrate temperature ( $\sim 800$  °C) with clean vacuum and very rapid (up to  $\sim 400$  °C  $\text{min}^{-1}$ ) temperature variation were realized during the growth. These are important factors in this study. Stoichiometric poly-crystal  $\text{Nd}_2\text{Ir}_2\text{O}_7$  and  $\text{IrO}_2$  targets were ablated by KrF excimer laser pulses ( $\lambda = 248$  nm, 5 Hz) with an oxygen pressure,  $P_{\text{O}_2}$ , of 50 mTorr. After growth, samples were characterized by a Bruker X-ray diffractometer, a Cypher atomic force microscope (AFM), and a JEOL JEM-ARM200F scanning transmission electron microscope (STEM) with energy dispersive X-ray (EDX) spectrometer.

By using reflection high electron energy diffraction (RHEED) and *in-situ* spectroscopic ellipsometry (SE) we observed layer-by-layer growth mode during the deposition. The RHEED pattern was monitored and the intensity oscillation was recorded for the specularly reflected spot. We measured the *in-situ* optical properties of  $\text{Nd}_2\text{Ir}_2\text{O}_7$  films during the growth via SE (using a J. A. Woollam M-2000-210 *in-situ* model). The light enters into and comes out of the chamber through optical windows. As rapid optical measurements can be performed outside the chamber, the technique can be used to monitor film deposition kinetics *in-operando*. The SE can take real-time scans from the

thin film samples every 10 seconds in the spectral range of 0.7 - 6.5 eV in photon energy.

Longitudinal resistivity and magneto-resistance (MR) were measured with a four-point probe method in a Quantum Design physical property measurement system. We measured MR below applied the magnetic field,  $H \sim 9$  T. During the measurements, we applied current along the [1-10] direction and  $H$  along the [111] direction.

## 5.2.2 Sample preparation

### 5.2.2.1 Difficulties on *in-situ* pyrochlore iridate growth

The multiple oxide phases of iridium present a key difficulty in the growth of such thin film samples. First is the phase segregation due to the  $\text{IrO}_2$  dissociation process [28]. The metallic Ir compound at the interface of a stoichiometric thin film is a good example of such difficulty. The other difficulty stems from the high volatility of Ir, it prefers to form Ir deficient phase such as  $\text{Re}_3\text{Ir}_2\text{O}_7$ . The  $\text{Bi}_3\text{Ir}_2\text{O}_7$  film [25] and  $\text{Nd}_3\text{Ir}_2\text{O}_7$  mixed with the  $\text{Nd}_2\text{Ir}_2\text{O}_7$  film are examples of Ir deficient phase of stoichiometric pyrochlore iridates thin films as shown in Fig. 5.1. To grow stoichiometric pyrochlore iridates films one has to suppress those processes.

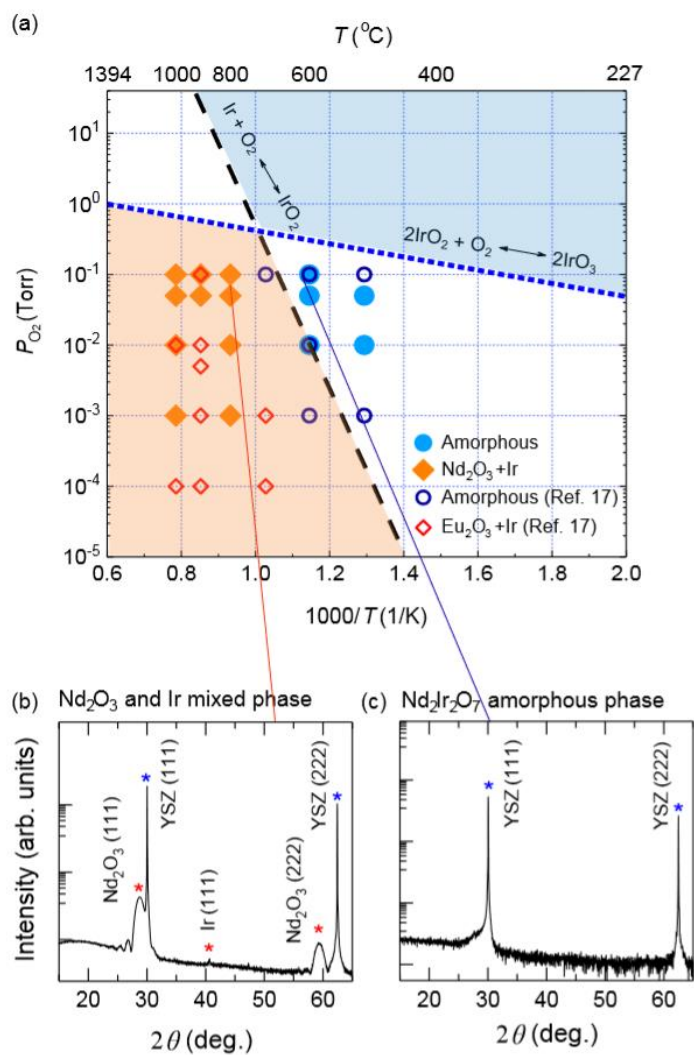


Figure 5.1 (a) Phase diagram of  $R_2Ir_2O_7$  (R: rare earth atoms) film growth. The solid blue (dashed black) line indicates the vapor (dissociation) pressure of  $IrO_3$  ( $IrO_2$ ). (b) X-ray  $\theta$ - $2\theta$  scan of an  $Nd_2O_3$ /Ir mixed-phase film. (c) X-ray  $\theta$ - $2\theta$  scan of an  $Nd_2Ir_2O_7$  amorphous thin film.

Our previous study finds the critical thermodynamic condition where these chemical kinetic occur [29]. At a high temperature ( $\sim 800^\circ\text{C}$ ) under a low  $P_{\text{O}_2}$  ( $\sim 50$  mTorr), over 50% of as-grown  $\text{IrO}_2$  thin films underwent  $\text{IrO}_2$  dissociation in less than 20 s as shown in Fig. 5.2. At the same  $T$  but at a higher  $P_{\text{O}_2}$  ( $\sim 20$  Torr), most of the sample gave rise to  $\text{IrO}_3$  gas within  $\sim 150$  s as shown in Fig. 5.3. The phase diagram for *in-situ*  $\text{Nd}_2\text{Ir}_2\text{O}_7$  in [Ref. 30] show that  $< 800^\circ\text{C}$   $\text{IrO}_2$  dissociation and  $\text{IrO}_3$  gas formation is suppressed. However, when the growth temperature  $T_g < 700^\circ\text{C}$  sample forms as amorphous phase. Therefore to crystallize the film, it is inevitable to increase  $T_g$  at least higher than  $800^\circ\text{C}$ .

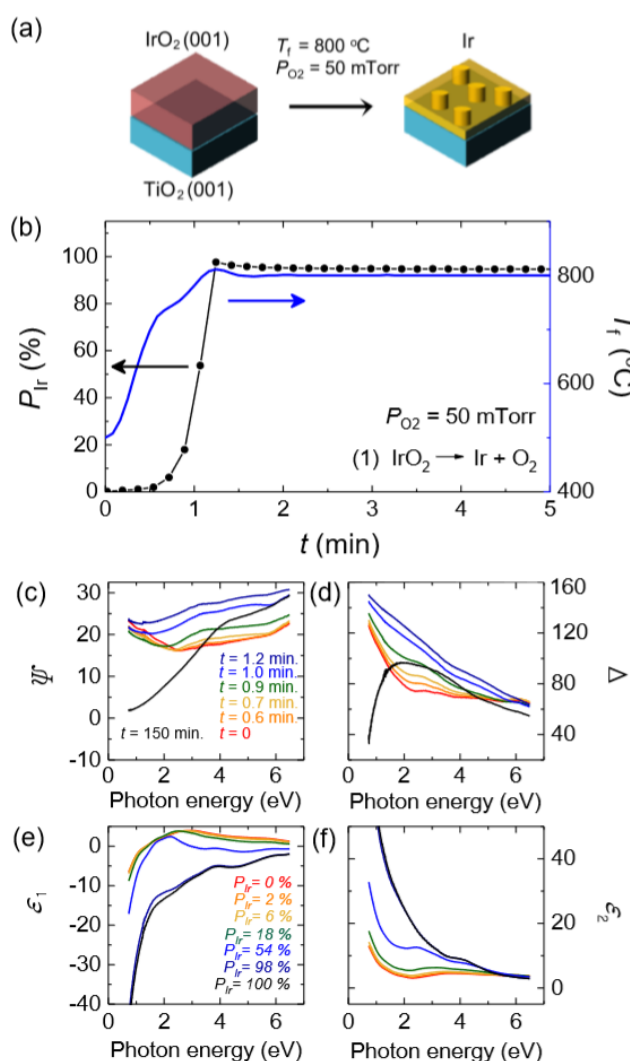


Figure 5.2 (a) Schematic diagram of an  $\text{IrO}_2$  thin film on a  $\text{TiO}_2(001)$  substrate. The  $\text{IrO}_2$  phase becomes Ir metal with a rough surface after Process (1). (b) The sample temperatures ( $T_f$  values) at times  $t$  are shown by the blue solid line. The  $\epsilon_1$ ,  $\epsilon_2$ , and the volume fraction of the Ir metal phase (in terms of total film volume;  $P_{\text{Ir}}$ ) were determined with the aid of Maxwell–Garnett theory. Real-time  $P_{\text{Ir}}$  film data acquired during annealing, shown as a bold dotted line. SE spectra of (c)  $\Psi$  and (d)  $\Delta$  collected at various times  $t$  during Process (1). The dielectric functions (e)  $\epsilon_1$  and (f)  $\epsilon_2$  at various times  $t$  during Process (1)

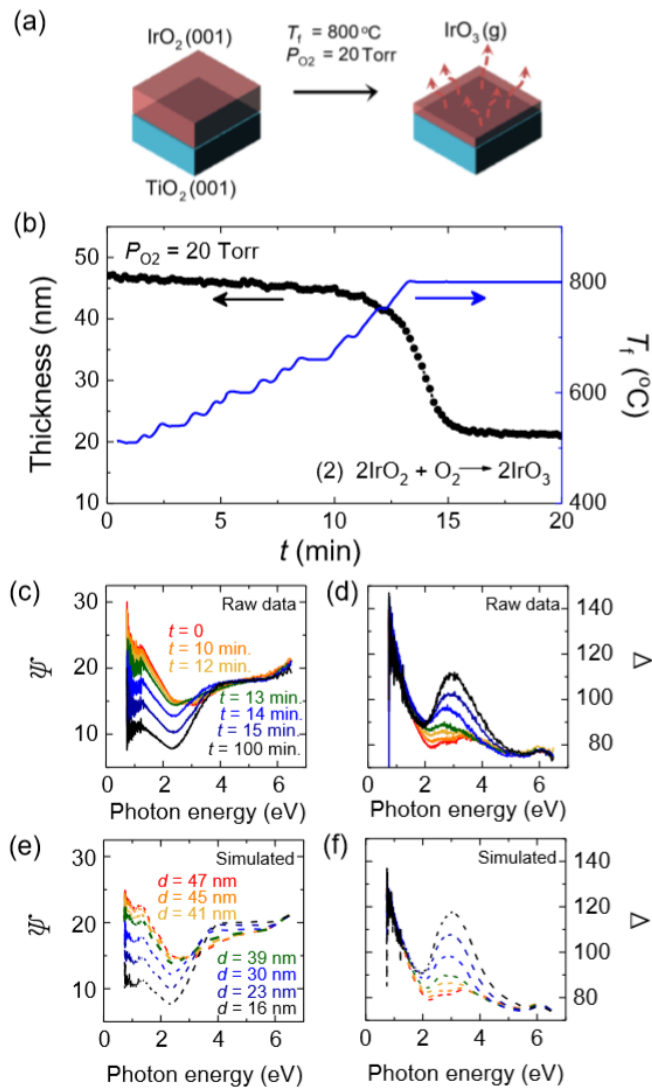


Figure 5.3 (a) Schematic of the IrO<sub>2</sub> thin film. The film maintained its phase but became thinner due to IrO<sub>3</sub> formation during Process (2). (b) The sample temperatures  $T_f$  at various times  $t$  are shown as a blue solid line. The real-time thicknesses of the IrO<sub>2</sub> thin-film during Process (2) are shown as a bold dotted line. SE spectra of (c)  $\Psi$  and (d)  $\Delta$  collected at various times  $t$  during Process (2). The simulated spectral values are shown in (e) and (f). The film thicknesses derived by simulation are shown in (e).

### 5.2.2.2 Rapid pulse annealing epitaxy

We used ‘rapid pulse annealing epitaxy’ technique during the deposition to suppress the kinetic instabilities such as  $\text{IrO}_2$  dissociation and  $\text{IrO}_3$  formation. The main idea of this special technique is providing minimal annealing time for pyrochlore phase formation by applying pulsed thermal energy. At  $T_g \sim 800^\circ\text{C}$  in low  $P_{\text{O}_2}$  ( $\sim 50$  mTorr),  $\text{IrO}_2$  dissociation will occur in very fast timescale. If we can achieve  $T_g \sim 800^\circ\text{C}$  in very short time and cool down fast as well, we might find the phase space where we will highly suppress the  $\text{IrO}_2$  dissociation process but will have enough time to stabilize pyrochlore structure.

This rapid pulse annealing technique we used consists of three key steps. First, we deposit Ir excessive amorphous  $\text{Nd}_2\text{Ir}_2\text{O}_7$  layer on YSZ (111) substrate via dual target ablation. As shown in Fig. 1a, orange color filled square region followed by pink color filled square correspond to laser ablation of 80 pulses on  $\text{Nd}_2\text{Ir}_2\text{O}_7$  target and 180 pulses of  $\text{IrO}_2$  target respectively. During the deposition, growth temperature,  $T_g$ , was maintained at  $600^\circ\text{C}$  in  $P_{\text{O}_2} \sim 50$  mTorr (see a black solid line in Fig. 1a). Second, we crystallized the deposited amorphous layer by using IR laser heating. As shown in a dashed squared region in Fig. 1a, right after the  $\text{IrO}_2$  ablation, with rapid ramping rate  $\sim 400^\circ\text{C min}^{-1}$ , we increased  $T_g$  to  $800^\circ\text{C}$ . We maintained the  $T_g = 800^\circ\text{C}$  for 30 s and cooled the substrate to  $600^\circ\text{C}$  with ramping rate  $\sim 400^\circ\text{C min}^{-1}$ . At last, for the last procedure, we repeated the first and the second steps and deposited the film until desired thickness. The schematic summary of the first and the second procedure is shown in Fig. 1b (II) and (III)

respectively.

RHEED pattern during the deposition shows that after each step of the growth technique [a dashed square region in Fig. 5.4(a)] leave two-dimensional crystalline structure on the substrate. Figure 1b (I) shows the RHEED pattern of YSZ (111) substrate where the direction of electron beams are parallel to [10-1]. The (0-1) RHEED peak intensity oscillation was recorded during the deposition [see a blue solid line in Fig. 5.4(a)]. The RHEED intensity in Fig. 5.4(a) abruptly decreased right after target ablations, indicating that the amorphous layer is deposited on the substrate. Figure 5.4(b) (II) also confirms the deposition of the amorphous layer that RHEED intensity becomes dimmer. Note that after the IR laser annealing procedure, the RHEED intensity becomes increased. This indicates that the amorphous layer became crystallized after the pulse annealing. Moreover, the RHEED peaks pattern in Figure 5.4(c) (III) show additional peaks between (0-1) and (00), (00) and (01) peaks of the YSZ substrate. Considering that the lattice parameter of a cubic unit cell of bulk  $\text{Nd}_2\text{Ir}_2\text{O}_7$  ( $a = b = c = 10.37 \text{ \AA}$ ) [26] is  $\sim$  twice larger than that of YSZ ( $a = b = c = 5.14 \text{ \AA}$ ), the additional RHEED peaks indicate the formation of pyrochlore. The line shapes of the additional peaks indicate that this crystalline layer has a flat surface (or two-dimensional growth). The periodic intensity change of RHEED indicates that this two-dimensional growth mode is maintained during the growth.

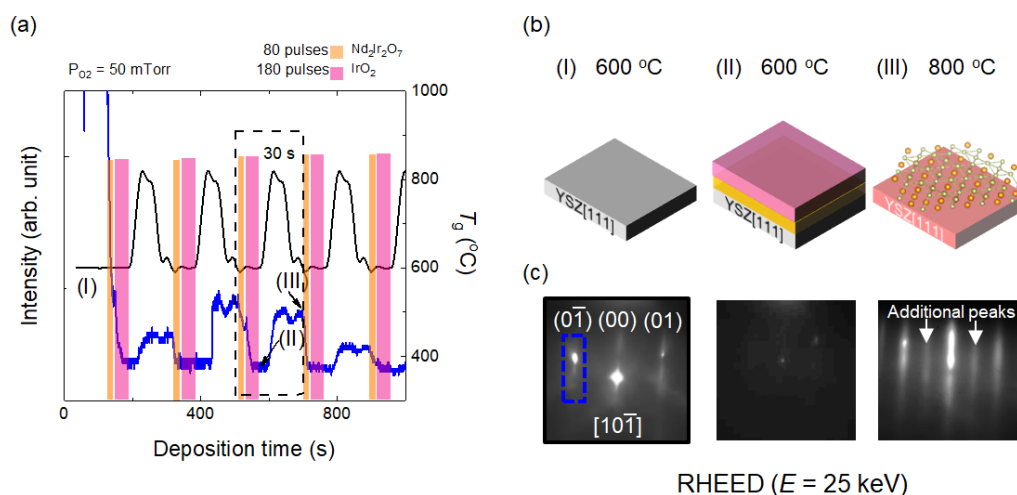


Figure 5.4 (a) The bold black line indicates temporal variation of growth temperature, switching between 600 °C and 800 °C, during  $\text{Nd}_2\text{Ir}_2\text{O}_7$  thin-film growth. Layers of amorphous  $\text{Nd}_2\text{Ir}_2\text{O}_7$  ( $\text{IrO}_2$ ) were first (after) deposited at 600 °C in the period coloured orange (pink). The deposited layers were annealed at 800 °C for 30 seconds. After the annealing, RHEED (blue bold line) intensity increased due to the crystallization of the layers. The dashed squared process is repeated during the growth. (b) The schematic figures of the procedure of the growth technique. (c) RHEED patterns of each procedure, from the left most to 2<sup>nd</sup> and 3<sup>rd</sup> indicate RHEED patterns of process (I), (II) and (III) of (b) respectively.

### 5.2.2.3 Sample characterization

After the 39-cycles of repeated pulse annealing procedure, we took out the sample from the chamber and measured X-ray diffraction (XRD). The XRD results show that our *in-situ* grown thin film shows a single phase  $\text{Nd}_2\text{Ir}_2\text{O}_7$  structure with compressively

strained in-plane lattice. Figure 5.5(a) shows XRD  $\theta$ - $2\theta$  scans of our  $\text{Nd}_2\text{Ir}_2\text{O}_7$  film and the YSZ substrate. The XRD of the film shows only peaks from a plane parallel to  $\text{Nd}_2\text{Ir}_2\text{O}_7$  (111) in addition to substrate peaks, indicating that the film has single-phase. The film peak shows clear thickness fringes, indicating that the thickness of the film is  $\sim 9$  nm. Figure 5.5(b) shows X-ray reciprocal space mapping (X-RSM) data around the (662) and (331) Bragg reflections of the  $\text{Nd}_2\text{Ir}_2\text{O}_7$  film and YSZ substrate, respectively. The (662) Bragg peak of the  $\text{Nd}_2\text{Ir}_2\text{O}_7$  film has same the  $Q_x$ -value and smaller  $Q_z$ -values than those of the YSZ (331) Bragg peak. From the experimental  $Q_x$ - and  $Q_z$ -values, the in-plane lattice constants of our film are same as YSZ which means the film is fully strained ( $\sim 1\%$  compressive strain).

We utilize STEM to explore the microstructure of 18-nm-thick  $\text{Nd}_2\text{Ir}_2\text{O}_7$  thin films. Figure 5.5(c) shows a STEM image of an  $\text{Nd}_2\text{Ir}_2\text{O}_7$  thin film on a YSZ (111) substrate with the zone axis parallel to [1-10]. The clear interface between the film and the substrate is observed. Also, the film has a uniform thickness in the overall long-range region. Figure 5.5(d) is magnified image of an orange dashed squared region in Fig. 5.5(c). The entire region of the film shows that there are no structural defects or disorder structure. As shown in Fig. 5.5(e), this contrast in the images of the  $\text{Nd}_2\text{Ir}_2\text{O}_7$  film is characteristic of a high degree of pyrochlore ordering. The most intense atomic columns contain only Ir atoms ( $Z=77$ ), while the least intense contain only Nd ( $Z=60$ ), and the columns of intermediate contrast are alternating Nd and Ir atoms with 1:1 ratio. To determine structural relationships, we perform fast Fourier transforms (FFTs) of real-space images of the  $\text{Nd}_2\text{Ir}_2\text{O}_7$  thin film and the YSZ substrate region [see Figs. 5.5(f) and

(g)]. An epitaxial relationship is evident between  $\text{Nd}_2\text{Ir}_2\text{O}_7$  and the YSZ substrate:  $\text{Nd}_2\text{Ir}_2\text{O}_7$  (111) // YSZ (111) and  $\text{Nd}_2\text{Ir}_2\text{O}_7$  (002) // YSZ (002).

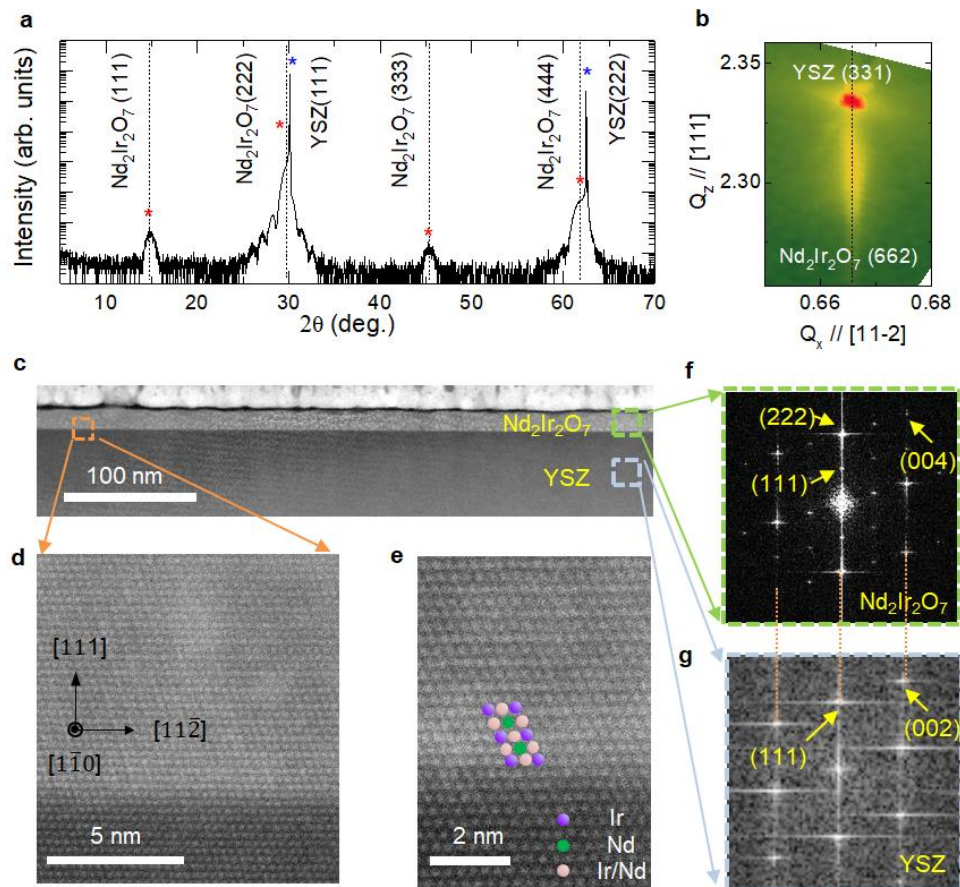


Figure 5.5 Fully strained epitaxial  $\text{Nd}_2\text{Ir}_2\text{O}_7$  thin film a, X-ray  $\theta$ - $2\theta$  scans of the epitaxial  $\text{Nd}_2\text{Ir}_2\text{O}_7$  film grown on (a) YSZ (111) substrate. (b) Reciprocal space map around the (331) diffraction of the YSZ substrate with (662) diffraction of  $\text{Nd}_2\text{Ir}_2\text{O}_7$  thin film. (c) Scanning tunneling electron microscope (STEM) image of a 18-nm-thick  $\text{Nd}_2\text{Ir}_2\text{O}_7$  film. (d) Magnified STEM image at the orange dashed square region in (c). (e) High resolution STEM image of the  $\text{Nd}_2\text{Ir}_2\text{O}_7$  film near the interface shows the sharp interface with

pyrochlore ordering of the Nd and Ir sublattices as schematically shown in (e). The fast Fourier transformation (FFT) of the (f) pyrochlore  $\text{Nd}_2\text{Ir}_2\text{O}_7$  thin film and (g) YSZ substrate from the dashed squares region in (c).

## 5.2.3 Strain induced insulator to semimetal transition

### 5.2.3.1 Strain effect and phase diagram

To elucidate the electronic band structure in the epitaxially strained  $\text{Nd}_2\text{Ir}_2\text{O}_7$  thin film, we perform a mean-field calculation (see Methods). Figure 5.6(a) shows the structure of the pyrochlore lattice. An Ir atom sits at each vertex of a tetrahedron and four sites within a tetrahedral unit cell are numbered from 1 to 4. When this Ir tetrahedron gets strained along [111] direction, its perfect tetrahedron breaks. The 4-1, 4-2, and 4-3 become elongated while 1-2, 2-3, and 3-1 become shorter [see Fig. 5.6(b)]. Our calculation shows this strain induced lattice deformation strongly affects its electronic structure. Starting from AIAO insulator (since this is true for bulk  $\text{Nd}_2\text{Ir}_2\text{O}_7$ ) when the strength of uniaxial strain along [111] direction gets larger it enters to the 1P WSM (it stands for 1 pair Weyl semimetal) as shown in Fig. 5.6(c). For 1P WSM two different Weyl points with opposite chirality, exist along the  $\Gamma$ -L inside the Brillouin zone as shown in Fig. 5.6(d). As each pair of Weyl points is constrained to be on a one-dimensional line, pair-annihilation can be easily achieved by increasing the pair separation until they merge at the Brillouin zone boundary. The 4P WSM to 1P WSM

transition can be easily understood that only 1-pair of Weyl points survive along  $k//[111]$  while other pairs annihilate due to the uniaxial strain along  $[111]$  direction. Our mean-field calculation support that strain can be a new powerful control parameter to study correlated topological phases.

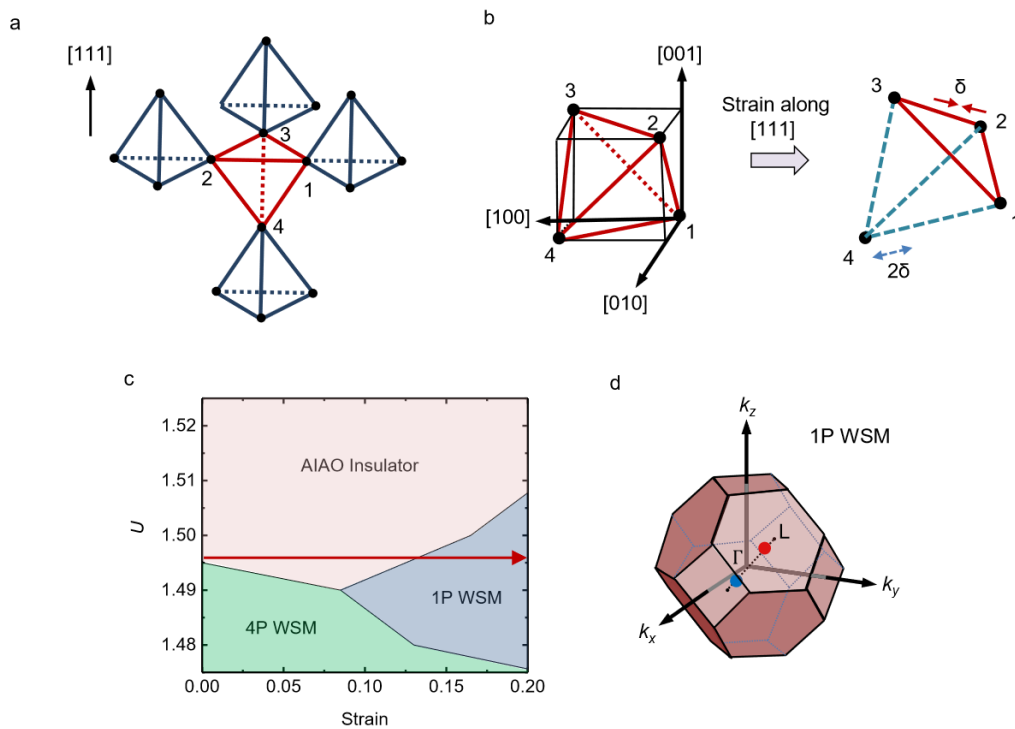


Figure 5.6 Theoretical descriptions on strain induced Weyl semimetallic state. (a), Structure of the pyrochlore lattice. An Ir atom sits at each vertex of a tetrahedron. Four sites within a tetrahedral unit cell are numbered from 1 to 4. (b), The coordinate of Ir sites depicted with specific crystallographic directions. Tetrahedron lattice deformations are also shown when it gets strained along  $[111]$ . (c), The phase diagram where the vertical axis is the electron correlation  $U$  and the horizontal axis is a strain strength along  $[111]$

directions. AIAO and 4P (1P) WSM stand for all-in-all-out and four points (one point) Weyl semimetal. (d), Schematic picture of the distribution of Weyl points in the three-dimensional momentum space for 1P WSM.

### 5.2.3.2 Resistivity comparison between fully relaxed and strained thin films

Now we compare the electronic transport behavior of our strained 9-nm-thick  $\text{Nd}_2\text{Ir}_2\text{O}_7$  thin film to bulk like relaxed 80-nm-thick film from our previous work [30]. The resistivity curve of our 80-nm-thick  $\text{Nd}_2\text{Ir}_2\text{O}_7$  thin film exhibits a metal to insulator transition (MIT) around  $T \sim 30$  K [see black open circles in Fig. 5.7(a)], close to its single crystal bulk value [31,32]. Our *in-situ* 9-nm-thick  $\text{Nd}_2\text{Ir}_2\text{O}_7$  thin film also exhibits metal to insulator transition (MIT)-like resistivity upturn [see blue circles in Fig. 5.7(a)]. However, its resistivity is more than one order of magnitude smaller than 80-nm-thick sample at overall  $T$  range. This large reduction of resistivity value might be the strain effect of the film. Its nonmetallic resistivity  $\rho$  versus  $T$  profile under  $\sim 30$  K, also support that strained samples are close to semimetallic state. Recent effective tight-binding model calculation reported that under the uniaxial strain along the [111] direction of the pyrochlore iridate, it can have the Weyl semimetallic state [33].

Temperature dependent magnetoresistivity shows that magnetic ordering starts to form at  $\sim 15$  K. It is well known that pyrochlore iridates have distinct non-coplanar antiferromagnetic ordering called AIAO [31]. When it is magnetically ordered,  $\rho_{xx}$  shows

negative field dependence; negative magnetoresistivity appears [27]. The temperature dependent magnetoresistivity show positive to negative sign change between 8 and 15 K as shown in Fig. 5.7(b). We observed clear positive to negative sign switching at  $\sim 15$  K from normalized MR versus  $T$  in Fig. S1. It is consistent with the Néel ordering temperature of the Nd moment ( $T_N^{\text{Nd}}$ ) [34]. We could not observe clear MR hysteresis solely from Ir moment where we observed in fully relaxed thick film [30]. The Néel ordering temperature of Ir moment might become lowered due to the quantum fluctuation in very thin film.

The magnetic ground state of  $\text{Nd}_2\text{Ir}_2\text{O}_7$  is well described in previous studies [22,23,30,31].  $\text{Nd}_2\text{Ir}_2\text{O}_7$  is composed of two types of tetrahedra, Ir and Nd sublattices, as shown in Fig. 5.7(c). Without any external field, as shown by the red arrows, all four of the Ir spins at the vertices of a tetrahedron point inward. At the nearest neighboring Ir tetrahedra (not shown), all of the Ir spins should point outward. These results in AIAO ordering of Ir spins, which we refer to as Ir:AIAO. At the same time, the spins in the Nd sublattice have similar magnetic ordering (all-out-all-in), Nd:AOAI, as shown in Fig. 5.7(c). Under an external magnetic field,  $H$ , we can switch between AIAO and AOAI domains of Ir spin. Note that the Nd ion has a larger magnetic moment; thus, the corresponding Zeeman field is larger. When  $H$  increases along the [111] direction, Nd spins become canted and then suddenly flip to form the 3-in-1-out (3I1O) configuration [30]. At a higher  $H$ , Nd spins can induce the flip of Ir sublattice spin into the AOAI configuration via the  $f$ - $d$  exchange interaction.

The low temperature,  $T \sim 2$  K, magnetoresistivity confirmed the magnetic ground

state of strained thin film is AIAO type. Hereafter, we shall take a careful look into the low-field range in which the AIAO order is preferred. Figure 5.7(d) shows the magnified view of the low-field region of magnetoresistivity at 2 K. The  $\rho_{xx}$  on the field decreasing process (denoted by the blue line) is larger than that on the field-increasing process (the red line) in the positive field region, and they turn opposite in the negative field side. This hysteresis can be explained by the unique configuration of Ir: AIAO order and Ir: AOAI, each of which can be aligned by the application of the  $H$ -field along [111] or the opposite direction [27,35]. The aligned AIAO configuration can induce the odd component of  $\rho_{xx}$  as demonstrated in a previous study [35]. Therefore, the butterfly-type hysteresis of  $\rho_{xx}$  within  $\pm 0$  T indicates that the single domain state is realized after applying the magnetic field along [111] direction.

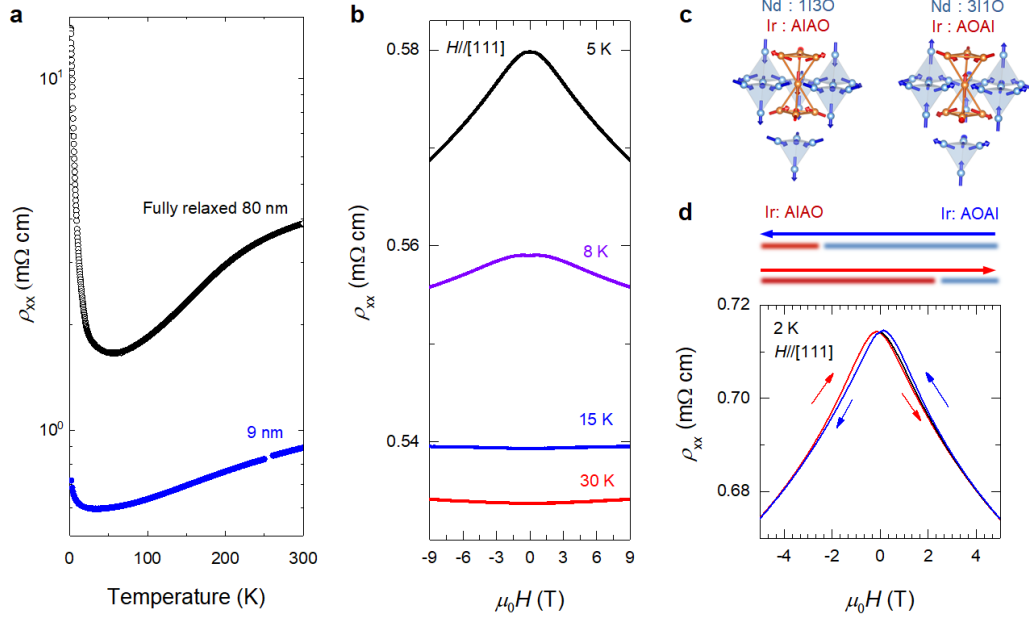


Figure 5.7 Strain-induced emergent topological phases (a) Black open (blue filled) circles indicate the temperature-dependent resistivity of the fully relaxed (strained) 80-nm-thick (9-nm-thick)  $\text{Nd}_2\text{Ir}_2\text{O}_7$  thin film. (b) Magnetoresistivity (MR) values of fully strained 9-nm-thick film at various temperatures with  $H // [111]$ . Negative to positive MR change occurs near the  $T_N \sim 15$  K. (c) The schematic figure of magnetic structure of  $\text{Nd}_2\text{Ir}_2\text{O}_7$  in sufficiently strong  $H$ . The Nd-4f and Ir-5d moments are coupled with the  $f$ - $d$  exchange interaction. (d) MR value with  $H // [111]$  at 2 K of the 9-nm-thick film. It shows MR hysteresis from AIAO/AOAI domain switching.

### 5.2.4 Large anomalous Hall effect and cubic symmetry breaking

Significantly, we also observed the hysteresis in Hall conductivity,  $\sigma_{xy}$ . When the  $H$ -field decreases,  $\sigma_{xy}$  denoted in blue circles decreases towards  $-2 \Omega^{-1} \text{ cm}^{-1}$  at 0 T as shown in Fig. 5.8(a).  $\sigma_{xy}$  on the field-increasing process (red circles) shows the similar field dependency with the opposite sign, shaping an unambiguous rhombus-type hysteresis within  $\pm 2$  T. This hysteresis remains under  $T_N \sim 15$  K. The size of anomalous Hall conductivity,  $\Delta\sigma_{xy}$ , reduces significantly when temperature gets higher. For instance, at  $T \sim 5$  K,  $\Delta\sigma_{xy} \sim 0.1 \Omega^{-1} \text{ cm}^{-1}$  which is more than 10 times smaller than  $\Delta\sigma_{xy}$  at 2 K [see Fig. 5.8(b)]. When  $T$  becomes  $\sim 8$  K, it gets even smaller  $\Delta\sigma_{xy} \sim 0.04 \Omega^{-1} \text{ cm}^{-1}$  [see Fig. 5.8(c)].

Anomalous Hall conductivity at low temperature can be understood as intrinsic effects; AHE originating from the Berry phase mechanism [36]. First, this AHE only appears at low  $H$ -field region where magnetism should govern by antiferromagnetism; Ir: AIAO/AOAI and Nd: AOAI/AIAO ordering. Thus, the AHE should not be caused by the conventional AHE related to ferromagnetism. Second, our magnetotransport results can rule out the extrinsic effect; skew-scattering and the side-jump [37]. Those two extrinsic effects are attributed to a carrier scattering by crystalline disorders or impurities. We can safely rule out the skew-scattering contribution which basically is dominant in the high-conductivity regime ( $\sigma_{xx} \geq 10^6 \Omega^{-1} \text{ cm}^{-1}$ ); in our case  $\sigma_{xx} \sim 10^3 \Omega^{-1} \text{ cm}^{-1}$ . The rest mechanism is the side-jump; however, it is difficult to partition each other only according to the scaling rule between  $\sigma_{xx}$  and  $\sigma_{xy}$ . We therefore pay our attention to the temperature

dependency. As one can see in Fig. 4, the spontaneous part of  $\Delta\sigma_{xy}$  enhances at very low temperature,  $T \sim 2$  K (more than one order difference compare to  $\Delta\sigma_{xy}$  at  $\sim 5$  K) and almost disappears above  $T \sim 8$  K, during which  $\Delta\sigma_{xx}$  ( $\Delta\rho_{xx}$ ) decreases (increases) only about 10%. Since the side-jump mechanism originates from an impurity scattering, it can hardly explain the observed steep temperature dependence. Thus, we conclude that the intrinsic mechanism, which is sensitive to the electronic band structure, is most plausible for  $\sigma_{xy}$  observed in the course of the phase transition.

Moreover, symmetry analysis support that this large AHE can only can appear when cubic symmetry is broken. The symmetry analysis show the anomalous Hall conductivity cannot occur in a single domain of AIAO order in cubic pyrochlore iridates [13,30]. Presence of two-fold rotation symmetry around the three orthogonal axes exists (cubic symmetry), Hall conductivity should be trivial. However, when two-fold rotation symmetries become broken but there exists a three-fold rotational symmetry about the axis perpendicular to the sample plane, AHE can occur in the sample plane. Our strained thin film gives exactly same geometry as explained above. Cubic symmetry of the system is naturally broken in strained thin film by the uniaxial strain along [111] direction. The fully relaxed  $\text{Nd}_2\text{Ir}_2\text{O}_7$  film has negligibly small anomalous Hall conductivity ( $\sim 0.05 \text{ } \Omega^{-1} \text{ cm}^{-1}$ ) compare to our strained thin film (more than  $\sim 40$  times smaller) [see Fig. S2]. The AHE in fully relaxed  $\text{Nd}_2\text{Ir}_2\text{O}_7$  is mainly driven by the uncompensated magnetic moments at the domain wall. Compare to fully relaxed film, our observation of large anomalous Hall conductivity is driven by structural symmetry breaking via strain effect.

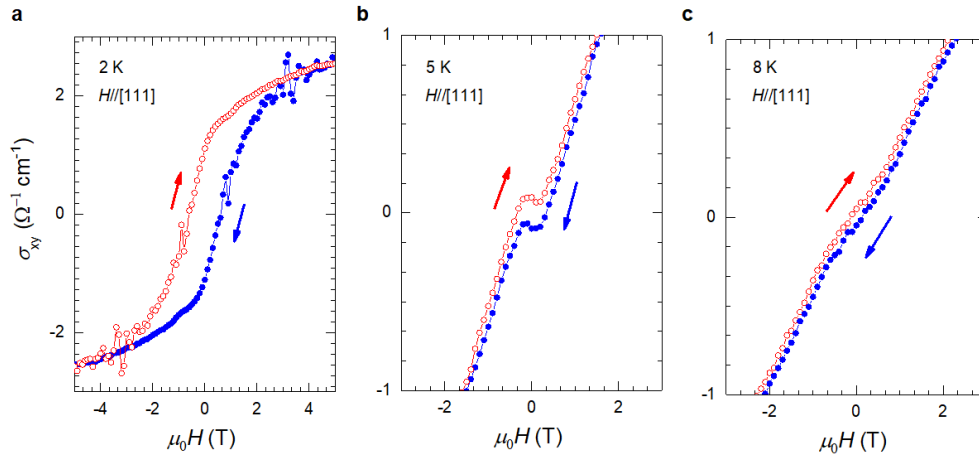


Figure 5.8 Large anomalous Hall conductivity. Hall conductivity for a magnetic field along [111] direction at various temperature (a), 2 K, (b), 5 K, and (c), 8 K. The red (blue) lines are Hall conductivity and magnetization on field-increasing (field-decreasing) process.

## 5.2.5 Chiral anomaly-related magnetoresistance in Weyl semimetals

Since we observed a large AHE, the observation of chiral anomaly will be another strong evidence for the underlying magnetic Weyl fermions. The chiral anomaly describes violation of separate number conservation laws for the left- and right-handed Weyl fermions in the presence of parallel electric and magnetic fields. When the resulting number imbalance between the Weyl fermions of opposite chirality is relaxed by

scattering between two Weyl points [see the Fig. 5.9(a)], one can obtain a positive longitudinal magnetoconductance (LMC) [38–40], while the transverse magnetoconductance remains negative. Such anisotropic magnetoconductance due to chiral anomaly has been experimentally confirmed in weakly correlated materials [41–44].

The magnetoconductance was measured in a schematic configuration shown in the insets of Fig. 5.9(b). The current  $I$  is applied along the  $[0\bar{1}1]$  axis, and angle dependent magnetoconductance were measured, i.e.,  $0^\circ$  for  $H \perp I$  and  $90^\circ$  for  $H//I$ . Although strong anisotropic magnetoconductance were not observed conductivity enhancement from chiral charge pumping was observed. Positive magnetoconductance occur even  $H \perp I$  due to distinct MR feature coming from AIAO ordering. When  $H//I$  ( $H \perp I$ ), the longitudinal conductance increases (decreases) with  $H$  as shown in Fig. 5.9(b). Moreover, the size of the positive magnetoconductivity,  $\sigma_{xx}(H)$ . Moreover, in weak  $H$  with  $H//I$ , LMC has the  $H^2$  dependence. Quadratic dependence of LMC is expected for type-I Weyl semimetals [45]. Thus, the observed  $H^2$  increase of the positive magnetoconductance in the low  $H$ -field regime is consistent with a chiral anomaly of the type-I Weyl fermion state predicted for pyrochlore iridates. To clarify the anisotropic character, we scanned the angle  $\theta$  between the  $H$  and  $I$  directions for the magnetoconductance measurements as shown in Fig. 5.9(d). The positive magnetoconductance becomes maximized when  $H//I$  ( $\theta = 90^\circ$ ). We believe that this locking pattern in weak  $H$  is the quintessential signature of the axial current from Weyl state.

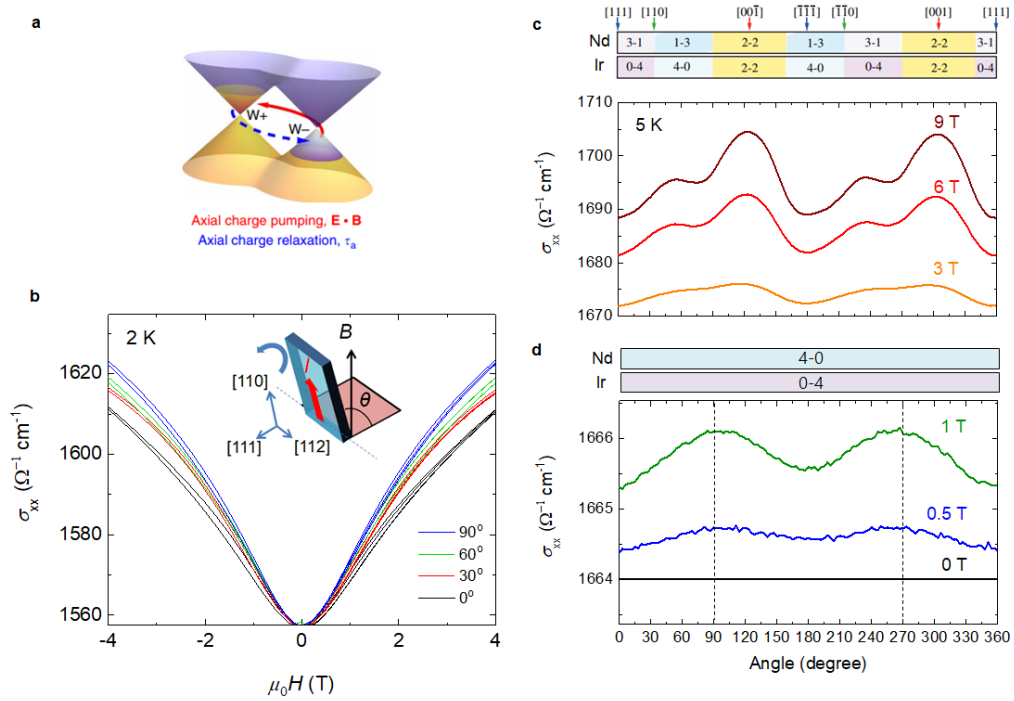


Figure 5.9 Evidence for charge pumping through Weyl points. (a), Sketch of two massless Weyl points at  $W_+$  and  $W_-$  which have distinct chiralities  $C = +1$  and  $-1$  respectively. (b), Magnetoconductivity in  $H$ -field at various angles. In weak  $H$ , it has the  $H^2$  form predicted in Type-I Weyl semimetal [45]. Inset figure shows the measurement geometry. Angle dependent magnetoconductivity at (c) high and (d) low  $H$ -fields.

### 5.3 Conclusion

We have developed the special PLD growth technique called repeated pulse annealing epitaxy to successively synthesize *in-situ*  $\text{Nd}_2\text{Ir}_2\text{O}_7$  thin film. We could obtain high quality  $\text{Nd}_2\text{Ir}_2\text{O}_7$  epitaxial thin film on YSZ (111) substrate. We observed that our compressive strained thin film have lower resistivity compare to the fully relaxed thick film. This significant reduction of resistivity might be due to the strain effect. We also observed from the MR measurement that the magnetic ground state of the strained thin film is AIAO ordering. Surprisingly, we observed large anomalous Hall effect presumably due to the strain induced Weyl semimetallic state. Our LMC results also support the existence of Weyl state in  $\text{Nd}_2\text{Ir}_2\text{O}_7$  thin film. Finally our mean-field calculation confirmed that strain effect can be a good tuning parameter for studying correlated topological phases including Weyl, Axion, and strong topological insulator.

---

**References**

- [1] R. Resta, Phys. Rev. Lett. **105**, 127601 (2010).
- [2] Y. Lee, Z. Q. Liu, J. T. Heron, J. D. Clarkson, J. Hong, C. Ko, M. D. Biegalski, U. Aschauer, S. L. Hsu, M. E. Nowakowski, J. Wu, H. M. Christen, S. Salahuddin, J. B. Bokor, N. A. Spaldin, D. G. Schlom, and R. Ramesh, Nat. Commun. **6**, 5959 (2015).
- [3] J. Engelmann, V. Grinenko, P. Chekhonin, W. Skrotzki, D. V Efremov, S. Oswald, K. Iida, R. Hühne, J. Hänisch, M. Hoffmann, F. Kurth, L. Schultz, and B. Holzapfel, Nat. Commun. **4**, 2877 (2013).
- [4] M. Imada, A. Fujimori, and Y. Tokura, Rev. Mod. Phys. **70**, 1039 (1998).
- [5] X. Wan, A. M. Turner, A. Vishwanath, and S. Y. Savrasov, Phys. Rev. B **83**, 205101 (2011).
- [6] D. Pesin and L. Balents, Nat. Phys. **6**, 376 (2010).
- [7] W. Witczak-Krempa, G. Chen, Y. B. Kim, and L. Balents, Annu. Rev. Condens. Matter Physics, Vol 5 **5**, 57 (2014).
- [8] K. Matsuhira, M. Wakeshima, R. Nakanishi, T. Yamada, A. Nakamura, W. Kawano, S. Takagi, and Y. Hinatsu, J. Phys. Soc. Japan **76**, 43706 (2007).
- [9] J. J. Ishikawa, E. C. T. O'Farrell, and S. Nakatsuji, Phys. Rev. B **85**, 245109 (2012).
- [10] C. H. Sohn, C. H. Kim, L. J. Sandilands, N. T. M. Hien, S. Y. Kim, H. J. Park, K. W. Kim, S. J. Moon, J. Yamaura, Z. Hiroi, and T. W. Noh, Phys. Rev. Lett. **118**, 117201 (2017).

- [11] H. Shinaoka, S. Hoshino, M. Troyer, and P. Werner, *Phys. Rev. Lett.* **115**, 156401 (2015).
- [12] T. M. H. Nguyen, L. J. Sandilands, C. H. Sohn, C. H. Kim, A. L. Wysocki, I.-S. Yang, S. J. Moon, J.-H. Ko, J. Yamaura, Z. Hiroi, and T. W. Noh, *Nat. Commun.* **8**, 251 (2017).
- [13] B.-J. Yang and N. Nagaosa, *Phys. Rev. Lett.* **112**, 246402 (2014).
- [14] K. Hwang and Y. B. Kim, *Sci. Rep.* **6**, 30017 (2016).
- [15] P. Laurell and G. A. Fiete, *Phys. Rev. Lett.* **118**, 177201 (2017).
- [16] E. Y. Ma, Y.-T. Cui, K. Ueda, S. Tang, K. Chen, N. Tamura, P. M. Wu, J. Fujioka, Y. Tokura, and Z.-X. Shen, *Science* (80-. ). **350**, 538 (2015).
- [17] T. C. Fujita, M. Uchida, Y. Kozuka, S. Ogawa, A. Tsukazaki, T. Arima, and M. Kawasaki, *Appl. Phys. Lett.* **108**, 22402 (2016).
- [18] T. C. Fujita, Y. Kozuka, J. Matsuno, M. Uchida, A. Tsukazaki, T. Arima, and M. Kawasaki, *Phys. Rev. Mater.* **2**, 11402 (2018).
- [19] G. Chen, *Phys. Rev. B* **94**, 205107 (2016).
- [20] Y. Yamaji and M. Imada, *Phys. Rev. X* **4**, 21035 (2014).
- [21] T. Kondo, M. Nakayama, R. Chen, J. J. Ishikawa, E.-G. Moon, T. Yamamoto, Y. Ota, W. Malaeb, H. Kanai, Y. Nakashima, Y. Ishida, R. Yoshida, H. Yamamoto, M. Matsunami, S. Kimura, N. Inami, K. Ono, H. Kumigashira, S. Nakatsuji, L. Balents, and S. Shin, *Nat. Commun.* **6**, 10042 (2015).
- [22] K. Ueda, T. Oh, B.-J. Yang, R. Kaneko, J. Fujioka, N. Nagaosa, and Y.

- Tokura, *Nat. Commun.* **8**, 15515 (2017).
- [23] K. Ueda, R. Kaneko, H. Ishizuka, J. Fujioka, N. Nagaosa, and Y. Tokura, *Nat. Commun.* **9**, 3032 (2018).
- [24] K. T. Jacob, T. H. Okabe, T. Uda, and Y. Waseda, *Electrochim. Acta* **45**, 1963 (2000).
- [25] W. C. Yang, Y. T. Xie, W. K. Zhu, K. Park, A. P. Chen, Y. Losovyj, Z. Li, H. M. Liu, M. Starr, J. A. Acosta, C. G. Tao, N. Li, Q. X. Jia, J. J. Heremans, and S. X. Zhang, *Sci. Rep.* **7**, 7740 (2017).
- [26] J. C. Gallagher, B. D. Esser, R. Morrow, S. R. Dunsiger, R. E. A. Williams, P. M. Woodward, D. W. McComb, and F. Y. Yang, *Sci. Rep.* **6**, 22282 (2016).
- [27] T. C. Fujita, Y. Kozuka, M. Uchida, A. Tsukazaki, T. Arima, and M. Kawasaki, *Sci. Rep.* **5**, 9711 (2015).
- [28] W. E. Bell, M. Tagami, and R. E. Inyard, *J. Phys. Chem.* **70**, 2048 (1966).
- [29] T. W. Kim, Woo Jin; Ko, Eun Kyo; Kim, So Yeun; Kim, Bonju; Noh, *Curr. Appl. Phys.* (n.d.).
- [30] W. J. Kim, J. H. Gruenewald, T. Oh, S. Cheon, B. Kim, O. B. Korneta, H. Cho, D. Lee, Y. Kim, M. Kim, J.-G. Park, B.-J. Yang, A. Seo, and T. W. Noh, *Phys. Rev. B* **98**, 125103 (2018).
- [31] K. Ueda, J. Fujioka, B.-J. Yang, J. Shiogai, A. Tsukazaki, S. Nakamura, S. Awaji, N. Nagaosa, and Y. Tokura, *Phys. Rev. Lett.* **115**, 56402 (2015).
- [32] Z. Tian, Y. Kohama, T. Tomita, H. Ishizuka, T. H. Hsieh, J. J. Ishikawa, K.

- Kindo, L. Balents, and S. Nakatsuji, *Nat. Phys.* **12**, 134 (2015).
- [33] D. Varnava, Nicodemos ; Vanderbilt, *ArXiv* **1809**, (2018).
- [34] K. Tomiyasu, K. Matsuhira, K. Iwasa, M. Watahiki, S. Takagi, M. Wakeshima, Y. Hinatsu, M. Yokoyama, K. Ohoyama, and K. Yamada, *J. Phys. Soc. Japan* **81**, 34709 (2012).
- [35] T. Arima, *J. Phys. Soc. Japan* **82**, 13705 (2012).
- [36] S. Onoda, N. Sugimoto, and N. Nagaosa, *Phys. Rev. B* **77**, 165103 (2008).
- [37] N. Nagaosa, J. Sinova, S. Onoda, A. H. MacDonald, and N. P. Ong, *Rev. Mod. Phys.* **82**, 1539 (2010).
- [38] H. B. Nielsen and M. Ninomiya, *Phys. Lett. B* **130**, 389 (1983).
- [39] D. T. Son and B. Z. Spivak, *Phys. Rev. B* **88**, 104412 (2013).
- [40] P. Goswami, J. H. Pixley, and S. Das Sarma, *Phys. Rev. B* **92**, 75205 (2015).
- [41] J. Xiong, S. K. Kushwaha, T. Liang, J. W. Krizan, M. Hirschberger, W. Wang, R. J. Cava, and N. P. Ong, *Science* (80-. ). **350**, 413 LP (2015).
- [42] M. Hirschberger, S. Kushwaha, Z. Wang, Q. Gibson, S. Liang, C. A. Belvin, B. A. Bernevig, R. J. Cava, and N. P. Ong, *Nat. Mater.* **15**, 1161 (2016).
- [43] C.-L. Zhang, S.-Y. Xu, I. Belopolski, Z. Yuan, Z. Lin, B. Tong, G. Bian, N. Alidoust, C.-C. Lee, S.-M. Huang, T.-R. Chang, G. Chang, C.-H. Hsu, H.-T. Jeng, M. Neupane, D. S. Sanchez, H. Zheng, J. Wang, H. Lin, C. Zhang, H.-Z. Lu, S.-Q. Shen, T. Neupert, M. Zahid Hasan, and S. Jia, *Nat.*

Commun. **7**, 10735 (2016).

[44] X. Huang, L. Zhao, Y. Long, P. Wang, D. Chen, Z. Yang, H. Liang, M. Xue, H. Weng, Z. Fang, X. Dai, and G. Chen, Phys. Rev. X **5**, 31023 (2015).

[45] V. A. Zyuzin, Phys. Rev. B **95**, 245128 (2017).

## Chapter 6

### Conclusion

The strain effect has been a key control parameter for emergent phenomena in heterostructure. Particularly in transition metal oxides (TMOs), spin, charge, and lattice degree of freedoms are strongly coupled; strain effect can strongly affect their ground state. However for realizing nontrivial topological phases in TMOs, not many studies are done. Since, nontrivial band topology in TMOs are driven by both relativistic spin-orbit coupling (SOC) and onsite correlation ( $U$ ) the actual materials is confined to very narrow choice;  $5d$  compounds mostly. Those  $5d$  compounds are extremely difficult to grow into high quality thin films. We developed new pulsed laser deposition (PLD) growth technique to overcome such difficulties. We also extend the field for studying correlated topological state by means of strain effect.

First, we investigated the electronic structure of  $\text{IrO}_2$  to address the controversy regarding SOC effects in metallic  $5d$  TMOs. Two issues have come to the forefront: (1) SOC effects on electronic structure and physical properties of  $\text{IrO}_2$  and (2) the possible formation of a novel ground state in this material, the  $J_{eff} = 1/2$  state. To better understand the SOC mechanism, we grew epitaxial  $\text{IrO}_2$  films whose dc resistivity values were comparable with those of a single crystal. We obtained polarization-dependent optical

and x-ray absorption spectra (XAS) and compared these results with those acquired using the generalized gradient approximation (GGA) and GGA+SOC calculations. From the optical spectra, peak structures were identified at 0.4 and 2.0 eV, which could only be explained using the GGA+SOC calculation. This suggests that SOC plays an important role in the electronic structure of IrO<sub>2</sub>. From the polarization-dependent O 1s XAS spectra, we observed that the empty state near the Fermi level lacks involvement of an Ir  $d_{xy}$  orbital. Despite the importance of SOC in IrO<sub>2</sub>, the  $J_{eff} = 1/2$  state does not form in metallic IrO<sub>2</sub>.

Second, we observed a large anomalous Hall effect (AHE) in an antiferromagnetic (AFM) Nd<sub>2</sub>Ir<sub>2</sub>O<sub>7</sub> thin film, which was induced mainly by the domain walls (DWs). The strong  $f-d$  exchange interaction effectively lowers the energy barrier for Ir domain switching, such that a small magnetic field can be used to control the Ir-DW. Eventually, effective Ir-domain switching induces an intrinsic AHE from the Berry curvature at the DW, leading to a large DW-AHE,  $\sim 15 \mu\Omega \text{ cm}$  at 2 K. Given the observation of AHE at DWs, we suggest that Nd<sub>2</sub>Ir<sub>2</sub>O<sub>7</sub> is a fertile area for the discovery and investigation of new topological phenomena. As the DW-conducting channels of Nd<sub>2</sub>Ir<sub>2</sub>O<sub>7</sub> are attributable to the fact that the system lies close to the topological Weyl semimetal phase, the observed DW-driven AHE provides additional evidence that the system exhibits novel topological properties.

For the last part, we have developed the special PLD growth technique called repeated pulse annealing epitaxy to successively synthesize *in-situ* Nd<sub>2</sub>Ir<sub>2</sub>O<sub>7</sub> thin film. We could obtain high quality Nd<sub>2</sub>Ir<sub>2</sub>O<sub>7</sub> epitaxial thin film on YSZ (111) substrate. We

observed that our compressive strained thin film have lower resistivity compare to the fully relaxed thick film. This significant reduction of resistivity might be due to the strain effect. We also observed from the MR measurement that the magnetic ground state of the strained thin film is AIAO ordering. Surprisingly, we observed large anomalous Hall effect presumably due to the strain induced Weyl semimetallic state. Our LMC results also support the existence of Weyl state in  $\text{Nd}_2\text{Ir}_2\text{O}_7$  thin film. Finally our mean-field calculation confirmed that strain effect can be a good tuning parameter for studying correlated topological phases including Weyl, Axion, and strong topological insulator.

## **Publication list**

- [1] **Woo Jin Kim**, So Yeun Kim, Choong. H. Kim, Chang Hee Sohn, Oleksandr B. Korneta, Seung Chul Chae, and Tae Won Noh, *Spin-orbit coupling induced band structure change and orbital character of epitaxial IrO<sub>2</sub> films*, Phys. Rev. B **93**, 045104 (2016).
- [2] **Woo Jin Kim**, John H. Gruenewald, Taekoo Oh, Sangmo Cheon, Bongju Kim, Oleksandr B. Korneta, Hwanbeom Cho, Daesu Lee, Yoonkoo Kim, Miyoung Kim, Je-Geun Park, BohmJung Yang, Ambrose Seo and Tae Won Noh, *Unconventional anomalous Hall effect from antiferromagnetic domain walls of Nd<sub>2</sub>Ir<sub>2</sub>O<sub>7</sub> thin films*, Phys. Rev. B **98**.125103 (2018).
- [3] **Woo Jin Kim**, Eun-Kyo Ko, So Yeun Kim, Bongju Kim, and Tae Won Noh, *In-operando spectroscopic ellipsometry studies of IrO<sub>2</sub> dynamic instabilities: Guide to in-situ growth of pyrochlore iridate thin films*, accepted in Current Applied Physics (2019).
- [4] **Woo Jin Kim**, Taekoo Oh, Eun-Kyo Ko, Jeongkeun Song, Junsik Mun, Bongju Kim, Miyoung Kim, Bohm-Jung Yang, Daesu Lee and Tae Won Noh, *Strain induced Weyl semimetal state in epitaxial Nd<sub>2</sub>Ir<sub>2</sub>O<sub>7</sub> thin films*, in preparation (2019).
- [5] John H. Gruenewald, **Woo Jin Kim**, Bongju Kim, Tae Won Noh, and Ambrose Seo, *The Weyl semimetallic phase in mixed phase pyrochlore iridates thin films*, in preparation (2019).
- [6] So Yeun Kim, Hyojin Yoon, **Woo Jin Kim**, Chang Hee Sohn, Soon Jae Moon, Seyoung Park, Junwoo Son, Byung Cheol Park, and Tae Won Noh, *Optical Determination of H content and Phase Boundaries in H<sub>x</sub>VO<sub>2</sub> Thin Films*, in preparation (2019).
- [7] Jinkwon Kim, Bongju Kim, Junsik Mun, Han Gyeol Lee, Daesu Lee, **Woo Jin Kim**, Tae Heon Kim, Shinbuhm Lee, Miyoung Kim, Seo Hyoung Chang, and Tae Won Noh,

***Publication list***

---

*Interface layer of BaPb<sub>1-x</sub>Bi<sub>x</sub>O<sub>3</sub> thin film on SrTiO<sub>3</sub> induced by large lattice mismatch, in preparation (2019).*

## 국문 초록

5d 전이금속 산화물은 매우 다양하고 흥미로운 양자현상이 발견될 것으로 보이는 물질로써 사람들이 많은 관심을 불러 일으켰다. 특히나, 5d 전이금속 산화물에서는 전자-전자 상호작용( $U$ ), 전자 띠 폭( $W$ ) 그리고 스핀-궤도 상호작용(SOC)이 비슷한 에너지량을 갖고 있는 것으로 알려져 있다. 이 세 에너지들의 상호작용은 새로운 위상 현상들을 발현시킬 수 있다. 5d 전이금속 산화물 중, 이리듐으로 구성되어 있는 산화물들은 특히나 이리듐의 큰 SOC에 의한 특별한 물리현상으로 많은 사람들의 관심을 끌어왔다. 다양한 이리듐 산화물 혹은 이중구조들은 바일 준금속, 액시온 절연체 그리고 위상 절연체 등의 전자 구조들을 가지고 있을 것이라고 예측되어 왔다.

에피택셜한 얇은 박막은 이러한 위상 현상들을 연구하기 위한 좋은 시스템을 제공한다. 타겟 물질을 에피택셜한 박막으로 성장시키는 것은 위상물질들을 연구하기에 다음과 같은 이유에 의해 좋다. 첫째, 다양한 기관을 통해 우리는 서로 다른 결정 시메트리를 가진 구조들을 만들어 낼 수 있다는 것에 있다. 두번째, 박막으로 제작할 때 가해지는 스트레인 효과를 이용하여 정육면체 시메트리와 같은 특정 시메트리를 무너뜨릴 수 있다는 것에 있다. 이 논문에서 에피택셜하게 기른 이리듐 산화물 박막에서의 전자구조와 그에 의한 위상 물리 현상들에 대해 보고하도록 하겠다.

우리는 먼저 루타일 구조를 가지고 있고, nonsymmorphic 시메트리를 가지고 있는  $\text{IrO}_2$  박막의 전자 구조에 대해 탐구하였다. 우리의 광학 전도도

측정과 generalized gradient approximation (GGA) + SOC 계산을 통해 SOC이  $\text{IrO}_2$ 의  $E_F$  근처의 전자구조에 큰 영향을 끼친다는 것을 알게 되었다. 하지만 O 1s 엑스선 흡수 분광학(XAS) 실험 결과와 projected density of state (pDOS) 분석은 금속성을 띄고 있는  $\text{IrO}_2$ 에서는 더 이상  $J_{\text{eff}} = 1/2$  상태가 존재하지 않는다는 것을 보여주었다. 큰 SOC를 가지면서 금속성을 유지하고 있는  $\text{IrO}_2$ 는 스핀 검출에 매우 민감한 소자와 같은 응용분야에서 좋은 환경을 제공해 준다고 볼 수 있다.

강자성 도메인 벽은 벌크 시료의 싱글 도메인의 시메트리와는 다른 시메터를 제공한다는 면에서 매우 흥미롭다. 특히나, noncoplanar 스핀 구조를 가지고 있는 반강자성성 도메인 벽은 강자성의 그것에서는 일어날 수 없는 특별한 시메트리를 유지할 수 있다. 우리는 일반적이지 않은 anomalous Hall effect (AHE)가 noncoplanar 반강자성을 가지고 있는  $\text{Nd}_2\text{Ir}_2\text{O}_7$ 의 자성 벽에서 나타날 수 있다는 것을 규명하였다. 덩치 시료는 정육면체 시메트리를 유지하고 있어서 외부 자기장이 없을 때 홀 또한 없이 측정 되어야 한다. 여기에 자성벽이 생길 때에, twofold 시메트리가 깨지게 되며 anomalous Hall conductivity가 나올 수 있다. 이러한 연구 결과는 AFM 물질의 도메인에서 깨지는 시메트리가 위상 현상과 그와 관계있는 응용분야를 연구하기에 좋은 환경을 제공한다는 것을 보여준다.

마지막으로 이러한  $\text{Nd}_2\text{Ir}_2\text{O}_7$  물질을 Y-stabilized  $\text{ZrO}_2$  (YSZ) 위에 에피택셜한 스트레인을 인가하여 증착 시킬 때에, 바일 준금속이 될 수 있다는 연구를 하였다. 우리는 매우 큰 AHE를 압축적으로 스트레인을 가한  $\text{Nd}_2\text{Ir}_2\text{O}_7$  얇은 박막에서 관측하였다. 이렇게 큰 AHE의 정량값은 이론적으로

예측한 값과 유사하였다. 더 나아가, 박막의 저항은 스트레인을 받지 않은 박막에 비해 매우 작아 진다는 것을 알 수 있었다. longitudinal magneto-resistance 측정을 통해 음의 magneto-resistance를 관측하였고, 이는 두 바일 점들 사이에서 일어나는 카이랄 전하 수송에 의한 것일 수 있다. 우리는 이러한 실험 결과를 통해, 파이로클로로 이리듐 산화물에서 strain 효과는 위상 발현현상을 연구하기에 매우 좋은 control parameter라는 것을 소개한다.

주요어: 강상관계 위상 상태, 전자 구조, 특이한 홀 효과, 바일 준금속, 파이로클로로 이리듐 산화물, 자성수송..

학번: 2013-20360

## 감사의 글

6년이라는 짧지 않은 연구실 생활 동안 혼자라면 할 수 없었던 일을 할 수 있게 함께 해주신 모든 분들께 진심으로 감사 드립니다. 제일 먼저 저희 가족에게 감사의 인사를 하고 싶습니다. 삼 남매 중 제일 철없는 장남을 믿고 제가 하고 싶은 것을 할 수 있게 격려와 지지를 아끼지 않고 주신 부모님께 감사 드립니다. 30년동안 따뜻한 사랑으로 길러주셔서 여기까지 올 수 있었습니다. 늘 따뜻한 온기가 가득한 집 분위기를 만들어 준 어머니 감사하고 사랑합니다. 매일 늦게 집에 돌아오는 자식 걱정을 해주시고, 집을 나서고 들어오는 현관에서 따뜻한 인사로 배웅 및 마중을 해주셔서 외로운 날이 없었습니다. 제가 세상에서 제일 존경하는 우리 아버지. 자상한 남편이자, 멋진 아버지이며, 훌륭한 학자의 모습을 다 갖추신 아버지 사랑합니다. 식탁에서의 조언과 일상에서 나눈 아버지와의 대화가 살아가는데 매우 큰 자산과 밑거름이 되었습니다. 좋은 형의 모습보다는 챙겨줘야 할 룸메이트의 모습을 보여준 것 같아 미안한 동생 민석이에게도 고마운 마음 전합니다. 악몽에 소리지르며 깨는 형을 다독여 주고 추운 새벽에 이불을 덮어주는 따뜻한 동생의 사랑 덕에 늘 따뜻한 밤을 보낼 수 있었습니다. 우리 집 분위기 메이커 막내 동생 성은이에게도 고마운 마음 전합니다. 집에 잘 있지 않는 무뚝뚝한 오빠들 대신 재롱과 다정다감의 언어로 빈 집을 채워줘서 고맙습니다. 사랑스러운 동생들이 하고자 하는 뭐든 일들이 잘 되기를 소망합니다. 보내주신 사랑과 성원에 실망 시켜드리지 않고, 자랑스러운

아들이자 멋진 형, 오빠가 될 수 있게 항상 노력하겠습니다. 잘 찾아 뵈지 못하는 손자를 언제나 반갑게 맞이해 주시고, 덕담과 재미있는 옛날이야기를 해주시는 친할아버지 할머니께도 감사 드립니다. 또 날카로운 직관력으로 세상을 보는 방법을 알려주시고, 따듯한 사랑으로 응원해주신 외할머니께도 감사 드립니다. 모두 오래오래 건강하세요.

20대 이후 세계 가장 큰 영향을 주신 노태원 교수님께 감사의 인사를 드리고 싶습니다. 걸음마도 떼지 못한 부족한 저를 연구자의 길을 걸을 수 있게 해주신 교수님께 감사 드립니다. 포기하고 싶을 정도로 높은 벽을 만날 때마다, 그 벽을 몸소 올라가는 방법을 보여주시고 가르쳐 주시는 모습을 보고 제가 연구자의 길을 포기하지 않을 수 있었습니다. 학문적인 가르침뿐만 아니라 세상을 살아가는 지혜에 대해서도 가르쳐 주셔서 너무나 감사 드립니다. 학위기간 동안 받은 교수님의 가르침을 잊지 않고 훌륭한 연구자이며 훌륭한 리더로 성장하도록 하겠습니다.

학위기간 동안 연구에 도움을 주신 많은 분들께 감사 드립니다. 먼저 과학을 대하는 순수한 학자의 모습이 무엇인지를 보여주신 서성석 교수님께 감사 드립니다. 또 저희 팀 미팅 때마다 좋은 조언 아끼지 않고 주신 이대수, 장서형, 이신범, 그리고 김태현 교수님께 감사 드립니다. TEM 미팅 때마다, 오셔서 좋은 결과를 만들어 주신 김윤구, 문준식 학생 그리고 김미영 교수님께 감사 드립니다. 또 이론적인 부분에 큰 도움과 가르침을 주신 김충현 박사님, 천상모 교수님, 그리고 양범정 교수님께 감사 드립니다.

흥미로운 이론계산 결과가 나올 때마다 수시로 연락을 주고 받았던 오테구 학생에게도 감사 합니다. 그 외에도 자성 수송실험에 도움을 주신 조환범 학생과 박제근 교수님께도 감사의 인사를 드립니다.

학위기간 동안 가장 많은 시간을 함께 보낸 연구실 선후배님들께 감사 드립니다. 즐거울 때 그리고 힘들 때를 항상 함께 지냈기에 강한 동지애가 느껴지는 여러분들입니다. 먼저 첫 논문을 쓸 때 그림을 그리는 것부터 문단 구성을 하는 방법까지 주말을 아끼지 않고, 친절하게 가르쳐 주신 채승철 교수님께 감사 드립니다. 강렬한 카리스마를 가진 양상모 교수님, 따뜻한 마음으로 후배에게 조언을 아끼지 않았던 병철이형, 지각할 때마다 늦지 말라고 혼냈지만 속은 다정다감한 다운이형, 격의 없이 친근하고 항상 만나면 좋은 향근이형, 영원한 탁구 라이벌 창희형, ‘커피한잔 할까?’ 산책친구 수빈, 술 마시면 욱하고 괴롭히고 싶은 영재 (하지만 사실 널 좋아해), 아름다운 네일아트를 하고 다녀서 내 눈길을 빼앗는 현주 (어디서 받았니?), 날카로운 논리로 무장했지만, 술 앞에서 미소가 예쁜 오지섭, 학부 후배이며, 하나뿐인 연구실 동기이며, 인생 선배로써 많은 것을 내게 가르쳐준 사랑스러운 민철이, ‘인생은 한 방!’ 하지만 그 한 방을 위해 노력을 아끼지 않는 성민이, 연구실 초년 차 때 항상 밤늦게 함께 동거동락(?) 했던 멋진 기덕이, 길 고양이도 예뻐하는 따뜻한 마음의 소유자 호동이, 철저함과 원칙을 중요시하는 그래서 가장 신뢰가 가는 인호, 은은한 차 (tea)의 매력과 달콤한 디저트의 세계로 입문하게 만들어준 소연이, 종종 사라지지만 연구의 대한 열정 가득한 한결이, 냉철한 과학자 정래, 생년월일이 같은 나의 분신 같은 재석이 (외모도 나와

비슷해서 잘생김), 노는 것에 있어서 탑 클래스! 열정 최고 예의 바른 진권이, ‘집에 가고 싶다~’ 함께 집에 가고 싶은 범주, 스펀지처럼 지식을 습득하고, 연구할 때는 파워돌진! 하지만 춤은 아직 내게 배울 것이 많은 은교, 치킨을 좋아하고 미소가 아름다운 앞으로의 활약이 기대되는 지환이와 요즘 나와 가장 많은 시간을 이야기를 나누는, 큰 체구 만큼이나 듬직하게 연구를 잘 할 정근이에게 고맙다고 말하고 싶고 앞으로도 서로 좋은 인연 이어나갈 수 있기를 바랍니다.

6년 동안, 제가 몸담았던 iridate thin film을 거쳐간 박사님들에게도 감사 드립니다. 실험에 대해 잘 몰랐던 연구 초년생 때, 가까이에서 많은 가르침을 줬던 우크라이나 형 Sasha 박사님, 1년동안 연구실에서 함께 연구하며 미팅이 있었던 날이면 맥주한잔을 꼭 함께 하며 스트레스를 풀었던 미국 아재 John에게 감사 인사를 전합니다. 특히 연구자가 갖춰야 할 자세와 좋은 연구 영감을 항상 주신 김봉주 박사님. 연구 외에도 중요한 것이 무엇인지 삶의 지혜를 아낌없이 주신 박사님께 감사 드립니다.

없어서는 안 될 행정적인 지원을 해주신 전지현 실장님, 김정란 선생님, 나고운 선생님, 주양희 선생님, 그리고 지정은 선생님께 감사 드립니다. 특히 가까이서 때론 친구같이 때론 좋은 조연자로 함께해준 1 세부 PA 선생님들께 감사 드립니다. 사후 보고 전문가인 제계 화 한번 안내고 도움 주신 서경누나, 삶의 지혜를 주고, 소맥 제조의 재능을 발견하게 해주신 존경하는 박주영 선생님, 그리고 이제 막 친해져서 더 친해지고 싶은 한나

선생님께 학위 과정 동안 많은 신세를 졌습니다. 심심할 때마다 놀러가서 시답잖은 농담에도 대꾸해주신, 2 세부 Erika 선생님께도 감사합니다. 언제나 연구단을 위해 힘써 주시고, 만날 때마다 얼른 졸업하라고 조언 아끼지 않아 주셨던 김정구 교수님께 감사 드립니다. 앞으로도 건강하시고, 언제나 그래 주셨듯이 후배 과학자들에게 조언 많이 해주시길 부탁 하겠습니다.

논문을 쓸 수 있는 좋은 데이터를 얻을 수 있게 도와주신 기술지원팀원들께도 감사 드립니다. 뻔질거리며 서류작업을 피하는 제게 그래도 웃으며 도와주신 인자하신 지원실장 박원구 박사님, 엘립소 실험을 도와주신 능력자 강태동 박사님, 연구실 주요 시설이 잘 작동할 수 있게 만들어 주신 맥가이버 이인호 선생님, 고품질의 substrate를 제공해주신 금채누나, 클린룸을 정말 클린하게 관리해주신 김태승 & 배현이 선생님, 요청하신 서류를 늦게 보내드려서 늘 죄송한 송인경 박사님, 일 할 땐 누구보다 철저하게 하고, 놀 땐 제대로 놀 줄 아시는 ‘인싸피플’ 이나현 선생님께 감사 드립니다.

학위 기간 동안 연구단 안팎에서 인연이 닿은 분들께도 감사의 인사를 드립니다. 재윤이형, 승진이형, 박수현 박사님, 김형도 박사님, Daniel, Cheng-Tai, Michael, 김민우 박사님, 이승란 박사님, 조명래 박사님, Luke, 박병철 박사님, Saikat, Lingfei, Wei 감사합니다. 마시는 술만큼이나 물리에 대한 열정도 많은 멋진 충원이, 그리고 검은색을 좋아하는 멋쟁이 영선이형에게도 감사의 인사 전합니다.

마지막으로 제 인생의 동반자로 평생 함께 할 한정은양과 그녀의 가족분들께 감사의 인사를 전하면서 글을 마치고자 합니다. 학위 기간 중 가장 바쁘고 가장 힘들 때에 만나서, 모든 기쁜 순간과 힘든 순간을 가까이에서 봐주었기에 학위를 함께 받았다는 마음마저 듭니다. 힘들 때에 어린 아이처럼 투덜거릴 때도, 격려와 토닥거림으로 앞으로 나아갈 힘을 주었고, 기쁠 때 자신의 일처럼 좋아하고 축하해준 당신에게 감사합니다. 앞으로 함께 할 때 순간에도 지금처럼 서로 의지하며 행복하게 나아가길 소망합니다. 사랑합니다. 소중한 따님을 제 인생의 동반자로 허락해주신 정은이 부모님께도 진심으로 감사 드립니다.

이 밖에 여기에 적지 못한 많은 분들에게도 도움을 받았고, 그 도움 덕분에 연구자로서 성장 할 수 있었습니다. 그 모든 분들께 실망시켜드리지 않는 사회의 멋진 리더로 성장하도록 하겠습니다. 감사합니다.

2019년 1월 관악 18동 연구실에서,

김우진